FINITE ELEMENT STUDIES OF REINFORCED AND UNREINFORCED TWO-LAYER SOIL SYSTEMS

by

Christopher Joseph Brocklehurst

A thesis submitted for the Degree of
Doctor of Philosophy
at
the University of Oxford

Wolfson College

Hilary Term 1993

ABSTRACT

FINITE ELEMENT STUDIES OF REINFORCED AND UNREINFORCED TWO-LAYER SOIL SYSTEMS

C. J. Brocklehurst
Wolfson College, University of Oxford

A thesis submitted for the Degree of Doctor of Philosophy

Hilary Term 1993

The purpose of this study is to obtain an insight into the mechanisms by which a geosynthetic membrane influences the performance of a plane strain and an axisymmetric two-layer soil system, where the reinforcement is incorporated either into a layer of fill, or at the interface of a layer of fill overlying clay subgrade.

New axisymmetric membrane and interface element formulations are developed and incorporated in to an existing large strain finite element code. A linear elastic model of behaviour is used for the membrane material and an elastic-perfectly frictional model, based on the Mohr-Coulomb yield function, is implemented for the interface. These new formulations both take account of large global displacement and rotation effects, although the interface element is constrained to small relative displacements, and are checked against small and large strain closed form test problems. The finite element equations are based on an Updated Lagrangian description of deformation.

Plane strain finite element investigations into the significance of the resolution and relative size of the finite element mesh, and the differences between large and small strain analyses, are undertaken. For typical unreinforced and reinforced plane strain and axisymmetric two-layer soil systems a detailed analysis is presented of the soil displacements, strains, stresses, principal stress directions, mobilised fill friction angles and the stresses on the underside of the footing. A series of plane strain and some axisymmetric parametric studies of the various material properties is conducted, to assess the influences and relative importance of those variables to the performance of the two-layer soil system under monotonic loading. The study considers various reinforcement lengths and stiffnesses, fill depths and strengths, and different clay strengths.

The mechanisms of reinforcement are identified through careful examination of the footing load-displacement response, the reinforcement tension and the stresses and displacements at the interfaces with the surrounding soil. A comparative study is also undertaken between the results obtained by the finite element model and those predicted by a plane strain and axisymmetric limit equilibrium design method.

The effects of including a low friction membrane within an oil storage tank base, as secondary containment against oil leakage, are investigated by a series of axisymmetric finite element analyses.

ACKNOWLEDGEMENTS

The research described in this thesis was conducted at Oxford during the period January 1989 to March 1993. The financial support of the Science and Engineering Research Council is gratefully acknowledged.

First of all I wish to express my sincere appreciation to my supervisor, Dr. Harvey Burd, for his accessibility, guidance and endless encouragement with all aspects of this work and for allowing me to use his original finite element code.

I am indebted also to Professor Guy Houlsby for his assistance and inspiring insight into real geotechnical problems and to Dr. Richard Jewell for his help and contagious enthusiasm in the early stages of the research. The privilege of studying under Professor C. P. Wroth, while he was head of the department at Oxford, will also remain a memorable part of my education.

My thanks go also to every member of the Soil Mechanics Research Group, especially Ross Bell, Anjum Chaudhry, Chris Eggleton, Chris Martin, Ivo Martorano, Paul Norris, Nigel Nutt, Adrian Pearson, Martin Pedley, Fernando Schnaid, Michael Smith, James Swee and Hai-Sui Yu, and to all my friends and colleagues in Oxford, for creating a stimulating academic environment and for always willing to provide essential social diversions.

Only for you, children of doctrine and learning, have we written this work. Examine this book, ponder the meaning we have dispersed in various places and gathered again; what we have concealed in one place we have disclosed in another, that it may be understood by your wisdom.

Heinrich Cornelius Agrippa von Nettesheim, *De occulta philosophia,* 3, 65

To my parents

CONTENTS

NOMENCLATURE

Additional symbols and occasional alternative usage of the symbols below are defined where they occur in the text.

A	Cross-sectional area of membrane element
a_i	Generalised reference co-ordinate
$[B]$	Matrix relating strain rate and nodal velocities
B	Footing half width in plane strain conditions
B'	Effective footing half width
$[C]$	Distortion rate matrix
$[D]$	Material stiffness matrix
$[D]^E$	Elastic material stiffness matrix
$[D]^P$	Plastic material stiffness matrix
$[D]^{EP}$	Elasto-plastic material stiffness matrix
D_c	Clay depth
D_f	Fill depth
E , E_u	Young's modulus
F_r	Longitudinal reinforcement tension
F_{tang}	Tangential reinforcement tension
F_{circ}	Circumferential reinforcement tension
F_u	Ultimate bearing load
F_{ix} , F_{iy}	Nodal forces
f_i	Nodal shape function
$f(\sigma)$	Yield function
G	Shear modulus
G_c	Clay shear modulus
G_f	Fill shear modulus
$g(\sigma)$	Plastic potential
H_P	Depth of plastic failure zone in clay
$[J]$	Jacobian matrix
J	Reinforcement stiffness
$[K]$	Stiffness matrix
K	Reinforcement bulk modulus

K_s	Coefficient of punching shearing resistance
K_0	Coefficient earth pressure
k	Vector constant
$\tilde{k_s}$	Interface element shear stiffness
k_n	Interface element normal stiffness
L	Reinforcement length
L^m	Length of membrane element
L_c	Characteristic length of interface element
$[N]$	Shape function matrix
N_c	Bearing capacity factor due to cohesion
N_γ	Bearing capacity factor due to self-weight
P	Average footing pressure
P_f	Final footing pressure
P_i	Generalised nodal force
P_p	Total passive earth pressure
P_u	Ultimate bearing capacity
P	Vector of nodal forces
$\tilde{q}$	Surcharge
R	Footing radius in axisymmetric conditions
R_i	Unbalanced nodal load
R	Vector of global nodal co-ordinates
$\tilde{r}$	Radius
r'	Mapped co-ordinate vector, in terms of α
$\tilde{s_u}$	Undrained shear strength of clay
s_u^T	Undrained triaxial shear strength of clay
s_u^{PS}	Undrained plane strain shear strength of clay
T	Instantaneous membrane element thickness
t	Time
t_0	Initial reinforcement thickness
U	Vector of nodal velocities
$\tilde{U_i}$	Generalised nodal velocity
u'	Mapped velocity vector, in terms of α
$\tilde{u_r}$	Relative tangential velocity/slip
v_r	Relative normal velocity/separation
W_c	Clay width
W_P	Width of plastic failure zone in clay

X	Vector of global nodal co-ordinates
$\tilde{x}$	Horizontal distance from the footing centre-line
x_i	Generalised co-ordinate
α, β	Isoparametric reference co-ordinates
β	Load spread angle through the fill
δ	Vertical footing displacement
δ_f	Angle of friction on the footing base
$\dot{\varepsilon}$	Vector of strain rates
$\dot{\tilde{\varepsilon}}_L$	Longitudinal Hencky strain rate
$\dot{\varepsilon}_t$	Tangential Hencky strain rate
$\dot{\varepsilon}_\theta$	Circumferential Hencky strain rate
ϕ_{PS}	Plane strain friction angle of fill
ϕ_T	Triaxial friction angle of fill
ϕ_{cv}	Critical state friction angle
ϕ_i	Interface element friction angle
ϕ'	Mobilised friction angle
ϕ_i'	Mobilised friction angle at interface
γ_a	Degree-of-association
γ_c	Bulk unit weight of clay
γ_f	Bulk unit weight of fill
ν_c	Poisson's ratio of clay
ν_f	Poisson's ratio of fill
ν_r	Poisson's ratio of reinforcement
θ	Rotation angle
σ	Normal stress
σ_L	Longitudinal stress
σ_t	Tangential stress
σ_θ	Circumferential stress
σ_v	Vertical stress
σ	Vector of stresses
$\tilde{\sigma}^i$	Imposed normal footing stress on reinforcement
τ	Shear stress
τ_f	Shear stress at the footing base
ψ_{PS}	Plane strain dilation angle of the fill
ψ_i	Interface element dilation angle

CHAPTER 1:

INTRODUCTION

1.1 Geotextiles and Geomembranes

Geotextiles and geomembranes, broadly speaking, are synthetic fibres used to stabilise structures built of earth. The now widely accepted generic term for these non-natural materials is 'geosynthetics', which was coined by Dr. J. P. Giroud (1986) in his extensive and exhaustive review of geotextiles. Geosynthetics include permeable and impermeable materials that are either of a knitted, woven, or non-woven nature, as well as polymer grids and meshes.

There are many different practical applications of geosynthetics in civil engineering. They are often incorporated into geotechnical constructions, such as steep slopes, retaining walls, embankments and roads, in order to provide strength and reinforcement, or they can be used for erosion control, rockfall nets and gabion cages to protect the construction from weathering and deterioration. They are used also to control fluid transmission, either as impermeable liners to prevent leakage from beneath fluid storage tanks, canals, reservoirs, dams and waste disposal sites, or as permeable filters allowing fluid to pass through the system, but still retaining the soil on the upstream side.

The role of the geosynthetic membrane varies in each of the above applications. It can operate in the functions of Reinforcement, Separation, Filtration, Protection, Containment and Fluid Transmission. A comprehensive discussion and evaluation of these functions is given by both Koerner (1986) and John (1987).

Clearly, geosynthetic materials have become an integral part of geotechnical engineering constructions and the specific application considered in this dissertation is that of two-layer soil systems. The use of geosynthetics within two-layer soil systems is well-established, utilising the functions of reinforcement, separation, containment and filtration. Their construction typically consists of a geosynthetic material laid on the stripped soft clay subgrade with a layer of aggregate fill compacted on top, and their uses are multitudinous, for example, temporary working platforms, car parks, outlying aircraft runways, foundations of storage tanks and silos, forestry trails, haul roads, access ways and low-maintenance unpaved roadways. The majority of previous research into two-layer soil systems, by experimental and theoretical methods, has addressed the specific problem of reinforced unpaved road design, Figure 1.1, as reviewed in Chapter 2.

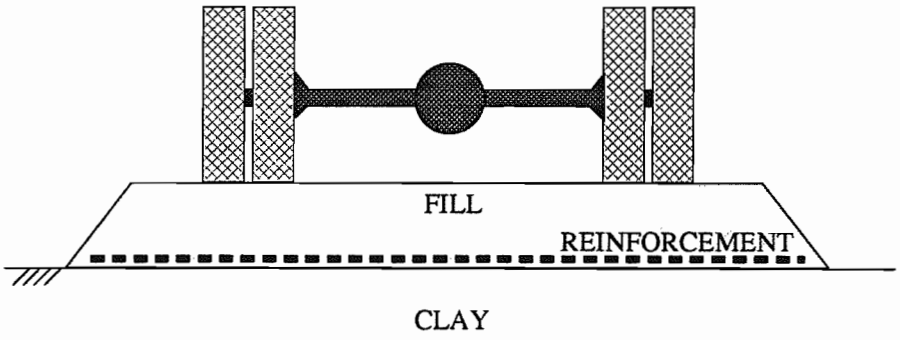

Figure 1.1: A Typical Reinforced Unpaved Road Section

1.2 Objectives of Research

The work described in Chapters 2 to 10 of this thesis has four main objectives. Firstly, to develop further the existing large strain finite element code OXFEM (initially developed by Burd (1986)) to include both plane strain and axisymmetric frictional interface elements, as well as axisymmetric membrane elements, so that the soil-reinforcement interaction of a two-layer soil system can be modelled accurately in both plane strain and axisymmetry. Secondly, to investigate and analyse numerically the mechanisms by which a geosynthetic membrane reinforces a plane strain and an axisymmetric system for large surface displacements. Thirdly, to conduct a detailed parametric study for each of the important

material properties and dimensions of a two-layer soil system and assess their influence on its performance, and finally, to evaluate the usefulness of the Houlsby *et al.* (1989) and Houlsby and Jewell (1990) analyses as appropriate design methods.

It is worthy of note that the plane strain results of the parametric study pre-date the development of the new axisymmetric membrane and interface elements and therefore comprise a greater proportion of the reported parametric analyses. An example of a practical application of the new axisymmetric interface elements to the analysis of the use of membranes in granular base foundations beneath oil storage tanks is described in Chapter 11.

CHAPTER 2:

ANALYSIS AND DESIGN OF REINFORCED TWO-LAYER SOIL SYSTEMS

2.1 Introduction

This chapter considers the problem of the design and analysis of reinforced two-layer soil systems, with particular reference to their common use as reinforced unpaved roads (Figure 1.1).

A synopsis of the different reinforcement mechanisms that have been identified as operating in a reinforced two-layer soil system is given in Section 2.2. This is followed by two reviews, firstly of the previous research conducted on model and full-scale two-layer soil systems, Section 2.3, and secondly of several finite element models specifically designed to analyse and investigate such reinforced soil systems, given in Section 2.4. Finally, Section 2.5 gives an overview of the currently available simple design methods for reinforced two-layer soil systems and their inherent understanding of the reinforcement mechanisms involved.

A key problem in designing and analysing a reinforced unpaved road is accounting for the effect of repeated loading. The majority of the currently available design methods initially design for the case of monotonic loading and then make empirical adjustments to the calculated allowable load to account for the repeated loading case, a procedure discussed further in Section 2.5.2. This methodology is clearly limited, since there is no rigorous analysis of the mechanics involved under repetitive loads, but it is generally accepted at present that such methods are valid and they are considered, in this thesis, to be the best

currently available. Therefore, based on the same assumptions, the research herein is concerned with understanding the mechanisms operating in a two-layer soil system subjected only to static monotonic loading.

2.2 Reinforcement Mechanisms

As a result of previous work in this area several mechanisms of reinforcement have been identified, or theorised, as acting in a reinforced two-layer soil system. These are described briefly below:-

Membrane Mechanism: Tensile forces are set up in the reinforcement by the shear stresses acting at the interface with the soil. During heavy, or repeated loading the aggregate layer deforms substantially, creating surface ruts which force the geotextile to deform, see Figure 2.1. If the tensile forces are coincident with an appreciable curvature of the reinforcement, then the normal stresses in the soil acting on each side of the reinforcement are unequal. This effect tends to reduce the normal stresses transmitted to the subgrade immediately underneath the load which increases the capacity of the road. This phenomenon is known as the *tensioned membrane effect.*

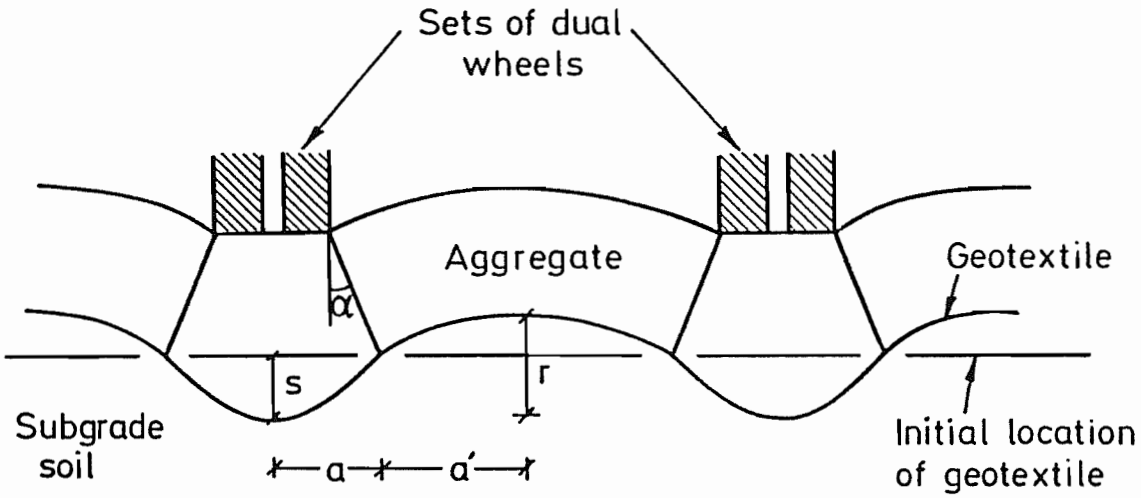

Figure 2.1: Assumed Profile of the Deformed Geotextile
(After Giroud and Noiray (1981))

Restraint Mechanisms: Lateral movements at the base of the aggregate layer and the surface of the subgrade are restrained by the reinforcement, which increases the strength and stiffness of the structure. This is achieved in two ways;

1) Through friction and/or interlock between the reinforcement and the surrounding soil, tensile strains at the base of the fill will be reduced. This mechanism effectively strengthens the fill layer by restricting any slip at the fill-reinforcement interface.

2) When the reinforcement deformation becomes appreciable it tends to restrain the heave movements of the subgrade on each side of the load through the membrane mechanism associated with the reversed curvature of the reinforcement. This effectively contributes an additional surcharge loading to the subgrade surface which will enhance its loading capabilities underneath the load.

Shear Stress Mechanism: As a vertical load is applied to the two-layer soil system lateral stresses develop in the fill layer which generate shear stresses at the base of the fill, see Figure 2.2. If reinforcement is absent these shear stresses are sustained directly by the subgrade and have the detrimental effect of lowering its bearing capacity, (Bolton (1979)). In the reinforced case the shear stresses at the fill base are assumed to be sustained by the reinforcement, rather than the subgrade, which causes a corresponding increase in the bearing capacity of the subgrade for vertical loads.

Improved Load Spread: By including a geotextile reinforcement at the base of the fill layer it is a commonly held belief that the wheel load distributes itself over a wider area on the subgrade surface, compared to the area under pressure in the unreinforced case. This wider load distribution would improve the subgrade bearing capacity. However, it is noteworthy that from the results presented herein this mechanism is not generally present.

Separation: A geotextile will prevent the loss of subbase material into the subgrade on a large scale, thereby ensuring retention of the full design thickness of the subbase even at large deformations. Through this continuity the subbase layer will fully maintain its mechanical properties. Geotextile reinforcement may act as a valuable separating layer on very soft subgrade and particularly under cyclic loading, since it is in these situations that

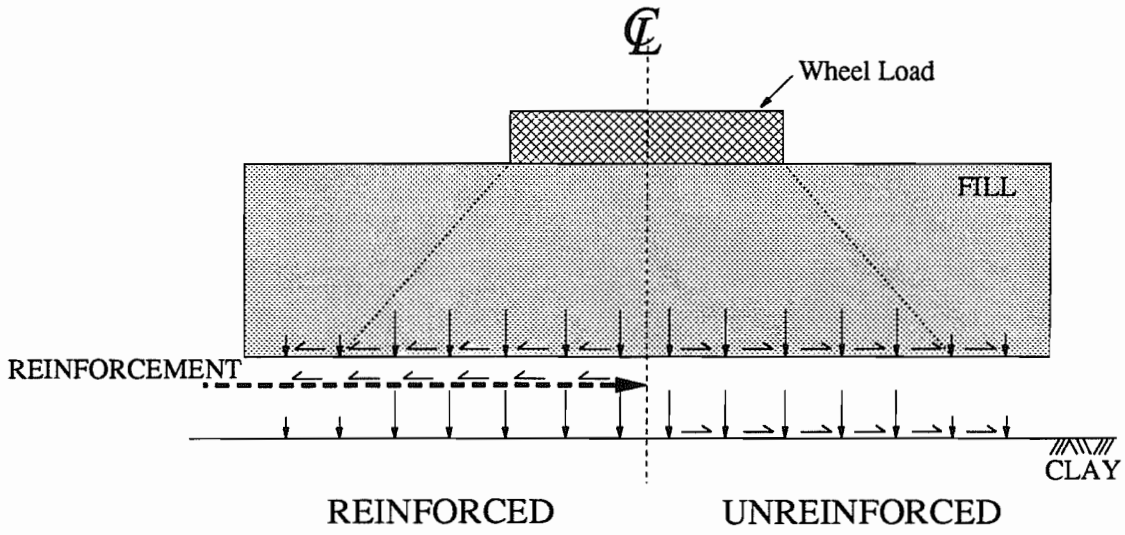

Figure 2.2: Shear Stress Mechanism of Reinforcement

progressive deterioration of the two-layer soil system will be increased due to the larger magnitude and/or rate of action of such detrimental mechanisms as the migration and mixing of the fill and soil particles and lateral movement of the subbase layer.

2.3 Previous Model and Full-Scale Studies

Numerous experimental studies on the problem of the design of reinforced two-layer soil systems, specifically reinforced unpaved roads, have been carried out in recent years. Several of these studies, Love (1984), Poran (1985), Fannin (1986) and Little (1992), are discussed in more detail below.

High quality model tests were conducted by Love (1984) to investigate the performance of a model geogrid in a quarter full-scale study of a reinforced unpaved road. These test results are summarised by Milligan and Love (1984), while Love *et al.* (1987) compares and discusses the experimental model results with the corresponding finite element modelling conducted by Burd (1986), which is described in Section 2.4. Simple plane strain monotonically loaded footing tests were carried out on systems consisting of a fill layer compacted onto a consolidated clay subgrade, both with and without a model grid placed

at their interface. Eighteen main tests were carried out for combinations of three different fill thicknesses ($D_f = 1.333B, 2.0B$ and $2.667B$ where B is the footing half width $= 37.5\ mm$) placed over clay of three different nominal strengths ($6\ kPa$, $9\ kPa$ and $14\ kPa$).

The resulting load-penetration data given by Love (1984) shows that the limit load, defined at a footing penetration of $50\ mm$, in each of the unreinforced cases is dependent on the clay strength, but virtually independent of the fill thickness, whereas in the reinforced cases the limit load is dependent on both clay strength and fill depth. It was further noted that in the initial elastic stages of testing there was very little difference between the reinforced and unreinforced systems, whereas in the plastic regimes of the load-penetration curves the reinforced responses were significantly stiffer compared to the unreinforced responses, an effect seen in all of the finite element parametric pressure-displacement responses presented later in this thesis. Love (1984) also showed that the zone of deformation in a reinforced test could be seen generally to extend approximately twice as deep into the clay as for an unreinforced test with the same fill thickness, clay strength and footing penetration (but a much smaller load). Additionally there was found to be much less fill material lost from immediately beneath the footing in the reinforced cases compared to the unreinforced cases where lateral movement of fill material occurred along the unreinforced fill-clay interface.

The explanation of why an increase in fill thickness does not significantly change the amount of load the unreinforced road can carry, is that the generated shear stresses at the fill base are also increased and they directly reduce the clay's load bearing capacity (the 'shear stress mechanism' in Section 2.2). Consequently the unreinforced road can only maintain an approximately constant ultimate load, despite the larger fill thickness, for a particular clay strength. In contrast, with the inclusion of a grid reinforcement there is a marked increase in the load carrying capacity of the system, which improves with increases of either the clay strength, or the fill depth. This is because the membrane prevents the detrimental shear stresses acting directly upon the clay surface and thus allows the clay to provide the full bearing capacity.

Large-scale plate loading laboratory investigations were carried out by Poran (1985) on soil-geogrid interaction, related to the bearing capacity of reinforced granular layers overlaying soft clay. The failure load, defined at the point were the vertical displacement of the square plate continued to increase throughout the first ten minutes after the load application, was attained in three loading/unloading cycles for each test. Poran (1985) found that Tensar grid reinforcement improves the load bearing capacity of such structures by 40-100% and reduces the vertical settlement, in comparison to the unreinforced, under relatively heavy loads. Different failure modes were observed for the unreinforced and reinforced tests. In the unreinforced tests significant punching of the plate into the base layer occurred, while no punching developed in the reinforced tests. This effect is mostly attributed by Poran (1985) to the confinement of the base material by the reinforcement (i.e. the restraint mechanism 1 discussed in Section 2.2), with an additional mechanism acting of an improved and more uniform load spread through the aggregate. The tensioned membrane effect is considered only important for very large displacements and therefore insignificant for normal bearing capacity applications.

Full-scale reinforced and unreinforced two-layer soil system trials, with monotonic loading of a single footing, and quarter scale model tests, for both monotonic and repeated loading using a dual footing, were performed by Fannin (1986) and discussed by Milligan *et al.* (1986) and (1989). The model tests showed that the failure mechanisms in the five-cycle repeated loading tests were the same as in the monotonic tests, which supports the argument for the common design practice of linking the two types of loading. In the cyclic tests the behaviour was identified as essentially one of low-cycle plastic fatigue, with deformations gradually accumulating with each cycle of loading at an ever accelerating rate until failure was reached. These repeated loading results compare well with the empirical fatigue curves derived from the extensive full-scale testing by Hammit (1970), for unreinforced unpaved roads, and by De Groot (1986), for reinforced unpaved roads, which are studies discussed further in Section 2.5.

From the full-scale monotonic tests conducted by Fannin (1986), with rectangular and circular footing plates involving an arrangement of compacted granular layers over a prepared London clay with a high strength polymer grid, it was discovered that directly

under the footing the grid maintained an interlocking action with the granular material throughout testing by an interpenetration of the particles into the grid apertures. Outside this region compaction of granular material during the preparation for testing had also caused the grid to interlock with the base of the granular layer. However, as a test proceeded upward heave movements of the deforming subgrade caused this interlock to be lost, with the grid being drawn increasingly into the clay. Fannin (1986) concluded that at moderate displacements the subgrade beyond the footing area would slide along the base of the granular layer and grid, but at large displacements it would 'flow' through the grid apertures.

The University of Nottingham completed a full-scale test of a geosynthetic reinforced haul road on the British Science and Engineering Research Council owned Soft Clay Site, at Bothkennar in Scotland (Little (1992)). Different geosynthetic manufacturers and the Universities of Nottingham and Oxford each designed two sections of the haul road circuit, one lower bound section with a life expectancy of 1,000 passes of an 80 *kN* axle load and one upper bound section for 10,000 passes, as explained in a technical note by Dawson and Little (1990). Failure by trafficking was deemed to occur at a rut depth of 150 *mm* , or if the geosynthetic ruptured. The Oxford sections of the haul road were designed by using the Houlsby *et al.* (1989) analytical method (reviewed in Section 2.5) and by running a series of plane strain, large displacement finite element analyses using OXFEM (see Section 2.4).

The final summary report by Dawson and Brown (1992) confirms that the basic mechanisms proposed by Houlsby *et al.* (1989), such as the shear stress mechanism, are correct, but that the tensioned membrane effect is unimportant at normal rut depths, which is in disagreement to the parametric study results presented in this thesis, where both mechanisms are found to be significant. Another important conclusion from the Bothkennar project is that internal aggregate compaction and/or the development of permanent shear strains can be a significant reason for rutting, which are factors that are almost impossible to accurately account for in an analytical or finite element study.

2.4 Finite Element Analyses

Finite element modelling has the advantages over experimental modelling that parameters may be varied easily and details of stresses and deformations throughout the system may be studied. This is particularly valuable for investigating the mechanisms acting at the unreinforced and reinforced interface between the fill and subgrade, which is extremely difficult to do in a model test.

Finite element numerical methods may be used to contribute to the design of reinforced two-layer soil systems in two general ways. Firstly, numerical models can be developed that may be used directly in the design of reinforced soil structures. Several numerical models have been developed that are capable of this function, four of these (Zeevaert (1980), Poran (1985), Kwok (1987) and Burd (1986)) are described briefly in this Section 2.4. These computer models, however, are not generally available to practising engineers and even if such numerical models were generally available it is clear that in most cases the use of such sophisticated design tools would be inappropriate, if only because of time and cost restraints. Nevertheless, finite element computer analyses can be incorporated into the design process, as discussed by Hird and Pyrah (1990). In this paper the authors describe the numerical modelling of an existing embankment reinforced at the base with a geogrid, using the finite element program CRISP. The authors consider that their finite element analysis could have played a significant role in providing guidance to the designer of the embankment. The second approach that may be adopted in the application of numerical models to design, is to use the theoretical calculation to investigate the mechanisms of reinforcement operating within a reinforced soil structure with the purpose of developing improved simple analytical design methods. While substantial progress has been made in developing analytical and limit equilibrium calculations for designing reinforced two-layer soil systems (Section 2.5), much work remains to be done to explore the deformation behaviour that occurs within them. Realistically this can be done only by employing numerical methods. The finite element studies described in this dissertation are intended to contribute to the understanding of the reinforcement mechanisms operating in a reinforced two-layer soil system in the manner of the second of these two approaches.

Zeevaert (1980) developed an axisymmetric finite element formulation which used eight node isoparametric elements to represent both the subgrade and fill, and an axisymmetric two node, linear displacement, two dimensional element to model the reinforcing material. The interfaces between the reinforcement elements and the fill above, as well as the subgrade below, are modelled by six noded linear spring elements which can account for both slip and separation of the mating surfaces. The nonlinear behaviour of the soil is described by a uniaxial stress-strain curve and the plasticity characteristics of each material are taken into account by use of the extended von Mises yield criterion proposed by Drucker and Prager (1952), which is limited to small strains, i.e. infinitesimal distortions. This yield criterion has a smooth yield surface that may be used to approximate the Mohr-Coulomb yield surfaces, but it is known to be a poor representation of real soil behaviour. Large or small displacements (i.e. rigid body movements) can be modelled by the finite element formulation through a process of updating the mesh geometry at each load increment. A 'no-tension' mathematical model is incorporated for the aggregate fill.

A very interesting phenomenon reported by Zeevaert (1980), is that the large displacement analyses exhibited greater footing deformations than for the small displacement option at the same footing load, and that this difference increased for decreasing fill thicknesses, i.e. a 10% larger footing displacement developed for the large displacement reinforced and unreinforced thick aggregate layer ($D_f = 2.33\,B$) analysis, compared to the equivalent small displacement analysis, and a 44% increase in displacement occurred for the thin layer ($D_f = 1.5\,B$), where B is the footing radius of 76 mm . This is contrary to the expected result, since a large displacement calculation accounts for the geometric non-linearities associated with the deformed system and therefore intrinsically promotes comparatively smaller deformations at higher loads, as explained and illustrated in Chapter 6 of this thesis. Therefore the finite element model presented by Zeevaert (1980) must be viewed with some strong reservations. Zeevaert (1980) does conclude, however, that the computed elastic-plastic deformations are smaller for a reinforced two-layer soil system, compared to an unreinforced, when subjected to the same footing load and that this reinforcing effect is more pronounced for a thinner aggregate layer, $D_f = 1.5\,B$, than for a thicker layer, $D_f = 2.33\,B$, as concluded also in Chapter 7. A limitation of the Zeevaert

(1980) study is that only one value of aggregate friction angle is used, whereas Chapter 7 illustrates that the amount of improvement obtained by including reinforcement is dependent upon both the aggregate thickness and the friction angle.

The finite element model proposed by Poran (1985) involves a plane strain analysis using a linear elastic 'composite layer' model for the geogrid-soil layer, where the reinforcement elements have the same properties as the surrounding granular material, but are overlaid by special beam-membrane four node elements which can model large deformation effects. The clay and sand are each modelled by almost identical discrete finite element formulations, differing only in that the clay is able to simulate consolidation and loading rate effects as necessary. The formulation is described as semi-discrete, since it does not model all of the components of the system individually, as would a fully discrete analysis (e.g. Burd (1986)), but alternatively it is not a fully composite analysis either, which would model the system as an equivalent orthotropic homogeneous continuum.

The finite element analyses presented by Poran (1985) display an interesting characteristic where the contours of vertical stress in the aggregate layer are modified by the inclusion of reinforcement, so that the fluctuations in the stress for the unreinforced case improve to a more uniform and a slightly wider distribution for the same footing displacement. This increased load spread effect, however, is not identified in the unreinforced and reinforced normal stress distribution plots and contours presented later in this thesis (e.g. Plates 6.3 and 6.4, Appendix 6B) and is thought to be a consequence of the semi-discrete formulation used. Poran (1985) makes a comparative study of the load-displacement results for the laboratory plate bearing tests (adjusted to plain strain conditions by applying relevant shape factors) and the equivalent finite element computations. A good correlation exists for the unreinforced case, but the load-displacement responses for the reinforced cases are much less comparable, because the finite element analyses predict a much stiffer response, such that the vertical displacements are estimated at about half those of the laboratory results for the same final loads.

Based on test results from investigations by Meyerhof (1974), Hanna and Meyerhof (1980), Giroud *et al.* (1984) and especially Milligan and Love (1984), as well as his own

experimental data, Poran (1985) proposes a simplified bearing capacity model for the analysis and design of footings placed on Tensar-geogrid reinforced granular bases overlaying soft clay. The tensioned membrane mechanism is considered insignificant by Poran (1985) and is therefore neglected, however the model does include the reinforcement effects of:

1) Confinement of the granular base and the clay so that the clay's plastic yield limit of $(\pi+2)\,s_u$ is adopted, rather than the elastic yield limit of $\pi\,s_u$ which is used in the unreinforced analysis.

2) Improved load distribution angle, determined empirically by incorporating test results from both previous studies and from the Poran (1985) investigation.

On comparison with other design methods (Section 2.5) for predicting footing pressures at failure for unreinforced two-layer soil systems, the Poran (1985) model shows good agreement. For predicting the footing pressure at failure for the reinforced case, however, the model underestimates previous test results by up to 25%.

Kwok (1987) considered the slightly different two-layer soil problem of embankments placed on reinforcement over a soft foundation layer, rather than the comparatively smaller monotonically loaded two-layer soil systems as considered by Zeevaert (1980), Poran (1985) and Burd (1986). Kwok (1987) used the plane strain finite element computer program CRISP (Britto and Gunn (1987)), which employs models of critical state soil mechanics, and incorporated special elements to model a reinforcement layer and the interfaces with the surrounding soil. The reinforcement was modelled by means of a line element with no bending stiffness and either a linear, or bi-linear axial force-extension relationship, while the interface elements permitted slip according to a Mohr-Coulomb criterion once the strength of the interface was exceeded. The embankment was modelled as an elastic-perfectly plastic material with a Mohr-Coulomb yield criterion and the foundation was modelled using the Modified Cam Clay model (Roscoe and Burland (1968)). The main conclusions of this work relevant to general reinforced two-layer soil systems, as described

in Hird and Kwok (1989) and (1990), are:

1) Sufficiently stiff and strong reinforcement can significantly reduce deformations within the subgrade. However an over-stiff reinforcement develops an excessively large tension without contributing significantly to an improvement in the load capacity. Therefore the benefit of increasing the reinforcement stiffness follows a pattern of strongly diminishing returns, (as substantiated in Chapter 8).

2) The reinforcement attracts shear stress, inducing tension, from both the fill and the subgrade, (as shown in Chapter 6).

The research work undertaken for this dissertation, on studies of reinforced and unreinforced two-layer soil systems, uses the finite element computer model OXFEM. This is a large displacement, large strain, finite element model that was initially developed by Burd (1986).

Burd (1986) describes a series of plane strain finite element predictions of the behaviour of a reinforced two-layer soil system consisting of a layer of fill compacted on top of a clay subgrade with rough, thin reinforcement placed at the interface. The numerical formulation has separate elements to model the soil and reinforcement and is specially designed to handle large deformations and large strains correctly (a full description of OXFEM is given in Chapter 3). The reinforcement was assumed perfectly rough, i.e. no slip or separation was allowed to occur, because the numerical model did not originally have the necessary interface elements incorporated. Later development of the computer program, as part of this research, involved installing special interface elements as described in Chapter 5.

In order to validate the mathematical model Burd (1986) conducted accurate back-analysis calculations of the eighteen experimental tests performed by Love (1984), (Section 2.3), using a consistent set of material properties. A number of general conclusions, relating to the behaviour of reinforced two-layer soil systems deforming in plane strain under the action of a single monotonic load, are derived from the results of these back-analysis

calculations:

1) The results clearly reproduce the important trend observed in the model tests that the reinforcement has a negligible effect on the load-penetration response at low surface deformations, but it becomes increasingly effective as displacements became appreciable.

2) For the cases studied by Burd (1986) the reinforcement was discovered to have little effect on the load spread action of the fill, as found for the parametric studies herein.

3) The reinforcement tended to reduce the shear stresses transmitted from the fill to the subgrade, i.e. the shear stress mechanism.

4) The numerical computations support the experimental findings of Love (1984) that the subgrade strength governs the load-displacement response of the system more strongly than the fill thickness.

Although Burd (1986) only considered the case of monotonic loading in plane strain, a development of that work is undertaken herein to deal with the additional case of axisymmetric monotonic loading (Chapters 4 and 5).

Finite element methods have become established as an important part of designing and analysing reinforced two-layer soil systems. However there are still some shortcomings associated with such computer modelling, for instance the practical requirement of sufficient computer capabilities and the need for accurate mathematical models. Additionally there are the limitations, shown in previous finite element studies, of needing to restrict the analyses to monotonic loading, or to a very low number of load cycles, rather than the realistic high-cyclic loading situation encountered for unpaved roads for example. There is also an apparent lack of extensive parametric studies to investigate the influences of various material properties.

2.5 Current Design Methods

There is clearly a need for analytical methods that may be used to predict the load-displacement characteristics of reinforced two-layer soil systems which practising engineers can use for design. Several design methods have therefore been proposed in recent years, based on simple analytical models of the reinforcement mechanism. The design models considered here are principally concerned with reinforced unpaved roads and are limited to the analysis of the road behaviour during a single static load application with adjustments made empirically for the cyclic loading case. This approach appears justified since Fannin (1986), (Section 2.3), found that the failure mechanisms under cyclic loading were the same as under monotonic loading.

2.5.1 Static Analyses

There have been many proposed design methods for reinforced unpaved roads, but only a few salient analyses for the static loading case are reviewed here, with an assessment of the particular limitations of each method given at the end of Section 2.5.1.

Giroud and Noiray (1981) describe a design method based on both the consideration of the 'tensioned membrane effect' and the subgrade confinement resulting from the curved nature of the geotextile after deformation, for the case of a plane strain reinforced unpaved road deforming under the action of a single application of a dual wheel load. The assumed mechanism of reinforcement is based on the link between footing displacement and membrane curvature. A pyramidal distribution of load through the aggregate layer is adopted and a constant value of $\tan^{-1} 0.6$ is taken for the load spread angle, irrespective of any other parameters. The deformed geotextile profile is assumed to follow a series of parabolae pinned at the initial plane of the fabric (see Figure 2.1), so that the average strain in the geotextile can be determined. The reinforcement tension is then evaluated as a function of the tensile stiffness and elongation of the membrane. In the reinforced case the reduction of pressure on the subgrade, due to the tension in the geotextile, is calculated and subtracted from the previously calculated pyramidal distribution. It is then suggested that this net load on the subgrade must be less than the ultimate bearing capacity of the subgrade which, due

to the additional confinement of the subgrade provided by the reinforcement, is given by the plastic bearing capacity factor, $(\pi + 2)$, in the reinforced case and the elastic limit bearing capacity, π, in the unreinforced case.

From the results of the finite element parametric study conducted herein (Chapters 7-10), it is established that the shape of the deformed membrane is not a constant parabola, but is dependent upon several factors including the fill thickness, the reinforcement stiffness and the clay strength. Additionally, the improvement in load capacity is not directly proportional to the reinforcement stiffness and the load spread angle is found to be strongly dependent upon the clay strength.

Giroud *et al.* (1984) present a development of the Giroud and Noiray (1981) quasi-static design procedure by proposing two additional reinforcement mechanisms in an attempt to explain the improvement in capacity attained at very small rut depths. One, is that the presence of reinforcement at the base of the fill layer improves the load spread performance of the fill. The other mechanism is that the reinforcement improves the structural behaviour of the road by acting as a separator between the fill and the clay which helps prevent progressive deterioration of the base layer. These two additional mechanisms are based on purely empirical relationships. Additionally the authors consider that the tensioned membrane effect is only significant if the rut depth is $\geq 150\ mm$ and is then accounted for by simply reducing the calculated granular layer thickness by 10%, otherwise it is neglected completely.

Sellmeijer *et al.* (1982) consider the specific reinforcement mechanisms of 'lateral restraint' and 'tensioned membrane action'. The design method initially assumes a bi-linear stress-deformation behaviour for the subgrade material with a separate elastic (Winkler spring type model) and plastic stress state analysis, although it is then concluded that the reinforcing effect of the membrane is negligible when the subsoil is in the elastic phase. A limit equilibrium equation is given relating the resultant of the combined traffic and aggregate loading on the upper side of the deformed geotextile and the subgrade reaction on the lower side, to the horizontal component of the tensile stress in the geotextile. It is suggested that the subgrade reaction stress is taken to be the failure stress estimated from a plastic analysis

based upon the Brinch Hansen (1970) bearing capacity formula, however no indication is given of what bearing capacity factor to use. Additionally, a superfluous design specification is made concerning firm fixity at the road edges (Chapter 9).

De Groot *et al.* (1986) present a design method and guidelines for the application of geotextiles in unpaved, or high volume paved roads, based on the calculation method presented by Sellmeijer *et al.* (1982). To account for the lateral restraint effects the bearing capacity factor is assumed to be 3.0 without reinforcement and 5.0 with reinforcement, based purely on empirical data obtained from field tests. A requirement is also made for a minimum 'anchorage length' of geotextile under the fill, over which the stress that has developed due to the strain in the heavily deformed part of the membrane will be reduced to zero by the friction on both sides of the geotextile (which is shown to be inaccurate in Chapter 9). An assessment of the separation function of a geotextile is presented in terms of its tear strength and puncture resistance. The problem of cyclic loading is also approached, as discussed in Section 2.5.2. Founded on these theories a step by step procedure is presented for designing the reinforced road.

Houlsby *et al.* (1989) propose a plane strain design method for reinforced unpaved roads where the benefit of reinforcement is considered only for the case of small surface displacements under a static monotonic load. Any improvement in the loading capacity of the reinforced road due to large deformations is excluded in this design approach. The valid justification of this is that the method is applicable to the design of hardstanding areas, such as car parks and working platforms, as well as unpaved roads, without the requirement for traffic channelling. The Houlsby *et al.* (1989) limit equilibrium method is based on the shear stress mechanism. In unreinforced roads the shear stresses at the fill base are sustained wholly by the subgrade, which has the detrimental effect of lowering the clay bearing capacity factor, N_c, to between $(2+\pi)$ and $(1+\pi/2)$, while in the reinforced road these shear stresses are assumed to be entirely removed by the membrane, leaving just a uniform vertical loading on the subgrade and allowing the maximum bearing capacity of $N_c = (2+\pi)$.

The Houlsby *et al.* (1989) analysis combines the unknown values of the bearing capacity of the clay subgrade and the horizontal stresses in the fill, which are linked by the

shear stresses developed at the unreinforced fill-clay interface. It is assumed that the fill beneath the footing is in a state of active failure and that outside of the loaded area it is in a general state of passive failure. The active and passive earth pressure coefficients give the corresponding lateral stresses in the fill. Through the equation of horizontal equilibrium the shear stresses acting at the base of the fill layer are evaluated, which gives the maximum value of the bearing capacity factor, and consequently the largest footing load can be calculated for a given fill depth.

Two of the assumptions made within the method are that, (1) the vertical load from the footing adopts an uniform pyramidal load distribution at an angle β through the fill layer and, (2) that an inward acting frictional force exists between the footing base and the fill layer surface, given by an angle of friction δ_f. The horizontal footing friction force is significant in the calculation of the maximum unreinforced footing load and the shear stresses at the fill base.

The reinforcement tension is estimated to be equal to the product of the total outward shear stress within the load spread area and the distance from the footing centre-line for which it acts. To carry this load there is an implicit requirement for a minimum value of both reinforcement stiffness and reinforcement length, although anchorage of the membrane is considered to be unnecessary since the reinforcement is under tension due to the outward acting shear stresses, even at small footing displacements. The possibility of failure within the fill is determined through a conventional bearing capacity investigation using the approximation of the self-weight bearing capacity factor, N_γ, suggested by Vesic (1975):-

$$N_\gamma = 2\,(\exp(\pi \tan\phi)\tan^2(45° + \phi/2) + 1)\tan\phi \qquad (2.1)$$

Houlsby and Jewell (1990) present an extended analysis of the Houlsby *et al.* (1989) theory for the case of axisymmetry, since in general a wheel loading approximates more closely to an axisymmetric rather than a plane strain style of loading. The analysis considers a static monotonic load, where the rut depth is again required to remain small. The authors suggest that such an analysis is justified since road designers generally want an assurance that their road will perform adequately at low surface deformation thus avoiding secondary loading, from water accumulation for example. The principle differences between the plane

strain and axisymmetric analyses are that, (1) the three-dimensional load spread gives a more rapid reduction in vertical stress within the fill, (2) the bearing capacity factors are somewhat higher (i.e. the full bearing capacity factor is 5.694 in axisymmetry, as opposed to $(\pi+2) \approx 5.14$ in plane strain), and (3) the passive pressures from the fill have greater influence. All three effects tend to increase the allowable loading on the pavement in comparison with the plane strain analysis. Design charts are developed for the unreinforced and reinforced cases.

Sellmeijer (1990) calculates the required strength of the geotextile needed to ensure that the membrane and the aggregate are both in a state of equilibrium. The method assumes that vertical equilibrium is established as indicated in Figure 2.3 (a), where σ_v is the limiting stress available from the subgrade, and hence the width of areas 2, 3 and 4 may be calculated. The resulting vertical deformation of the geotextile depends only on the shear modulus of the aggregate and through strain compatibility between the geotextile and aggregate the stiffness of the reinforcement may be computed. It is assumed that due to lateral restraint the subbase layer acts as a continuous slab and that it is reinforced by the geotextile in a similar way to a steel bar reinforcing concrete. Additionally, the mode of deformation experienced by the aggregate layer is taken to be one of shearing, rather than bending, Figure 2.3 (b). The other function of the geotextile is to maintain the integrity of the individual soil layers. The fill is considered to behave in an elasto-plastic manner and the mobilised friction angle, which is limited to values below the internal fill friction angle, is used in the analysis to control the degree of strain at the fill-reinforcement interface. An important parameter in the analysis is the friction angle between the geotextile and aggregate, which must be of an optimum value to ensure that the aggregate displays a slab effect. It is assumed that the reinforcement does not directly reduce the subgrade stress, but that the internal outward deformation of the aggregate is restricted by virtue of the aggregate-geotextile friction, thus improving the aggregate shear modulus and consequently reducing any rutting.

Developing a comprehensive analytical design method for reinforced two-layer soil systems is undoubtedly complex and therefore necessitates that certain simplifications and modifications are made to the actual problem. One particular difficulty is accounting for both the large and small displacement mechanisms operating in the system. For example,

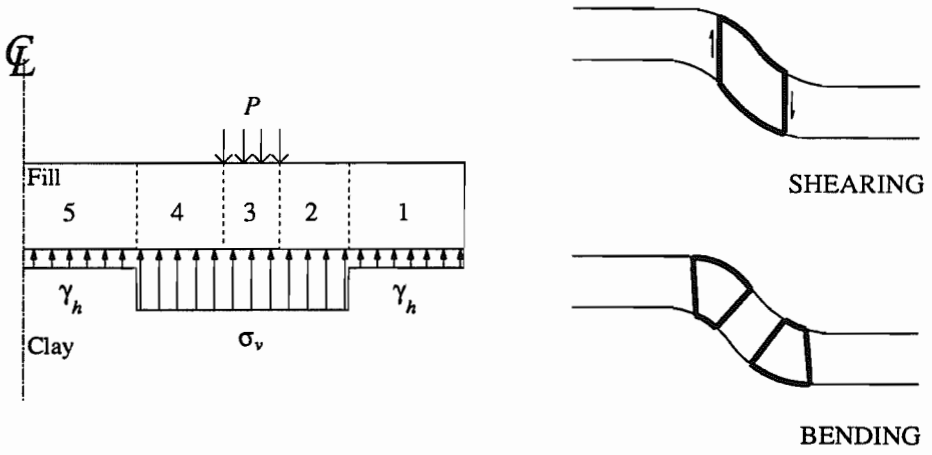

2.3 (a) Vertical Equilibrium (After Sellmeijer (1990))

2.3 (b) Modes of Aggregate Layer Deformation

Figure 2.3:

reinforced unpaved roads will ordinarily deform quite noticeably during service, however, it is found that there are significant improvements in the load bearing capacity of a reinforced two-layer soil system, compared to an unreinforced, even at very small rut depths, Love *et al.* (1987). Therefore, the design method needs to be based on an understanding of the mechanics involved at both small and large displacements.

The design procedures discussed in this Section 2.5.1 each have certain drawbacks. Giroud and Noiray (1981) base their design on the limiting, or inaccurate, assumptions that large displacements occur at the surface, that the deformed geotextile profile follows a series of parabolae pinned at the initial plane of the fabric and that the improvement in load capacity is linear with the reinforcement stiffness. Although Giroud *et al.* (1984) further develop the rudimentary theory of Giroud and Noiray (1981), such that reinforcement benefit is estimated for small rut depths and a load distribution improvement is calculated, there is still a simplistic analysis of the subgrade bearing capacity for an unreinforced road which does not consider any shear stress effects at the fill base. Sellmeijer *et al.* (1982) makes the erroneous assumptions that anchorage of the geotextile is necessary and that the reinforcement is sufficiently frictional so that slip cannot occur, in order to calculate the strain in the reinforcement due to the surface rutting. De Groot *et al.* (1986) base their design merely

on empirical evaluation of the subgrade bearing capacity, rather than any detailed mathematical investigation. The design method by Sellmeijer (1990) is inconsistent by assuming an elastic fill layer and plastic subgrade, and restrictive by considering the fill layer of a reinforced unpaved road as a stiff slab, whereas it has been found through this research that in fact the aggregate layer develops plastic yield (see Figure 6.5), before failure occurs in the clay subgrade.

Despite more sophisticated methods of analysis by Houlsby *et al.* (1989) and Houlsby and Jewell (1990) which calculate the lower varying bearing capacities obtainable for unreinforced cases, as opposed to the constant ultimate values used in fully reinforced cases, the methods do not consider the improved wheel loading that will undoubtedly be obtained due to the tensioned membrane mechanism. Additionally, there is no consideration of the exact reinforcement stiffness, only a prerequisite that it is sufficiently stiff to create a 'fully' reinforced condition and, moreover, it is assumed incorrectly that active fill failure conditions prevail directly beneath the footing (see Section 6.5.6). Although these analytical design methods are limited to purely small displacement, they are considered to be the most progressive and complete design methods for unpaved roads to date (Dawson and Brown (1992)) and they will therefore be used throughout the parametric investigation, carried out in Chapters 6 - 10, for a comparative study between the analytical solutions they provide and the finite element results obtained.

All these design methods are primarily concerned with the static loading case, but obviously a reinforced road is generally subjected to cyclic loading.

2.5.2 Cyclic Analyses

For most road applications the loads will be repetitive, which requires a modified approach in the design analysis.

The analytical design methods proposed by Giroud and Noiray (1981) and Giroud *et al.* (1984) are both quasi-static analyses which are converted to a cyclic loading design by applying an empirical formula relating the aggregate layer thickness to the amount of traffic

and to the soil properties for unreinforced unpaved roads. A set of empirically derived design charts are presented for the adjustment of the fill layer necessary to compensate for progressive deterioration of the clay subgrade due to repeated loading.

The De Groot *et al.* (1986) design method allows for cyclic loading conditions by deriving an equivalent static failure load, P_s, from an empirical fatigue relationship (equation (2.2)) derived from full-scale trafficking trials:-

$$P_s = P_n N^{0.161} \tag{2.2}$$

where P_n is the allowable axle load for N applications of the load.

Milligan *et al.* (1989), the companion paper of Houlsby *et al.* (1989), estimates the effect of repeated loading on a reinforced and unreinforced unpaved road by comparing the experimental cyclic loading data of Fannin (1986) (Section 2.3) with similar published studies by Delmas *et al.* (1986), De Groot *et al.* (1986) and Hammit (1970). It is suggested by Milligan *et al.* (1989) that the fatigue curve given by the De Groot *et al.* (1986) analysis (equation (2.2)) is currently the best available method for designing a reinforced unpaved road and that a similar fatigue relationship presented graphically by Hammit (1970) should be used for unreinforced roads. Milligan *et al.* (1989) provides an overall design procedure and worked examples of reinforced unpaved roads using the Houlsby *et al.* (1989) theory.

A paper by Davies and Bridle (1990) predicts the gradually increasing permanent deformation of a reinforced road due to repeated monotonic loading, by using a method based on the theorem of the minimum potential energy. The sum of the potential energy of the system and the work done by the applied load is equated to the sum of the strain energies in the subgrade, subbase and geogrid. Modelling of the permanent deformations remaining after a loading cycle, is achieved by choice of the properties of the subgrade. The cumulative deformation that occurs with repeated loading is modelled by variation of the material parameters of the subgrade. Although the analysis is compared to a restricted number of experimental model tests, promising results were obtained regarding its validity.

Despite the crudity of using empirical relationships established from field trials it is generally accepted at present that such methods are valid. This thesis, however, is concerned only with the static loading case and further discussion of cyclic loading is extraneous.

CHAPTER 3:

THE FINITE ELEMENT MODEL

3.1 Introduction

The research described in this thesis was carried out using the finite element program OXFEM, which is fully described in Burd (1986) and Yu (1990). This chapter provides a brief overview of aspects of the model that are not described in detail later in this thesis.

The program OXFEM is specifically designed to conduct large displacement, large strain calculations for both the plane strain and axisymmetric analyses of geotechnical structures. The specific application considered here is that of a two-layer soil system, with and without a layer of geosynthetic reinforcement placed between the soil layers, subjected to a single monotonic load.

3.2 Large Displacement Analyses

Some of the reinforcement mechanisms in a two-layer soil system only begin to operate at large surface displacements, e.g. the tensioned membrane effect, as discussed in Section 2.2. The numerical analysis, therefore, needs to be able to handle accurately any geometric non-linearity that may occur during deformation, i.e. it needs to be a large strain formulation. In OXFEM an Updated Lagrangian description of the deformation is used (i.e. the reference state is updated as the calculation proceeds, hence all the strain rates are related to the current mesh configuration), with extra non-linear terms included in the finite element stiffness

equations to account for geometric non-linearities and the addition of the Jaumann stress rate in the constitutive equations to account for large rotation effects. These large displacement characteristics are discussed more fully in the following sections.

3.2.1 Description of Kinematics

By using a Lagrangian reference system in continuum mechanics the deformation of a body subjected to large displacements is uniquely defined by a vector equation of the form:-

$$x_i = x_i\,(a_i\,,\,t) \tag{3.1}$$

where the reference position (at time $t = 0$) of a particular point within the material is described by the co-ordinate vector, a_i , relative to some fixed origin. After a finite time interval ($t = T$) the same material point will have moved to a new position described by the vector, x_i , in the same reference frame. This Updated Lagrangian description of kinematics, where the reference position is updated as the calculation proceeds, has been used for all the OXFEM finite element calculations discussed herein.

3.2.2 Objective Stress Rates

The objective stress rate adopted in the OXFEM large strain calculations is the Jaumann stress rate (Jaumann (1911)). The requirement of 'objectivity' is that when a material experiences rigid body motion, or rotation, the stress rate used in the constitutive equations must be zero.

A unique advantage of the Jaumann definition is that a zero stress rate represents a stationary behaviour of the stress invariants and similarly of the yield function for an isotropic material. However, the Jaumann stress rate does have the restriction that for problems involving large shear strains, i.e. greater than unity, then physically unrealistic solutions may be given. Despite this limitation the original Jaumann stress rate has been used in this study since the shear strains are not expected to be excessively large.

3.3 Continuum Elements to Model Soil

In order to ascertain whether a particular element assemblage is suitable for accurate elasto-plastic analysis Nagtegaal *et al.* (1974) proposed a criterion where it is necessary to evaluate the number of degrees-of-freedom per constraint for the limiting case of a very fine mesh. If this ratio is less than one, convergence to the true limit load will generally not be obtained.

Sloan (1981) applies this criterion to a large variety of triangular and serendipity elements for both the plane strain and axisymmetric cases. Sloan concludes that for plane strain problems of undrained soil behaviour, where the constant volume condition must be maintained, (i.e. material is incompressible) the majority of triangular and serendipity elements in common usage are suitable for predicting collapse loads accurately. The noticeable exception being the plane strain four-noded quadrilateral element. However, in the case of axisymmetric problems Sloan shows that only the fifteen-noded cubic strain triangle, or the twenty five-noded quadrilateral element, (or higher orders if desired) give a ratio of the number of degrees-of-freedom per constraint greater than one.

In all the finite element calculations reported in this thesis isoparametric triangular continuum elements are used to represent the soil medium, i.e. the equations describing the shape of the element boundaries are of the same order as those describing the variation of the nodal unknown (e.g. displacements) across the element. For the plane strain analyses six-noded elements are implemented, while fifteen-noded elements are used for the axisymmetric case, Figure 3.1, since these are the minimum number of nodes necessary to predict collapse loads accurately.

The specific finite element equations for the six-noded plane strain triangular continuum element are given in Burd (1986) and for the fifteen-noded axisymmetric continuum element see Teh (1987).

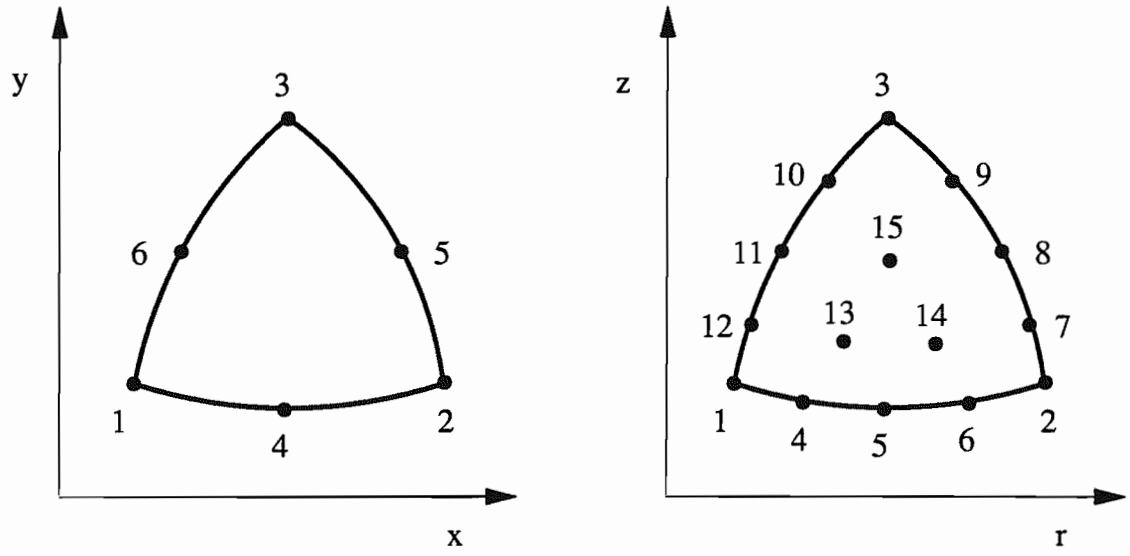

Six-noded Plane Strain **Fifteen-noded Axisymmetric**

Figure 3.1: Triangular Continuum Elements

3.4 Global Solution Scheme

The governing equations in finite element analysis are derived from the principle of virtual work, which states that the external applied loads, $\underset{\sim}{P}$, must be in equilibrium with the current internal stresses, $\underset{\sim}{\sigma}$. This is usually expressed in matrix form (Zienkiewicz (1977)) as:-

$$\underset{\sim}{P} = \int_E [B]^T \underset{\sim}{\sigma} \, dV \tag{3.2}$$

where the integration is performed over the element and the matrix $[B]$ relates the nodal velocities vector, $\underset{\sim}{U}$, to the strain rate vector, $\dot{\underset{\sim}{\varepsilon}}$, as follows:-

$$\dot{\underset{\sim}{\varepsilon}} = [B] \underset{\sim}{U} \tag{3.3}$$

where the superior dot denotes differentiation with respect to time.

The matrix $[B]$ depends on the strain definitions and element shape functions used to specify the displacement field throughout the element. By introducing the elasto-plastic material stiffness matrix, $[D]^{EP}$, which defines the relevant stress-strain relationship such that:-

$$\dot{\underset{\sim}{\sigma}} = [D]^{EP} \dot{\underset{\sim}{\varepsilon}} \tag{3.4}$$

equation (3.2) can be differentiated and written in terms of the nodal force rates and nodal velocities as:-

$$\dot{\underset{\sim}{P}} = [K] \underset{\sim}{U} \tag{3.5}$$

where $[K]$ is the tangential incremental stiffness matrix and is expressed as:-

$$[K] = \int_E [B]^T [D]^{EP} [B] \; dV \tag{3.6}$$

The specific incremental stiffness matrix for the plane strain case is defined by Burd (1986) as:-

$$[K]_{PS} = \int \int_E \{ [B]^T ([D]^{EP} + [R]) [B] \, det[J] + [C]_{PS} \} \; d\alpha \, d\beta \tag{3.7}$$

and the axisymmetric incremental stiffness matrix is defined by Teh (1987) as:-

$$[K]_{Axi} = 2\pi \int \int_E \{ [B]^T ([D]^{EP} + [R]) [B] \, r \, det[J] + [C]_{Axi} \} \; d\alpha \, d\beta \tag{3.8}$$

where α and β are the reference co-ordinates, r is the radius, $[J]$ is the Jacobian of the transformation from global to reference co-ordinates, the matrix $[R]$ accounts for the effects of element rotation and the matrices $[C]_{PS}$ and $[C]_{Axi}$ are interpreted as the distortion rate matrices. The stiffness matrices, $[K]_{PS}$ and $[K]_{Axi}$, therefore contain the conventional small displacement terms as well as an additional term, $[C]$, which accounts for the rate of change

of element geometry and is different for the plane strain and axisymmetric cases. The plane strain non-symmetrical distortion rate matrix is detailed by Burd (1986) and is obtained by expanding the following expression on a term-by-term basis.

$$[C]_{PS}\,\underset{\sim}{\dot{U}} \;=\; \{\,[B]^T \dot{det}[J]\,\}\,\underset{\sim}{\sigma} \tag{3.9}$$

The axisymmetric non-symmetrical distortion rate matrix is obtained by Teh (1987) through combining two of the terms in the resulting integrand, i.e.:-

$$[C]_{Axi}\,\underset{\sim}{\dot{U}} \;=\; \{\,[B]^T \dot{det}[J]\,\}\,\underset{\sim}{\sigma}\,r \;+\; [B]^T\,\underset{\sim}{\sigma}\,\dot{r}\,det[J] \tag{3.10}$$

In finite element problems where material and/or geometric non-linearities exist, as in the large displacement two-layer soil system analyses reported in this thesis, the resulting equations are non-linear and must be solved using an appropriate algorithm. The chosen incremental solution procedure implemented in OXFEM is described by Sloan (1981) as the 'modified Euler scheme'. A schematic representation of this scheme for a one degree-of-freedom system is presented in Figure 3.2. The exact load-displacement curve is approximated by a series of straight lines having a slope equal to that of the exact curve at the start of the increment. At the end of each increment of load, or displacement, the nodal forces corresponding to the equilibrium imbalance are calculated and equilibrium is restored by applying these out-of-balance loads in the opposite direction during the next load increment.

In a displacement controlled calculation the nodal force, P_i, in equilibrium with the prescribed nodal displacement, U_i, at the start of the i^{th} load step is used in equation (3.5) to obtain the incremental nodal force, ΔF_{i+1}. The individual element stiffness matrices are calculated and then assembled and inverted using a Frontal Solution algorithm.

The Frontal Solution, as outlined by Bathe (1982) and implemented in OXFEM by Burd (1986), is in principle a Gauss elimination procedure. The stiffness matrix of equation (3.6) is invariably calculated using a Gaussian quadrature scheme. The relevant order of the Gaussian quadrature scheme must be determined from the degree of the polynomial to be evaluated (see Section 4.2.2). However, the accuracy of the integration is affected when

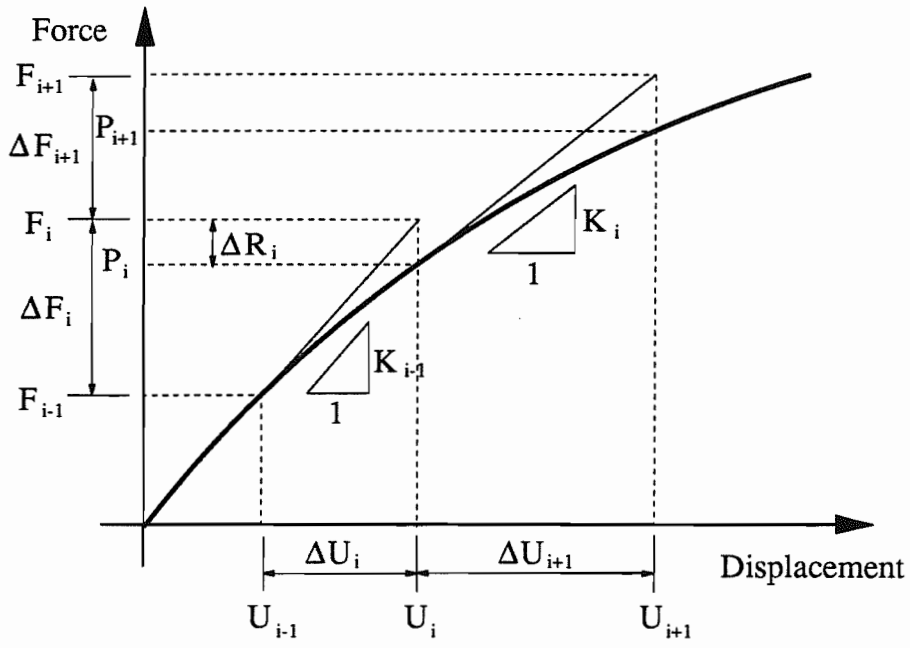

Figure 3.2: Modified Euler Solution Scheme

(After Sloan (1981))

large element distortion occurs and the calculations cannot be considered exact for a large displacement finite element analysis. For the six-noded plane strain elements a three-point Gauss rule is used, while the fifteen-noded axisymmetric elements use a sixteen-point Gauss rule (Britto and Gunn (1987)).

The set of Gauss point stress increments, $\Delta\underset{\sim}{\sigma}$, corresponding to the set of incremental nodal displacements, ΔU_{i+1}, are then calculated using an integration of the form:-

$$\Delta\underset{\sim}{\sigma} = \int_t^{t+\Delta t} [D]^{EP} \dot{\underset{\sim}{\varepsilon}}\, dt \tag{3.11}$$

where the integration is performed over the time step Δt. A complete description of the 'stress update' calculations is given in Burd (1986) and Teh (1987) for the plane strain and axisymmetric continuum elements and in Chapters 4 and 5 for the new axisymmetric membrane and interface elements, respectively.

At the end of each step the nodal loads, P_i, equivalent to the updated stresses are calculated from the virtual work equation (3.2). A set of unbalanced nodal loads, ΔR_i, are then determined and applied as an equilibrium correction during the next displacement increment.

3.5 Constitutive Behaviour

The clay subgrade and the granular fill materials of a two-layer soil system require different constitutive laws in order to numerically model their behaviour appropriately. Linear-elastic perfectly-plastic models of behaviour are used in OXFEM to simulate the two soil materials.

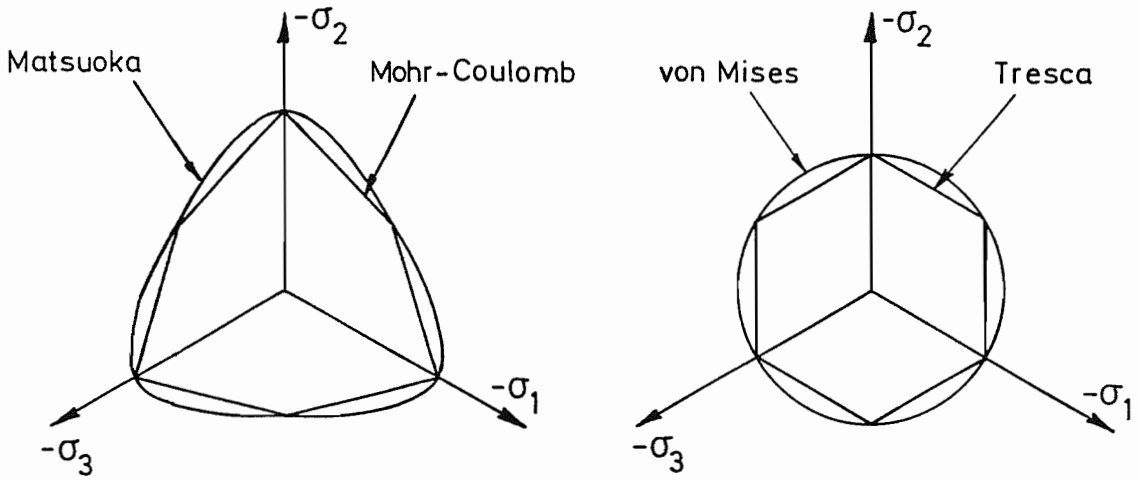

Figure 3.3: Comparison of Yield Surfaces
(After Burd (1986))

It is assumed that the loading on the subgrade is sufficiently rapid to give an undrained response and consequently is modelled using a 'total stress' approach. The von Mises plasticity yield criterion (Calladine (1985)), shown in Figure 3.3 for a section through the yield loci in the π plane, is used to model the cohesive clay. The plastic strain rates are derived from a fully associated flow rule which gives zero plastic dilation rate and is therefore suitable to the modelling of undrained clay behaviour, as discussed by Wroth and Houlsby

(1985). A fully associated flow rule requires that the plastic potential and the von Mises yield functions are exactly identical when plotted together using consistent axes and the plastic strains are then normal to the yield surface.

The fill is assumed sufficiently permeable not to allow pore pressures to occur during the loading, hence total and effective stresses are equal. It is represented as a frictional material using a non-associated linear elastic perfectly-plastic model based on the Matsuoka yield criterion (Matsuoka (1976)), illustrated in Figure 3.3. By using a non-associated flow rule the dilation characteristics of the soil are specified independently from the friction angle. A parameter termed the degree-of-association, γ_a , is introduced, which when set to unity the model of behaviour reduces to the full association case and when γ_a is zero the dilation rate is zero. The material behaviour for the case when the dilation rate lies between these two extremes is obtained by taking a weighted average of the plastic strain rates that give full and zero dilation.

Alternative yield functions such as the Tresca and Mohr-Coulomb models, (shown in Figure 3.3) commonly used to represent cohesive and frictional soils respectively, contain discontinuous yield surfaces with edges at which the yield function is not differentiable. In axisymmetric loading conditions, particularly, these singularities can have an important effect (Sloan (1981)). However, the von Mises and Matsuoka yield functions have the advantage that they are everywhere differentiable (except at the origin for the Matsuoka model). A full description of the approach used in implementing these formulations is given in Burd and Houlsby (1989) and Burd (1986).

CHAPTER 4:

FORMULATION OF THE MEMBRANE ELEMENTS

4.1 Introduction

This chapter is devoted to the description of the formulation of an axisymmetric membrane element possessing a finite axial stiffness, but a zero bending stiffness. The formulation intrinsically follows the approach described by Burd and Houlsby (1986) for a plane strain membrane element. However, that formulation needs to be modified for the axisymmetric case because of the difference in strain arrangement.

This axisymmetric membrane element effectively models a continuous sheet of material. It assumes that the membrane possesses isotropic material properties, where the material stiffness is the same for the tangential and circumferential directions.

The finite element equations are based on an Updated Lagrangian description of deformation, in a similar manner to the continuum element formulation described in Chapter 3. The Updated Lagrangian description of deformation lends itself well to the use of the Hencky strain rate to define the material behaviour of the membrane. Therefore, for this particular formulation, the material is assumed to be linearly elastic with respect to Hencky strain. In general, the stiffness equations derived using this approach will be different from those derived for a material that is assumed linearly elastic with respect to some alternative strain definition.

The proceeding sections include a detailed account of the finite element formulation for the new axisymmetric membrane element, followed by a brief synopsis of how this formulation differs to that of the established plane strain membrane element given by Burd and Houlsby (1986) and concluding with a set of rigorous test analyses.

4.2 Axisymmetric Membrane Element Formulation

The large strain finite element formulation of the new axisymmetric membrane element is based on an isoparametric approach, i.e. the shape functions defining the element geometry and the nodal displacements are the same. The formulation takes account of the effects of large strains and rotations by calculating the incremental strains generated at each step of the analysis and continuously updating these, along with the associated stresses, throughout the calculation.

In an axisymmetric problem any tangential displacement of the membrane naturally creates a tangential strain and thus a tangential stress σ_t, but it additionally induces a strain in the circumferential direction and therefore an associated circumferential stress, σ_θ, exists, as shown in Figure 4.1. For this particular formulation the membrane is considered to be of an infinitesimal initial thickness, t_0, and consequently the normal stress, σ_n, acting in the membrane will be comparatively very much smaller in relation to the in-plane stresses and can therefore be neglected. The variation of the membrane thickness is accounted for at each increment of load. The one-dimensional membrane element is also assumed to have zero bending moment and therefore no shear stress component needs to be considered within the element. Consequently it is only the tangential and circumferential stresses that are calculated in this new axisymmetric membrane formulation.

The axisymmetric formulation described in this chapter is applicable to membrane elements of arbitrary order and is therefore presented in a general form. The specific equations for the case of the five-noded element are presented in Appendix 4A.

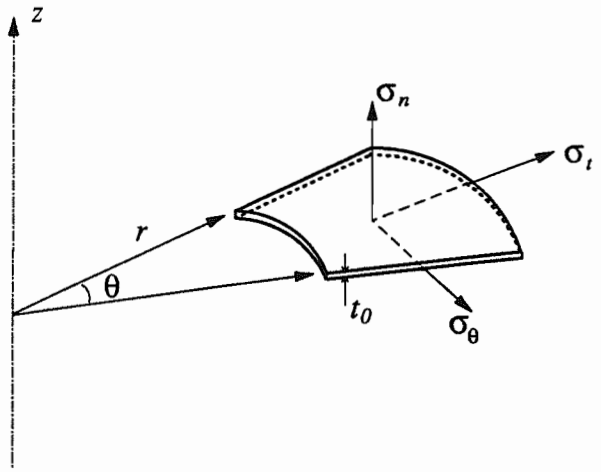

$$\sigma_n \ll \sigma_t , \ \sigma_\theta$$

Figure 4.1: Stresses in the Axisymmetric Membrane

4.2.1 Strain Definitions

The tangential and circumferential strains are individually defined in terms of the Hencky strain rate. Consider the tangential displacement of an infinitesimal portion of the membrane during an infinitesimal time step *dt*, as shown in Figure 4.2. Cylindrical co-ordinates are denoted by *r*, *z* and *u*, *v* are the velocities in the *r*, *z* directions respectively.

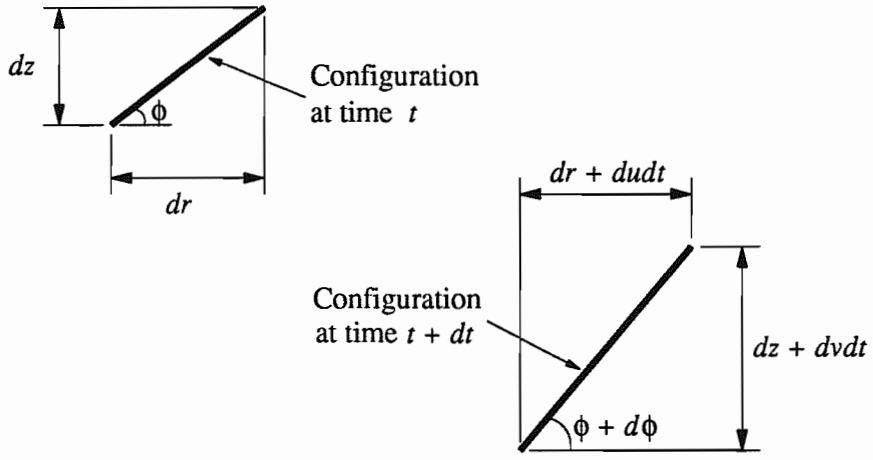

Figure 4.2: Displacements in a Membrane Element

The fractional increase in the length of the portion is:-

$$\frac{[\,(dr+dudt)^2+(dz+dvdt)^2\,]^{1/2} - [\,dr^2+dz^2\,]^{1/2}}{[\,dr^2+dz^2\,]^{1/2}} = \frac{dr\,du+dz\,dv}{dr^2+dz^2}\,dt \tag{4.1}$$

where higher order displacement terms are ignored. The tangential Hencky strain rate, $\dot{\varepsilon}_t$, can therefore be written:-

$$\dot{\varepsilon}_t = \frac{d\varepsilon_t}{dt} = \frac{dr\,du + dz\,dv}{dr^2 + dz^2} \tag{4.2}$$

where the superior dot denotes differentiation with respect to time.

The circumferential Hencky strain rate, $\dot{\varepsilon}_\theta$, is automatically given by the scalar value:-

$$\dot{\varepsilon}_\theta = \frac{u}{r} \tag{4.3}$$

(See Slater (1977), or Timoshenko and Goodier (1951)).

In order to develop the relationships between strain rates and nodal velocities, an axisymmetric isoparametric membrane element with N nodes is considered. Each node has two degrees of freedom. The global cylindrical co-ordinates of a point in the element are r, z and these are mapped onto a single reference co-ordinate α, as shown in Figure 4.3.

The vector of global co-ordinates of an arbitrary point in the element, $\underset{\sim}{r}^T = [\,r \quad z\,]$, is related to the vector of global nodal co-ordinates $\underset{\sim}{R}$, by:-

$$\underset{\sim}{r} = [N]\,\underset{\sim}{R} \tag{4.4}$$

where $[N]$, the shape function matrix, is a function of α. In a similar way the velocity vector of the same arbitrary point, $\underset{\sim}{u}^T = [\,u \quad v\,]$, is related to the nodal velocity vector $\underset{\sim}{U}$ by:-

$$\underset{\sim}{u} = [N]\,\underset{\sim}{U} \tag{4.5}$$

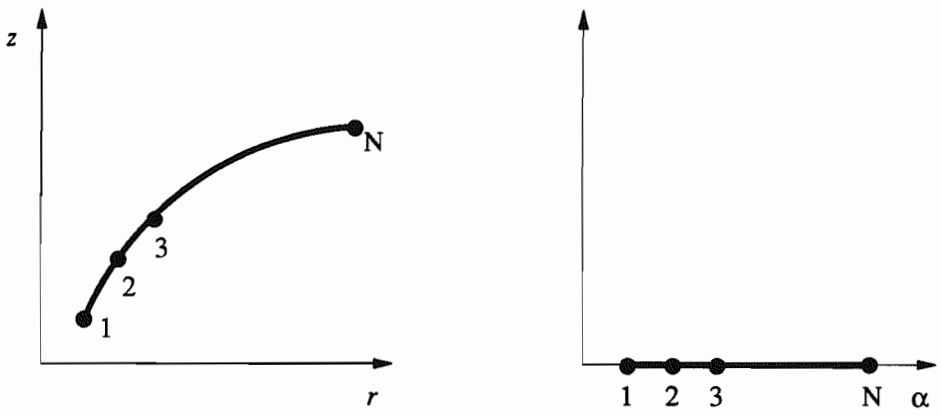

Parent Element **Mapped Element**

Figure 4.3: Mapping for an Axisymmetric Membrane Element

Differentiating these two equations (4.4) and (4.5) with respect to α and denoting this with a prime, gives:-

$$\underset{\sim}{r'} = [N']\,\underset{\sim}{R} \tag{4.6}$$

and:-

$$\underset{\sim}{u'} = [N']\,\underset{\sim}{U} \tag{4.7}$$

The tangential Hencky strain rate equation (4.2) can be written in terms of the mapped co-ordinate vector $\underset{\sim}{r'}$ and the mapped velocity vector $\underset{\sim}{u'}$, as:-

$$\dot{\varepsilon}_t = \frac{\frac{dr}{d\alpha}\frac{du}{d\alpha} + \frac{dz}{d\alpha}\frac{dv}{d\alpha}}{\left[\frac{dr}{d\alpha}\right]^2 + \left[\frac{dz}{d\alpha}\right]^2} = \frac{\left(\underset{\sim}{r'}\right)^T \underset{\sim}{u'}}{\left(\underset{\sim}{r'}\right)^T \underset{\sim}{r'}} \tag{4.8}$$

which can be re-arranged, by substituting equations (4.6) and (4.7), to:-

$$\dot{\varepsilon}_t = \frac{\underset{\sim}{R}^T [N']^T [N'] \underset{\sim}{U}}{\underset{\sim}{R}^T [N']^T [N'] \underset{\sim}{R}} \tag{4.9}$$

The denominator of the expression given in equation (4.9) can be denoted by J^2, where J represents the Jacobian of the transformation from parent to reference co-ordinates and is given by:-

$$J^2 = \left(\frac{dr}{d\alpha}\right)^2 + \left(\frac{dz}{d\alpha}\right)^2 \tag{4.10}$$

Differentiating equation (4.10) with respect to time gives:-

$$\begin{aligned} 2J\dot{J} &= 2\left(\frac{dr}{d\alpha}\right)\left(\frac{d\dot{r}}{d\alpha}\right) + 2\left(\frac{dz}{d\alpha}\right)\left(\frac{d\dot{z}}{d\alpha}\right) \\ &= 2\left(\frac{dr}{d\alpha}\right)\left(\frac{du}{d\alpha}\right) + 2\left(\frac{dz}{d\alpha}\right)\left(\frac{dv}{d\alpha}\right) \end{aligned} \tag{4.11}$$

and by substituting equations (4.6) and (4.7), this re-arranges to:-

$$\dot{J} = \frac{\underset{\sim}{R}^T [N']^T [N'] \underset{\sim}{U}}{J} \tag{4.12}$$

Thus, equation (4.9) can be written in the simplified form:-

$$\dot{\varepsilon}_t = \frac{\dot{J}}{J} \tag{4.13}$$

Rewriting the circumferential strain rate equation (4.3) in terms of the global co-ordinate vector $\underset{\sim}{r}$ and the velocity vector $\underset{\sim}{u}$, gives:-

$$\dot{\varepsilon}_\theta = \frac{\dot{r}}{r} = \frac{\underset{\sim}{k}\,[N]\,\underset{\sim}{U}}{\underset{\sim}{k}\,[N]\,\underset{\sim}{R}} \tag{4.14}$$

where the vector constant $\underset{\sim}{k} = [\ 1 \quad 0\ ]$ is introduced so that the radius r is equal to the scalar value of $\underset{\sim}{k}\,[N]\,\underset{\sim}{R}$

By using the tangential and circumferential strain rates defined by equations (4.9) and (4.14) respectively, the strain rate vector, $\dot{\underset{\sim}{\varepsilon}}$, may be written as:-

$$\dot{\underset{\sim}{\varepsilon}} = \begin{bmatrix} \dot{\varepsilon}_t \\ \dot{\varepsilon}_\theta \end{bmatrix} = \begin{bmatrix} \dfrac{\underset{\sim}{R}^T [N']^T [N']}{J^2} \\ \dfrac{\underset{\sim}{k}\,[N]}{\underset{\sim}{k}\,[N]\,\underset{\sim}{R}} \end{bmatrix} \underset{\sim}{U} = [B]\,\underset{\sim}{U} \tag{4.15}$$

where the $[B]$ matrix relates the nodal velocity vector $\underset{\sim}{U}$ to the strain rate vector $\dot{\underset{\sim}{\varepsilon}}$.

4.2.2 Formulation of the Finite Element Equations

By the principle of virtual work:-

$$\underset{\sim}{U}^{*T}\,\underset{\sim}{P} = \int_E \dot{\underset{\sim}{\varepsilon}}^{*T}\,\underset{\sim}{\sigma}\ dV \tag{4.16}$$

Where $\underset{\sim}{U}^*$ is a set of virtual nodal velocities and $\dot{\underset{\sim}{\varepsilon}}^*$ is the vector of the compatible tangential and circumferential strain rates. The vector of nodal forces, denoted as $\underset{\sim}{P}$, is in equilibrium with the stress vector $\underset{\sim}{\sigma}^T = [\ \sigma_t \quad \sigma_\theta\ ]$, and the integration is performed over each individual element.

Substituting the strain rate vector, equation (4.15), into equation (4.16) gives:-

$$\underset{\sim}{U}^{*T}\,\underset{\sim}{P} = \int_E \underset{\sim}{U}^{*T}\,[B]^T\,\underset{\sim}{\sigma}\ dV \tag{4.17}$$

The elemental volume dV may be written as:-

$$dV = 2\pi r J T \quad d\alpha \tag{4.18}$$

where T is the instantaneous thickness of the membrane element and $J\ d\alpha$ can be interpreted as representing the tangential length of an infinitesimal element within the membrane. Since the virtual work expression must hold for arbitrary nodal velocities, it follows that equation (4.17) can be re-arranged to give the nodal forces as:-

$$\underset{\sim}{P} = 2\pi \int_E [B]^T \underset{\sim}{\sigma}\, r J T \quad d\alpha \tag{4.19}$$

Equation (4.19) may be differentiated with respect to time to give an expression for the nodal force rate:-

$$\dot{\underset{\sim}{P}} = 2\pi \int_E \{ [B]^T \dot{\underset{\sim}{\sigma}}\, r J T + [\dot{B}]^T \underset{\sim}{\sigma}\, r J T + [B]^T \underset{\sim}{\sigma}\, \dot{r} J T + [B]^T \underset{\sim}{\sigma}\, r \dot{J} T + [B]^T \underset{\sim}{\sigma}\, r J \dot{T} \} \quad d\alpha \tag{4.20}$$

which can be simplified to:-

$$\dot{\underset{\sim}{P}} = [K]\, \underset{\sim}{U} \tag{4.21}$$

where $[K]$ is the incremental stiffness matrix given by:-

$$[K] = 2\pi \int_E \{ [B]^T [D] [B]\, r J T + [C] \} \quad d\alpha \tag{4.22}$$

The material stiffness matrix, $[D]$, in equation (4.22) relates the stress rate vector $\dot{\underset{\sim}{\sigma}}$ to the strain rate vector $\dot{\underset{\sim}{\varepsilon}}$ by:-

$$\dot{\underset{\sim}{\sigma}} = [D]\, \dot{\underset{\sim}{\varepsilon}} \tag{4.23}$$

Note that it is possible to express the $[K]$ matrix in a variety of forms. The form given in equation (4.22) is chosen to be consistent with the axisymmetric continuum formulation (Teh (1987)), equation (3.8). The first term in the integrand of the incremental stiffness matrix is the conventional small displacement term. The second term, $[C]$, contains additional terms that need to be included to represent the effect of geometry changes on the nodal force rate. This matrix is termed the distortion rate matrix (Burd (1986)).

The distortion rate matrix is given by:-

$$[C]\,\underset{\sim}{U} = [\dot{B}]^T\,\underset{\sim}{\sigma}\,r\,J\,T + [B]^T\,\underset{\sim}{\sigma}\,\dot{r}\,J\,T + [B]^T\,\underset{\sim}{\sigma}\,r\,\dot{J}\,T + [B]^T\,\underset{\sim}{\sigma}\,r\,J\,\dot{T} \tag{4.24}$$

The four terms in the distortion rate matrix each represent specific components of the nodal force rate equation. The first term gives the rate of change of element geometry and the three remaining terms account for the rate of change of the radius (r), the Jacobian (J) and the thickness (T). It is not possible to find $[C]$ directly by matrix manipulation, instead it is considered in two parts and rewritten as:-

$$[C]\,\underset{\sim}{U} = [C_1]\,\underset{\sim}{U}\,r\,J\,T + [B]^T\,\underset{\sim}{\sigma}\,r\,J\,T\left(\frac{\dot{r}}{r} + \frac{\dot{J}}{J} + \frac{\dot{T}}{T}\right) \tag{4.25}$$

where:-

$$[C_1]\,\underset{\sim}{U} = [\dot{B}]^T\,\underset{\sim}{\sigma} \tag{4.26}$$

The first term of equation (4.25) is evaluated by expanding it on a term-by-term basis and the second term is obtained by matrix manipulation. The resulting $[C_1]$ matrix for the specific case of a five-noded axisymmetric membrane element is defined in Appendix 4A. The substitution procedure used in equation (4.26) was initially developed by Burd (1986) for the plane strain continuum element formulation. It is noteworthy that for the plane strain membrane element, however, this matrix solving was avoided by algebraic manipulation of the matrix equations, as discussed in Section 4.3.

Since the stresses normal to the membrane are neglected, the proportional thickness change of the membrane can be written in terms of the tangential and circumferential strain rates:-

$$\frac{\dot{T}}{T} = -\frac{\nu}{1-\nu}(\dot{\varepsilon}_t + \dot{\varepsilon}_\theta) \tag{4.27}$$

The distortion rate matrix, equation (4.25), may therefore be rewritten using equations (4.12), (4.13), (4.14) and (4.27) to give:-

$$[C] = \left\{[C_1] + [B]^T \underset{\sim}{\sigma}\left(\frac{k\,[N]}{r} + \frac{R\,[N']^T[N']}{J^2} - \frac{\nu}{1-\nu}\left(\frac{R^T[N']^T[N']}{J^2} + \frac{k\,[N]}{r}\right)\right)\right\} r\,J\,T \tag{4.28}$$

All of the reinforced axisymmetric computations described in this thesis were carried out using a five-noded axisymmetric membrane element, which is compatible with the fifteen-noded axisymmetric continuum element, i.e. the same order of polynomial is used for the displacement interpolation. Additionally, a seven-point Gaussian quadrature scheme was used to evaluate the incremental stiffness matrix $[K]$ of equation (4.22). To obtain an exact integration the required number of Gauss points is actually determined by the degree of the polynomial to be evaluated. In general, a polynomial of degree $2n-1$ is integrated exactly by an n-point Gauss quadrature.

The polynomial order of $[K]$ can actually be determined from the nodal force vector equation (4.19), since it is by simply differentiating this expression with respect to time that the incremental stiffness matrix is obtained. In a small displacement problem the membrane element does not undergo any severe distortions and, assuming it is initially set up straight and that the nodes are equally spaced, the Jacobian of the transformation from global to reference co-ordinates, J, is a constant. Similarly, the global co-ordinates vector of any arbitrary point in the element, r', is also a constant. Consequently, the integrand in equation

(4.19) can be shown from Appendix 4A to be a polynomial of the tenth degree. Therefore, a six-point Gauss quadrature would be sufficient to integrate $[K]$ exactly for the small displacement problem.

However, once the element becomes distorted due to large displacements the determinant of the Jacobian, J, no longer remains a constant and the integrand of equation (4.22) becomes a ratio of polynomials, which corresponds to a polynomial of infinite degree. Therefore a seven-point Gaussian integration rule has been employed to evaluate the element stiffness matrix, since the use of any higher order routines will make very little difference.

4.2.3 Constitutive Equations

The axisymmetric membrane is modelled as a linear elastic isotropic material with a single value of Young's modulus, E, a Poisson's ratio, ν, and zero bending stiffness, since geosynthetics generally cannot sustain any significantly large compressions without buckling. In practice many different geosynthetic reinforcement materials are available, some of which are isotropic, for example spunbonded polypropylene geotextiles, while others are anisotropic, like the geogrids which possess different stiffnesses in the transverse and longitudinal directions. Although this axisymmetric membrane element is developed for the case of isotropy, an anisotropic membrane could be developed by modifying the material stiffness matrix appropriately.

Since the membrane has zero bending stiffness each of the tangential and circumferential stresses can independently be zero, i.e. buckle. In order to include these features in the formulation the following procedures are adopted for the four possible cases of constitutive behaviour.

Case (1): $\sigma_t > 0$ and $\sigma_\theta > 0$

From Hooke's Laws, assuming isotropic Young's modulus:-

$$\dot{\varepsilon}_t = \frac{\dot{\sigma}_t}{E} - \nu\frac{\dot{\sigma}_\theta}{E} \tag{4.29}$$

$$\dot{\varepsilon}_\theta = \frac{\dot{\sigma}_\theta}{E} - \nu\frac{\dot{\sigma}_t}{E} \tag{4.30}$$

These equations may be re-arranged in the form of equation (4.23), such that the material stiffness matrix may be shown to be:-

$$[D] = \begin{bmatrix} \dfrac{E}{1-\nu^2} & \dfrac{\nu E}{1-\nu^2} \\ \dfrac{\nu E}{1-\nu^2} & \dfrac{E}{1-\nu^2} \end{bmatrix} \tag{4.31}$$

Case (2): $\sigma_t > 0$ and $\sigma_\theta = 0$

In this case the membrane is buckled in the circumferential direction. The value of σ_θ is set to zero and so there is no coupling between $\dot{\varepsilon}_\theta$ and $\dot{\sigma}_t$. Equations (4.29) and (4.30) therefore become:-

$$\dot{\varepsilon}_t = \frac{\dot{\sigma}_t}{E} \tag{4.32}$$

$$\dot{\varepsilon}_\theta = 0 \tag{4.33}$$

Thus the material stiffness matrix is:-

$$[D] = \begin{bmatrix} E & 0 \\ 0 & 0 \end{bmatrix} \tag{4.34}$$

Case (3): $\sigma_t = 0$ and $\sigma_\theta > 0$

The membrane is buckled in the tangential direction and because there is no coupling between $\dot{\varepsilon}_t$ and $\dot{\sigma}_\theta$ equations (4.29) and (4.30) become:-

$$\dot{\varepsilon}_t = 0 \tag{4.35}$$

$$\dot{\varepsilon}_\theta = \frac{\dot{\sigma}_\theta}{E} \tag{4.36}$$

Thus the material stiffness matrix is:-

$$[D] = \begin{bmatrix} 0 & 0 \\ 0 & E \end{bmatrix} \tag{4.37}$$

Case (4): $\sigma_t = 0$ and $\sigma_\theta = 0$

The membrane is buckled in both the tangential and circumferential directions and therefore the material stiffness matrix becomes:-

$$[D] = \begin{bmatrix} 0 & 0 \\ 0 & 0 \end{bmatrix} \tag{4.38}$$

4.2.4 Stress Update Calculations

At the beginning of each load step of the analysis the global incremental element stiffness matrix $[K_G]$ is calculated and the stiffness equations are inverted to give the global incremental nodal velocities. The Gauss point tangential and circumferential strain increments are then calculated by integrating equations (4.13) and (4.14) exactly, over the finite time increment Δt (corresponding to the load increment), to give:-

$$\Delta\varepsilon_t = \log_e\left[\frac{J_{t+\Delta t}}{J_t}\right] \tag{4.39}$$

and:-

$$\Delta\varepsilon_\theta = \log_e\left[\frac{r_{t+\Delta t}}{r_t}\right] \tag{4.40}$$

where $\Delta\varepsilon_t$ and $\Delta\varepsilon_\theta$ are the respective finite tangential and circumferential Hencky strain increments at a point, over the time increment Δt. The value of the Jacobian at the beginning of the load step is J_t and at the end is $J_{t+\Delta t}$, while the radius of the point at the beginning of the load step is r_t and at the end is $r_{t+\Delta t}$.

For each increment of load the membrane thickness is determined by the expression:-

$$\log_e\left[\frac{T}{t_0}\right] = -\frac{\nu}{1-\nu}(\varepsilon_t + \varepsilon_\theta) \tag{4.41}$$

where T is the thickness at the end of the load step, t_0 is the original reinforcement thickness and ε_t and ε_θ are the updated tangential and circumferential Hencky strains respectively.

At the end of a load step the updated Gauss point stresses associated with the calculated total strains are determined so that a check on the general equilibrium of the system can be undertaken. The total stresses are not path dependent, which means that they may be calculated directly from the total strains using equations of the same form as the stress-strain rate equations in Section 4.2.3.

Firstly it is assumed that case (1) applies, i.e. that both the updated tangential and circumferential Hencky stresses, σ_t and σ_θ, are positive. Therefore equation (4.23) is used with $[D]$ given by equation (4.31):-

$$\sigma_t = \frac{E}{1-\nu^2}(\varepsilon_t + \nu\,\varepsilon_\theta) \tag{4.42}$$

$$\sigma_\theta = \frac{E}{1-\nu^2}(\varepsilon_\theta + \nu\,\varepsilon_t) \tag{4.43}$$

where ε_t and ε_θ are the updated tangential and circumferential Hencky strains calculated using equations (4.39) and (4.40).

However, if either or both of the Gauss point stresses are found to be negative, then that stress is set to zero and they are both re-calculated for the appropriate case (2, 3 or 4) using the relevant material stiffness matrix, as described in Section 4.2.3.

4.3 Plane Strain Membrane Element Formulation

The large strain finite element formulation of the one-dimensional plane strain isoparametric membrane element, already utilised in OXFEM, is fully described in both Burd (1986) and

Burd and Houlsby (1986). The finite element equations derived for this plane strain element will therefore be discussed only briefly in this section to highlight the essential differences between the plane strain and axisymmetric formulations.

In the plane strain analysis the strain in the direction perpendicular to the x-y plane is, by definition, zero. As in the axisymmetric case, the plane strain element is assumed to have no bending stiffness and therefore no shear stress component needs to be considered. The membrane is also assumed to be of no significant thickness, consequently the stresses normal to the membrane are negligible in comparison to the in-plane stresses. As a result, only the one component of longitudinal strain, ε_L , needs to be considered in the plane strain formulation.

The finite longitudinal Hencky strain increment, $\Delta\varepsilon_L$, at any particular point in the element, is found by a similar procedure to that described for the tangential Hencky strain increment within the axisymmetric membrane formulation, (see the derivation of equation (4.39)).

In calculating the plane strain nodal force rate vector $\dot{P}$, the incremental stiffness matrix $[K]$, can be algebraically manipulated into a convenient expression which is cast in the familiar form of the small displacement finite element equations, i.e.:-

$$[K] \;=\; \int_E [B]^{*T}\; [D]^*\; [B]^* \quad dV \tag{4.44}$$

where $[D]^*$ is a modified material stiffness matrix:-

$$[D]^* \;=\; \begin{bmatrix} E^* & 0 \\ 0 & \sigma_L \end{bmatrix} \tag{4.45}$$

which contains the variable:-

$$E^* \;=\; \frac{E}{1-\nu^2} \;-\; \frac{\sigma_L\,\nu}{1-\nu} \tag{4.46}$$

such that E is the Young's modulus of the membrane material, ν is the Poisson's ratio and σ_L is the longitudinal stress.

Furthermore, the modified matrix $[B]^*$ in equation (4.44) is of the form:-

$$[B]^* = \frac{1}{J^2}\begin{bmatrix} \underset{\sim}{X}^T [N']^T [N'] \\ \underset{\sim}{X}^T [N']^T [Z]^T [N'] \end{bmatrix} \tag{4.47}$$

where:-

$$[Z] = \begin{bmatrix} 0 & -1 \\ 1 & 0 \end{bmatrix} \tag{4.48}$$

and $\underset{\sim}{X}$ is the vector of global nodal co-ordinates, $[N]$ is the shape function matrix and J is the Jacobian of the transformation from global to reference co-ordinates.

The plane strain incremental stiffness formulation, equation (4.44), is clearly of a much simpler configuration than that of the axisymmetric formulation, equation (4.22). This has the advantage of making the plane strain finite element implementation relatively easy in comparison to the more complicated axisymmetric formulation. Moreover, having $[K]$ in the small displacement form means that this large displacement plane strain formulation can be incorporated into existing finite element codes with the minimum of software modification.

An important feature of the plane strain incremental stiffness matrix is the (2 x 1) configuration of the modified matrix $[B]^*$. This matrix relates the nodal velocity vector $\underset{\sim}{U}$ to the strain rate vector $\dot{\underset{\sim}{\varepsilon}}$, as shown in the axisymmetric equation (4.15). When considering the axisymmetric problem there are clearly two terms within the strain rate vector, those of the tangential and circumferential strain rates, $\dot{\varepsilon}_t$ and $\dot{\varepsilon}_\theta$, whereas for plane strain the two terms of the strain rate vector are not, initially, as obvious. The first term is

in fact the longitudinal strain rate $\dot{\varepsilon}_L$, while the second term is actually identified with the anti-clockwise rotation rate of the element. Therefore, the plane strain nodal force rate vector, $\dot{\underset{\sim}{P}}$, can be associated with both longitudinal straining and element rotation.

It is also useful to consider the significance of the stress rate vector $\dot{\underset{\sim}{\sigma}}$, which is given by the product of the plane strain modified material stiffness matrix $[D]^*$ and the strain rate vector $\dot{\underset{\sim}{\varepsilon}}$, as shown in the axisymmetric equation (4.23). Clearly there are also two terms within the plane strain stress rate vector. The first term is the longitudinal stress rate $\dot{\sigma}_L$, while the second stress rate term is associated with the element rotation rate.

Within the plane strain formulation an allowance is made for changes in the cross-sectional area of the membrane, A, as the analysis progresses, similar to the axisymmetric formulation where account is made of the varying membrane thickness. It is necessary to calculate the cross-sectional area of the membrane, at the relevant Gauss point, in order to fully evaluate the plane strain incremental stiffness matrix $[K]$, equation (4.44). For each increment of load the cross-sectional area is determined by the expression:-

$$\log_e \left[\frac{A}{A_0} \right] = -\frac{\nu}{1-\nu} \Delta\varepsilon_L \tag{4.49}$$

where A_0 is the area at the start of the calculation step, A is the area at the end of the step and $\Delta\varepsilon_L$ is the longitudinal Hencky strain increment.

All of the large displacement reinforced plane strain computations described in this thesis were carried out using a three-noded membrane element, with a three-point Gaussian integration rule. It is worthy of note that a two-point Gaussian integration rule would in fact be sufficient for the small displacement case, provided that the Jacobian did not vary along the element. The finite element equations for the specific case of the three-noded element are fully detailed in Burd (1986) and therefore require no repetition here.

4.4 Verification of the Axisymmetric Membrane Formulation

To validate the new axisymmetric membrane formulation and the corresponding computer code, several different test analyses are undertaken. The principal objective in conducting these relatively simple, but rigorous, tests is to verify that the membrane is modelled accurately before attempting the more complex problem of the reinforced two-layer soil system.

The test problems are designed to investigate the small and large displacement behaviour of the elastic membrane, since both these modes of deformation are fundamentally important within a reinforced two-layer soil system, for displacement and force controlled calculations. The membrane elements are also arranged in different configurations.

4.4.1 Small Strain Thick-walled Cylinder Analysis

To ensure that the finite element formulation predicts the tangential and circumferential stresses accurately, a relatively simple small strain elastic test is conducted. This problem is analogous to a small strain thick-walled cylinder of inner radius $a = 1\ m$ and outer radius $b = 5\ m$, subjected to an external tensile stress P^*. The mesh used for the calculation consists of two five-noded axisymmetric membrane elements, as shown in Figure 4.4.

The material is allocated a relatively high value of Young's modulus, $E = 10^6\ kPa$, to ensure a small displacement response, the Poisson's ratio is taken as zero and the membrane thickness is set to unity. The expansion of the cylinder is carried out as a displacement controlled analysis.

The resulting tangential and circumferential stresses at each of the Gauss point co-ordinates r are plotted in Figure 4.4, normalised by the external stress P^*. The well known elasticity solutions (e.g. Benham and Crawford (1987)) are also shown for comparison. It is found that the finite element results closely approximate the exact solution for the small strain elastic case.

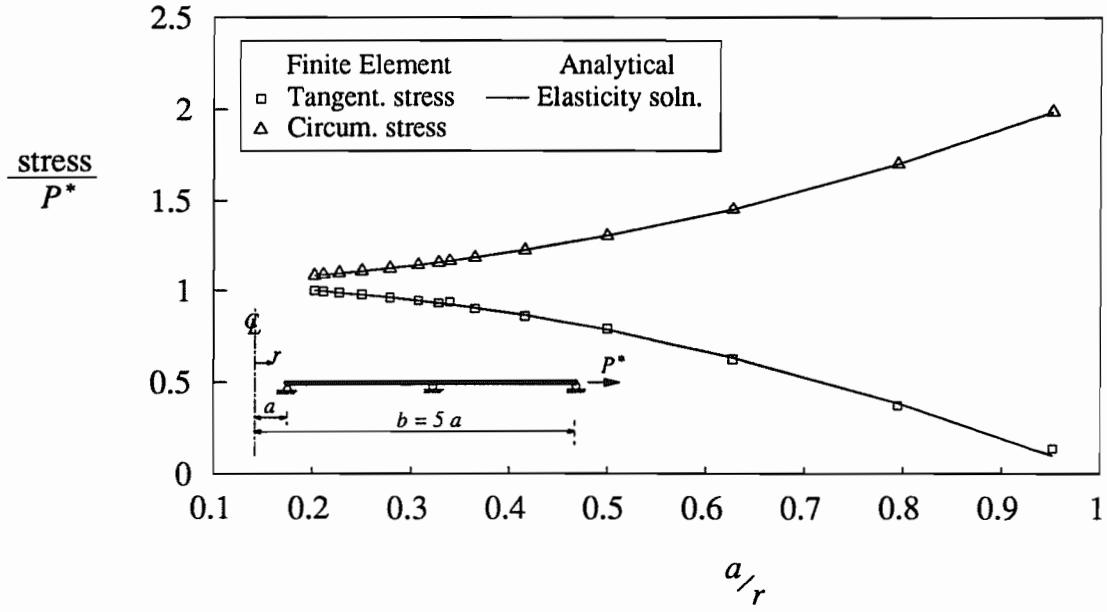

Figure 4.4: Stresses in a Thick-walled Cylinder

4.4.2 Large Strain Cavity Expansion Analysis

This test problem is essentially a large displacement one-dimensional cavity expansion analysis. An exact closed form solution for this problem has been established by Sagaseta (1984), based on elastic perfectly-plastic large strain theory. The axisymmetric membrane element, however, has been defined as an elastic material and consequently this analytical solution needs to be modified to negate the plasticity part of the calculation.

Clearly a cavity expansion analysis requires the material to sustain compressive stresses, which the membrane material is specifically not allowed to do. However, the stress update calculations as described in Sections 4.2.3 and 4.2.4 can be modified to allow compression, so that the induced negative strains and stresses are not set to zero and where case (1) only of the constitutive behaviour applies. The value in undertaking this analysis is that the large displacement nature of the membrane element can be compared to a known solution. In all other uses of the axisymmetric membrane element in this thesis the original constitutive behaviour and stress updating apply.

The Sagaseta (1984) solution relates specifically to an incompressible material, i.e. one with a Poisson's ratio of 0.5 , but to avoid numerical instability the finite element

calculations must use the approximation of $\nu = 0.49$ for the membrane material. The analytical theory also assumes the continuum is of infinite extent. However, Burd and Houlsby (1990) show how this can in fact be simulated in a finite element analysis through using a "correcting layer" at the periphery of the mesh. By incorporating an additional element layer, with appropriately different material properties, it is possible to model an infinite medium while using a finite mesh size. This is achieved by adding a layer of elements, with a rigidly fixed edge of outer radius b to the mesh of initial outer radius c, provided that the following relationship is satisfied:-

$$\frac{G^*}{G} = \frac{\left(\left(\frac{b}{c}\right)^2 - 1\right)(1 - 2\nu^*)}{\left(1 + \left(\frac{b}{c}\right)^2 (1 - 2\nu^*)\right)} \tag{4.50}$$

where G is the shear modulus of the medium to be modelled and G^* and ν^* are the shear modulus and Poisson's ratio of the correcting layer.

The one-dimensional mesh, of initial thickness $t_0 = 0.0001$, used for the finite element calculation is shown in Figure 4.5. The elastic membrane is assumed to have a shear modulus of $100\ kPa$ and the correcting layer, of radius twice that of the original mesh radius, is prescribed the properties of $G^* = 50\ kPa$ and $\nu^* = 0.25$. The initial cavity radius a_0 is expanded to a final cavity radius of $a = 5\ a_0$, using a displacement controlled analysis.

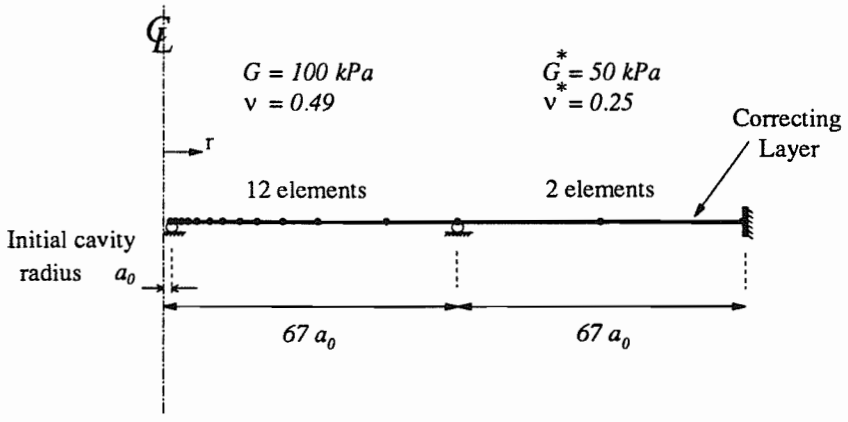

Figure 4.5: Finite Element Mesh for Cavity Expansion

Figure 4.6 shows the tangential and circumferential stresses calculated by the finite element analysis, compared to the Sagaseta (1984) analytical solution. The stresses are normalised by the shear modulus G, a is the final cavity radius and r is the radius corresponding to the position of the Gauss point stresses.

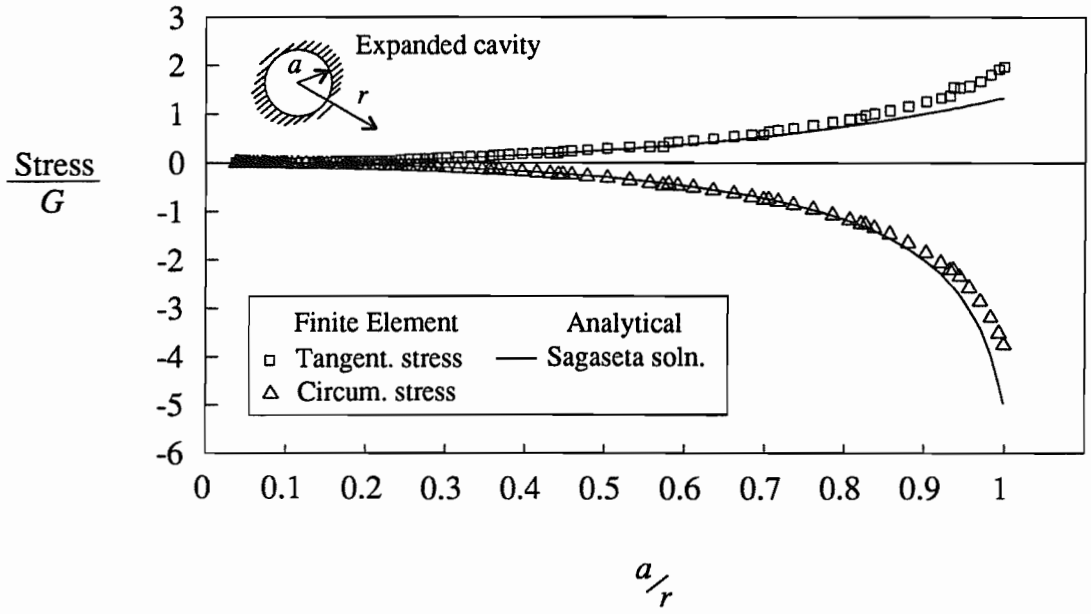

Figure 4.6: Stresses for Cavity Expansion Analysis

The finite element predictions using 100 load steps generally agree well with the analytical solution. Some deviation of the results occurs at the inner boundary ($a/r = 1$) due to discretization errors. It was found that the results are very sensitive to the number of load steps used, causing increased divergence of the stresses from the Sagaseta (1984) solution for too many or too few steps.

4.4.3 Thin-walled Cylinder Expansion Analysis

A 2 m tall thin-walled cylinder of inner radius R = 1 m is modelled by two vertical axisymmetric membrane elements as shown in Figure 4.7. The cylinder wall, of initial thickness $t_0 = 0.001$ m, is assigned a Young's modulus of $E = 2 \times 10^8$ kPa and a Poisson's ratio $\nu = 0.3$.

Keeping the tangential strain zero and neglecting any radial stress in the cylinder wall, it can be shown that for a uniform radial wall displacement of u_r the circumferential, σ_θ, and meridional, σ_t, stresses in the cylinder are given by:-

$$\sigma_\theta = \frac{E}{(1-\nu^2)} \ln\left(\frac{R+u_r}{R}\right) \tag{4.51}$$

$$\sigma_t = \nu\,\sigma_\theta \tag{4.52}$$

where the meridional stress is identical to the tangential stress in the membrane.

The computed large displacement finite element membrane stresses and the corresponding exact elastic solutions, shown in Figure 4.7 for different radial wall displacements, are very comparable.

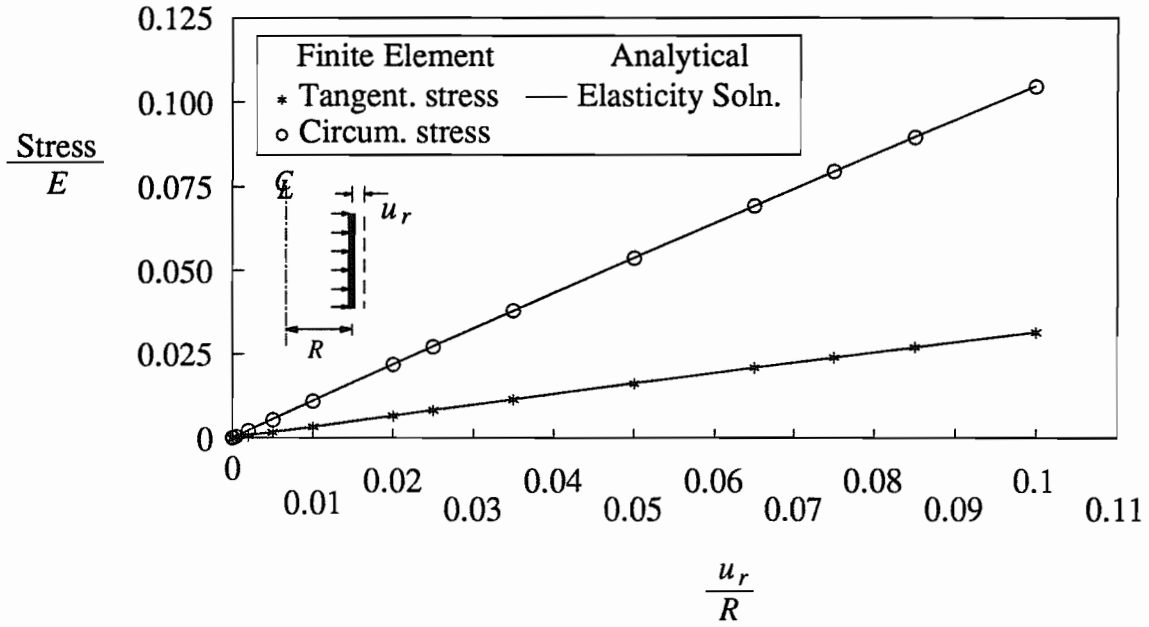

Figure 4.7: Expansion of a Thin-walled Cylinder

4.4.4 Annular Plate with Fixed Periphery and Inward Pressure

A horizontal simply-supported annular plate of initial thickness $t_0 = 0.0005\ m$, rigidly fixed at the outer radius of $b = 5\ m$ with an inward acting pressure of P at the inner radius $a = 1\ m$, is used to study the case when one stress falls to zero.

The plate is assigned a Young's modulus of $E = 2\text{x}10^8\ kPa$ and a Poisson's ratio of $\nu = 0.3$. For a linear elastic material the tangential, or in this case the radial stress, σ_t, will be tensile throughout the plate, but the circumferential stress, σ_θ, will be tensile only within a small area at the outside edge and tends to be compressive towards the centre. The membrane material does not allow compressive stresses, so the elastic solution to this problem is found by considering two separate zones in the plate and maintaining compatibility of the stresses at the boundary.

For the unbuckled outer zone the equations of equilibrium, compatibility of strain and displacements, and the stress-strain relationships of elasticity combine to give:-

$$\sigma_t = A - \frac{B}{r^2} \qquad \sigma_\theta = A + \frac{B}{r^2} \tag{4.53}$$

where A and B are constants. Whereas, for the circumferentially buckled inner zone, the stresses are calculated by equilibrium only and are of the form:-

$$\sigma_t = \frac{D}{r} \qquad \sigma_\theta = 0 \tag{4.54}$$

where D is a constant.

The boundary conditions of the problem, where c is the radius of the limit of the circumferential buckling as shown in Figure 4.8, are: at $r = a$, $\sigma_t = P$; at $r = c$, $\sigma_\theta = 0$ and σ_t is continuous; and at $r = b$, $\varepsilon_\theta = 0$. By applying these boundary conditions and maintaining compatibility of the stresses at $r = c$, it may be shown that:-

$$c = \frac{b\,(1-\nu)^{\frac{1}{2}}}{(1+\nu)^{\frac{1}{2}}} \tag{4.55}$$

and that in the unbuckled outer zone the tangential and circumferential stresses are:-

$$\sigma_t = \frac{P\,a}{2\,b\,(1-\nu^2)^{\frac{1}{2}}}\left\{(1+\nu) + (1-\nu)\left(\frac{b}{r}\right)^2\right\} \tag{4.56}$$

$$\sigma_\theta = \frac{P\,a}{2\,b\,(1-\nu^2)^{\frac{1}{2}}}\left\{(1+\nu) - (1-\nu)\left(\frac{b}{r}\right)^2\right\} \tag{4.57}$$

and in the buckled inner zone:-

$$\sigma_t = \frac{P\,a}{r} \qquad \sigma_\theta = 0 \tag{4.58}$$

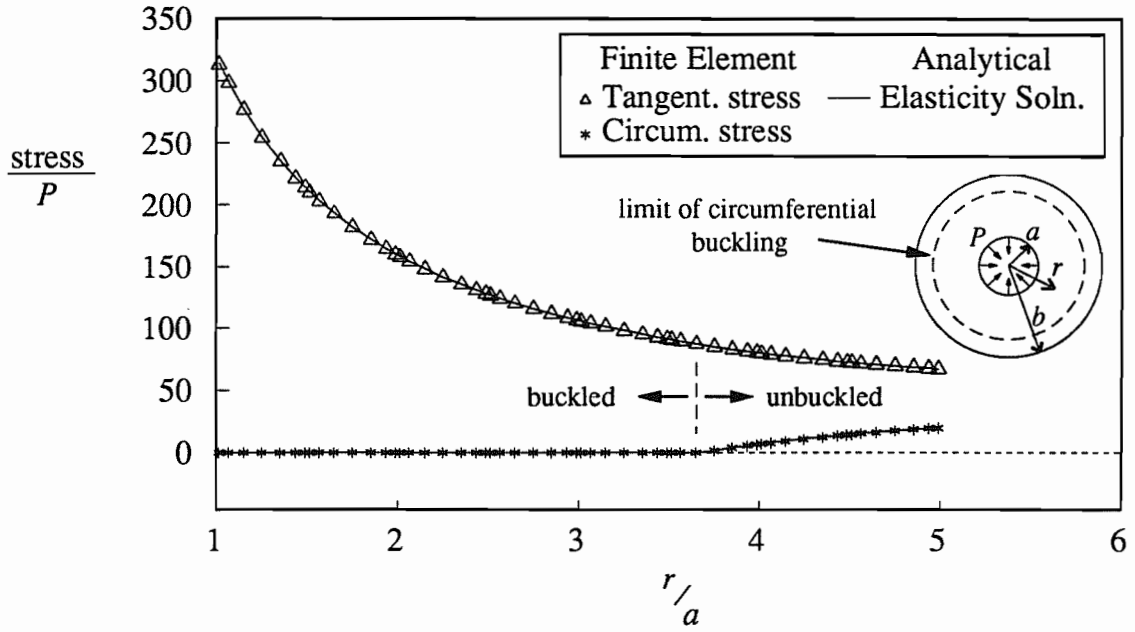

Figure 4.8: Annular Plate with Fixed Periphery and Internal Inward Pressure

The close correlation between the large strain finite element results, using a mesh of 8 axisymmetric membrane elements, and the elasticity solution is illustrated in Figure 4.8.

4.4.5 Annular Plate with Fixed Periphery and Vertical Displacements

To check that the incremental stiffness matrix, $[K]$, is correctly formulated in the finite element equations, this test problem compares the nodal forces computed by two separate methods.

A single axisymmetric membrane element is used to model an annular plate of internal radius $a = 1.0\,m$ and external radius $b = 5\,a$, with the outer edge fixed. The plate is assigned

the properties of a Young's modulus $E = 10^3\ kPa$, Poisson's ratio of zero and an initial thickness of unity. Vertical displacements, δ_v, are prescribed to each of the inner four nodes leaving the fifth node fixed, so that the element slopes down towards the centre-line, but remains straight with equal distances between the nodes in the tangential direction, as shown in Figure 4.9. For a particular set of nodal displacements, $\underset{\sim}{U}$, the resulting vector of nodal forces, $\underset{\sim}{P}$, in equilibrium with the Gauss point stresses, $\underset{\sim}{\sigma}$, is calculated exactly by the equation (4.59):-

$$\underset{\sim}{P} = \int_E [B]^T \underset{\sim}{\sigma}\ dV \tag{4.59}$$

which is derived from equation (4.17) and where the $[B]$ matrix is defined in Appendix 4A.

These nodal forces can also be calculated incrementally by the equation (4.60):-

$$\Delta\underset{\sim}{P} = [K]\,\Delta\underset{\sim}{U} \tag{4.60}$$

where $[K]$ is determined by equation (4.22) and the final horizontal and vertical nodal forces, F_x and F_y, are given by summing the incremental nodal forces over a finite number of steps. By increasing the number of steps the results of equation (4.60) approximate more closely to those of equation (4.59).

A comparison of the computed nodal forces, using 10,000 steps for equation (4.60), is shown in Figure 4.9. There is an average error of less than 0.5%, as opposed to $\approx 3\%$ for 1,000 steps.

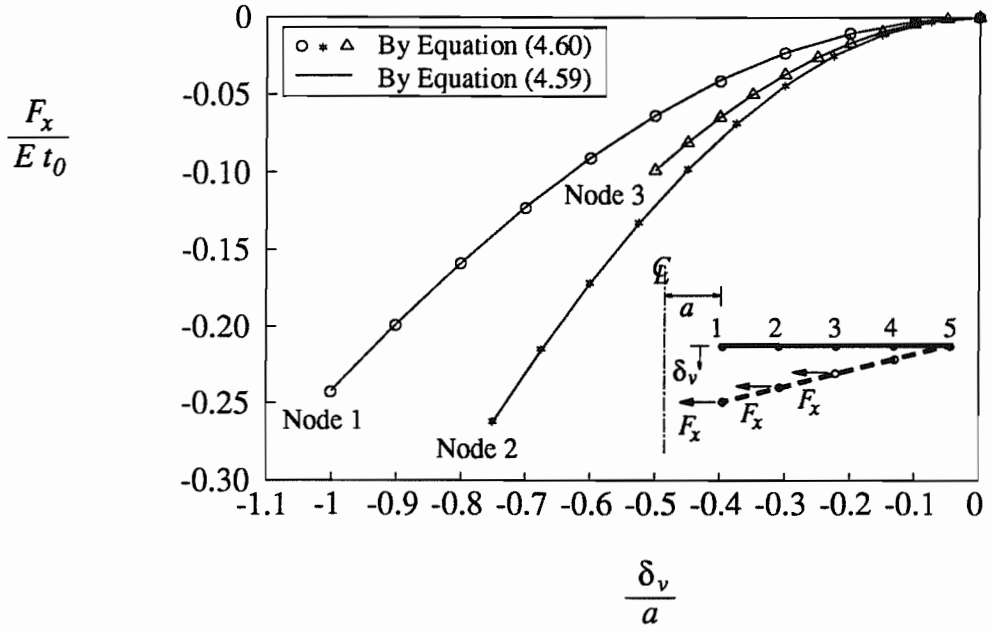

a) Horizontal Nodal Forces

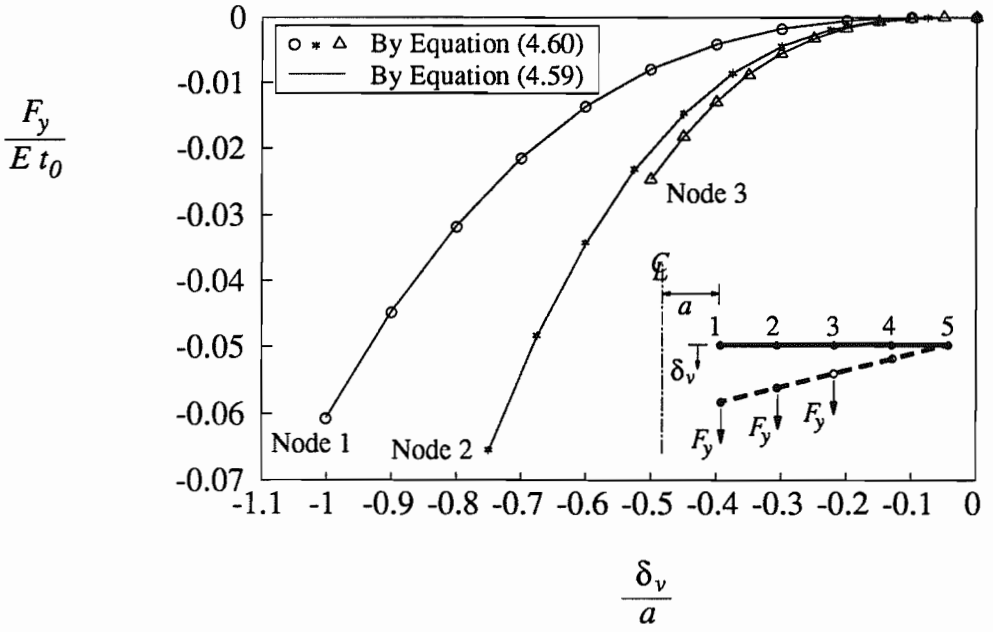

b) Vertical Nodal Forces

Figure 4.9: Nodal Forces for varying Vertical Nodal Displacements

4.4.6 Expanding Sphere Analysis

By modelling the displacement controlled expansion of a thin-walled sphere, of initial radius $R = 1.0\,m$ and thickness $t_0 = 0.001\,m$, the membrane elements are tested for a variety of geometric configurations.

Six axisymmetric membrane elements are orientated in a semi-circle about a centre-line, as shown in Figure 4.10, with horizontal fixities at the top and bottom. Each node is prescribed the same outward radial displacement, u_r, corresponding to a uniform inflating pressure, so that the resulting meridional (tangential) and circumferential membrane stresses, σ_t and σ_θ, are identical.

By elasticity theory it may be shown that these stresses are given by:-

$$\sigma_t = \sigma_\theta = \frac{E}{(1-\nu)} \ln\left(\frac{R+u_r}{R}\right) \tag{4.61}$$

where $E = 2\text{x}10^5\ kPa$ and ν are the Young's modulus and Poisson's ratio of the material, respectively.

The membrane stresses at different radial displacements, predicted by the large displacement finite element analysis, are compared in Figure 4.10 to the elasticity solutions for two different values of Poisson's ratio. The analyses were conducted using displacement control, since force control proved too unstable.

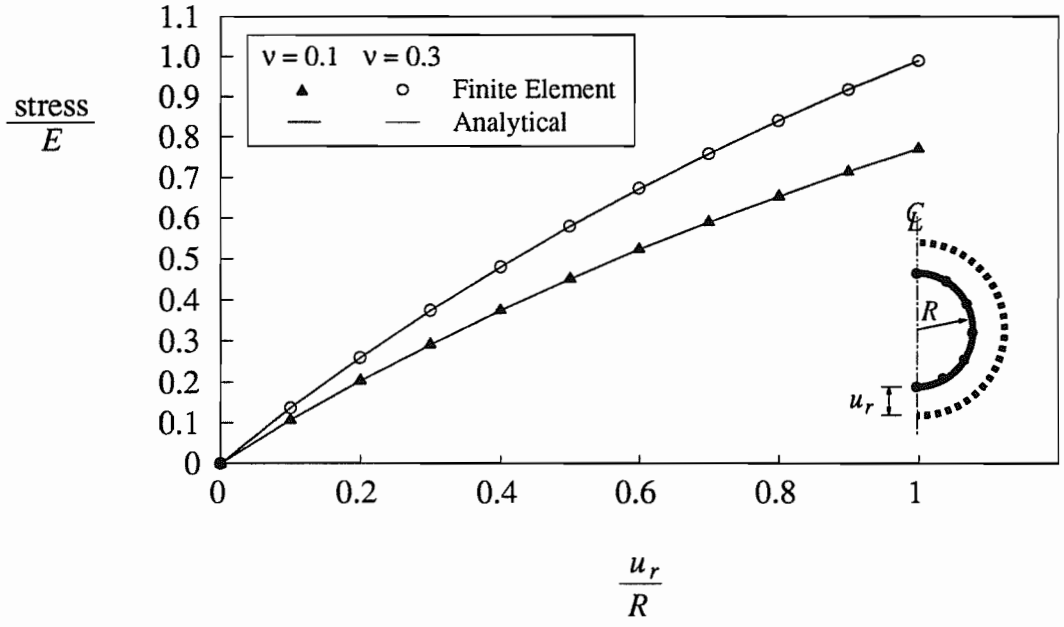

Figure 4.10: Membrane Stresses in Expanding Sphere

APPENDIX 4A

Finite Element Equations for the Five-Noded Membrane Element

Figure 4.11 shows the isoparametric mapping between the parent and reference elements for the five-noded membrane element.

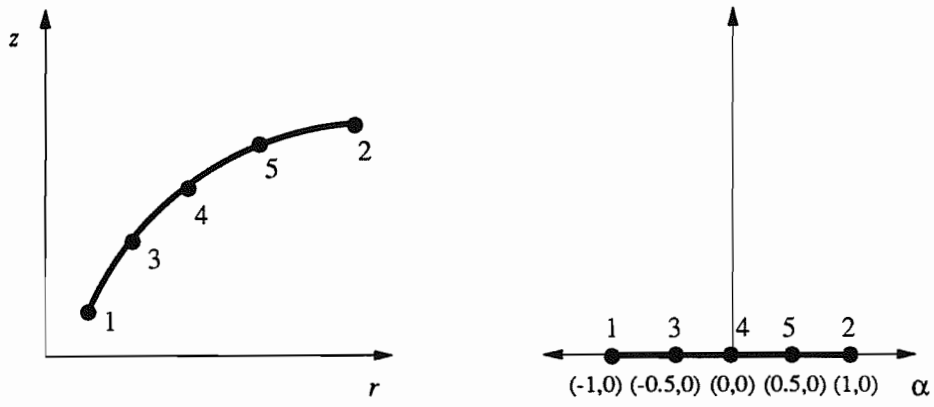

Parent Element **Mapped Element**

Figure 4.11: Mapping for the Five-Noded Axisymmetric Membrane Element

The vectors $\underset{\sim}{r}$ and $\underset{\sim}{R}$, that are related by equation (4.4), are defined as:-

$$\underset{\sim}{r}^T = [\, r \quad z \,] \tag{4.62}$$

$$\underset{\sim}{R}^T = [\, R_1 \quad Z_1 \quad R_2 \quad Z_2 \quad \ldots \quad R_5 \quad Z_5 \,] \tag{4.63}$$

Where R_i, Z_i are the global co-ordinates of the i^{th} node. The shape function matrix is:-

$$[N] = \begin{bmatrix} f_1 & 0 & f_2 & 0 & f_3 & 0 & f_4 & 0 & f_5 & 0 \\ 0 & f_1 & 0 & f_2 & 0 & f_3 & 0 & f_4 & 0 & f_5 \end{bmatrix} \tag{4.64}$$

in which:-

$$f_1 = \frac{2}{3}(\alpha+1/2)\,(\alpha)\,(\alpha-1/2)\,(\alpha-1) \tag{4.65}$$

$$f_2 = \frac{2}{3}(\alpha+1/2)\,(\alpha)\,(\alpha-1/2)\,(\alpha+1) \tag{4.66}$$

$$f_3 = -\frac{8}{3}(\alpha+1)(\alpha)(\alpha-1/2)(\alpha-1) \tag{4.67}$$

$$f_4 = 4(\alpha+1)(\alpha-1)(\alpha+1/2)(\alpha-1/2) \tag{4.68}$$

$$f_5 = -\frac{8}{3}(\alpha+1)(\alpha)(\alpha+1/2)(\alpha-1) \tag{4.69}$$

The $[B]$ matrix of equation (4.15) is given by:-

$$[B] = \begin{bmatrix} \frac{f_1' r'}{J^2} & \frac{f_1' z'}{J^2} & \frac{f_2' r'}{J^2} & \frac{f_2' z'}{J^2} & \cdots & \frac{f_5' r'}{J^2} & \frac{f_5' z'}{J^2} \\ \frac{f_1}{r} & 0 & \frac{f_2}{r} & 0 & \cdots & \frac{f_5}{r} & 0 \end{bmatrix} \tag{4.70}$$

The $[C_1]$ matrix of equation (4.26) maybe shown to be:-

$$[C_1] = \begin{bmatrix} C_{1,1} & C_{1,2} & \cdots & C_{1,10} \\ C_{2,1} & C_{2,2} & \cdots & C_{2,10} \\ & & & \\ C_{10,1} & C_{10,2} & \cdots & C_{10,10} \end{bmatrix} \tag{4.71}$$

in which:-

$$C_{2i-1,2j-1} = \sigma_t f_i' f_j' \frac{A}{J^2} - \frac{\sigma_\theta f_i f_j}{r^2} \tag{4.72}$$

$$C_{2i,2j-1} = 2\sigma_t f_i' f_j' \frac{B}{J^2} \tag{4.73}$$

$$C_{2i-1,2j} = 2\sigma_t f_i' f_j' \frac{B}{J^2} \tag{4.74}$$

$$C_{2i,2j} = -\sigma_t f_i' f_j' \frac{A}{J^2} \tag{4.75}$$

where

$$A = \frac{1}{J^2}\left(\left(\frac{dz}{d\alpha}\right)^2 - \left(\frac{dr}{d\alpha}\right)^2\right) \tag{4.76}$$

and

$$B = -\frac{1}{J^2}\left(\left(\frac{dz}{d\alpha}\right)\left(\frac{dr}{d\alpha}\right)\right) \tag{4.77}$$

CHAPTER 5:

ANALYSIS OF THE SOIL-REINFORCEMENT INTERFACE

5.1 Introduction

This chapter is concerned with the analysis of the soil-reinforcement interface for a two-layer soil system, using both standard continuum elements and a special class of finite element termed interface elements. In Section 5.2 a description is given of the methods that might be used to extract the interface stresses from a finite element solution for the case when no interface elements are used. A brief review of different types of interface elements currently available is given in Section 5.3 and the formulation of a new large strain, small relative displacement, axisymmetric interface element is described in Section 5.4.

To investigate fully the mechanisms of reinforcement within a two-layer soil system, which incorporates a geosynthetic membrane, the stresses acting at the interfaces of the different materials need to be calculated accurately. This requires an exact modelling of the soil-structure interaction.

In previous publications on finite element studies for reinforced two-layer soil systems using OXFEM, it was assumed that the reinforcement interlocked perfectly with the surrounding soil and that no slip occurred at the soil-reinforcement interfaces (e.g. Burd (1986), Burd and Houlsby (1989) and Burd and Brocklehurst (1990)). However, this assumption was shown by the experimental work of Fannin (1986) to be justified only for the area directly under the footing (see Section 2.3). Outside of this region it was found that the interlock between the granular material and the grid reinforcement was partially lost due

to the upward heave movements of the deforming subgrade through the grid. It was also reported by Milligan *et al.* (1986) that when excavations were conducted of the full-scale plate loading tests performed on reinforced two-layer soil systems, little evidence was actually found of the geogrid interlocking with particles of fill. Therefore, to model numerically the soil-reinforcement interfaces more accurately it was felt necessary to include interface elements in OXFEM.

The use of interface elements has two distinct advantages. Firstly they allow the properties of the reinforcement-soil interface to be varied independently of the soil properties and secondly they provide a convenient way of extracting the stresses acting at the soil-reinforcement interface. All of the plane strain and axisymmetric finite element analyses, of two-layer soil systems, discussed in later chapters of this thesis have interface elements incorporated.

5.2 Determination of Interface Stresses from Continuum Elements

The key to understanding the mechanisms of reinforcement of a two-layer soil system is a clear knowledge of the shear stresses acting at the interface. It is important, therefore, to determine these stresses precisely.

Difficulties in accurately calculating and analysing the interface stresses at the continuum-membrane element boundaries were discussed in the finite element analyses reported in Burd (1986). The method that was used by Burd (1986) to determine these interface stresses, from the six-noded continuum elements and three-noded membrane elements, involved calculating them from the force associated with the mid-side node of the common edge. The forces at the element corners were ignored, as discussed later for Method 2. It was found that the shear stresses acting at the membrane surface, for both reinforced and unreinforced analyses, showed marked variations along the length of the interface, whereas the normal stresses were much better conditioned. These large spatial variations of shear stress were attributed by Burd (1986) to discretization errors involved in the numerical model and to the general tendency of the finite element method to produce

solutions which have local erroneous variations even though they are globally correct. It was felt, however, that an improved method of interface analysis was needed, especially since the shear stresses are of particular importance.

An investigation, as part of this dissertation, into the different ways of establishing the normal, σ, and shear, τ, stresses at an interface between continuum and membrane elements has led to the development of four separate methods of analysis. Figure 5.1 depicts a typical boundary between a six-noded, plane strain, continuum element containing three Gauss points (***A***, ***B*** and ***C***) and a three-noded membrane element of length L^m. The continuum-membrane element boundary is illustrated here for the case of small displacement (i.e. the nodal positions are not updated), with the reinforcement horizontal.

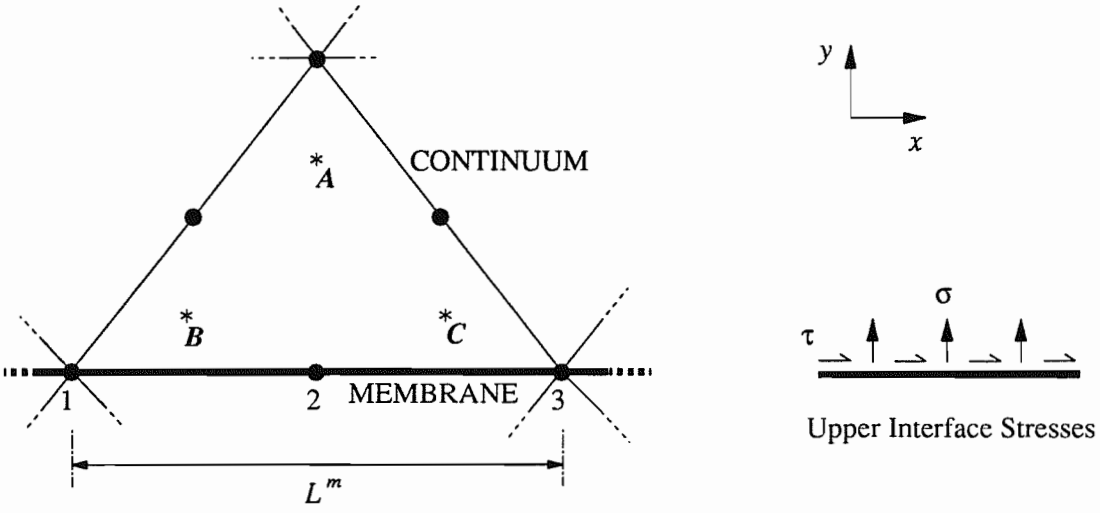

Figure 5.1: A Typical Continuum-Membrane Element Boundary (Without an Interface Element)

Method 1: The interface stresses are calculated from the contribution of the forces acting at all three of the nodes along the side of each six-noded continuum element directly adjacent to the membrane. The method assumes that 100% of the central nodal force and that 50% of the edge nodal forces contribute to the overall stress for that element. For the two continuum elements at the membrane ends, the full 100% of the edge nodal forces are taken into consideration (rather than 50%). Thus, the general boundary stresses are:-

$$\sigma = \frac{(F_{1y} + F_{3y})/2 + F_{2y}}{L^m} \tag{5.1}$$

$$\tau = \frac{(F_{1x} + F_{3x})/2 + F_{2x}}{L^m} \tag{5.2}$$

except for the left edge continuum-membrane elements, where the stresses are given by:-

$$\sigma = \frac{F_{1y} + (F_{3y})/2 + F_{2y}}{L^m} \tag{5.3}$$

$$\tau = \frac{F_{1x} + (F_{3x})/2 + F_{2x}}{L^m} \tag{5.4}$$

where F_{ix} and F_{iy} are the nodal forces at node i in the x and y directions respectively.

Method 2: Considers only the force at the mid-side node of the same continuum elements that are in contact with the membrane. It uses the equivalent nodal force loading ratios specific to a three-noded edge element, where a ratio of 2/3 of the total force applied to the element side acts at the mid-side node and 1/6 acts at each end node, therefore:-

$$\sigma = \frac{3\ F_{2y}}{2\ L^m} \tag{5.5}$$

$$\tau = \frac{3\ F_{2x}}{2\ L^m} \tag{5.6}$$

Method 3: This method considers a mean value for the three Gauss point stresses of the boundary continuum elements. Care must be taken for large strain, large displacement analyses to ensure that the normal and shear stresses obtained are actually perpendicular and parallel to the deformed membrane respectively, due to element rotation:-

$$\sigma = \{ (\sigma_y)_A + (\sigma_y)_B + (\sigma_y)_C \}/3 \tag{5.7}$$

$$\tau = \{ (\tau_{xy})_A + (\tau_{xy})_B + (\tau_{xy})_C \}/3 \tag{5.8}$$

where $(\sigma_y)_A$ is the value of the normal stress at Gauss point A and $(\tau_{xy})_A$ is the value of the shear stress at Gauss point A.

Method 4: This is similar to Method 3, but uses only the two Gauss points nearest the reinforcement in the continuum element concerned and it again requires the relevant stresses to be modified due to large strain element rotation:-

$$\sigma = \{ (\sigma_y)_B + (\sigma_y)_C \} / 2 \tag{5.9}$$

$$\tau = \{ (\tau_{xy})_B + (\tau_{xy})_C \} / 2 \tag{5.10}$$

For all of the methods discussed above the position at which the calculated stress acts is taken to be the average of the horizontal co-ordinates of the relevant nodes, or Gauss points considered. Typical graphs of the various normal and shear stresses, calculated at the upper and lower interfaces between continuum and membrane elements, are presented in Figures 5.3 and 5.4. These interface stresses are extracted from one small strain finite element calculation, using each of the four methods of analysis. In addition, the stresses obtained directly from an identical finite element calculation using interface elements are also illustrated. The stresses are normalised with respect to the plane strain undrained shear strength of the clay, s_u^{PS}, and the horizontal distance from the footing centre-line, x, is normalised with respect to the footing half-width, B.

The plane strain finite element mesh used for this soil-reinforcement interface study, shown in Figure 5.2, was developed by the mesh generator program OXMESH (Houlsby (1988)) and has overall dimensions of 5.0 m wide by 5.3 m deep with the reinforcement layer, separating the fill above from the clay below, at a depth of 0.3 m (shown as a double horizontal line). The mesh possesses 449 six-noded continuum elements and 20 three-noded membrane elements. The footing half width is $B = 0.25$ m and the material properties of the clay, fill and reinforcement are as given in Appendix 6A for the central parametric analysis. The interface properties for the one comparative analysis are also listed in Appendix 6A.

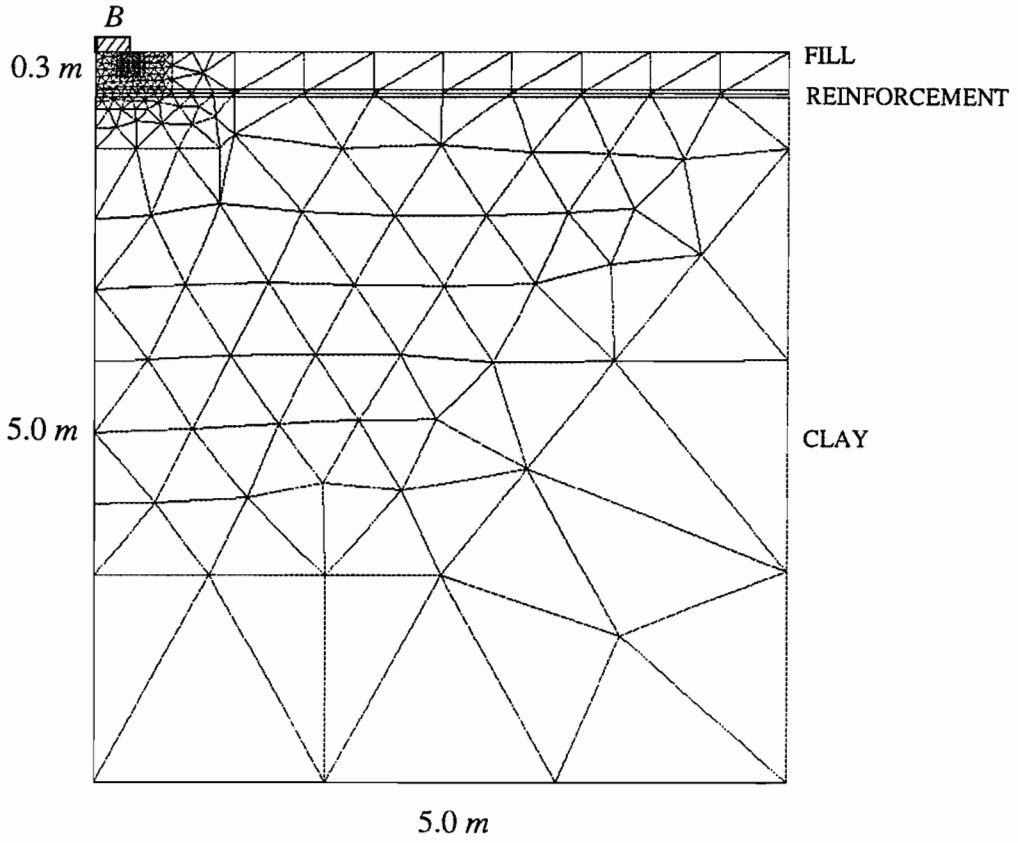

Figure 5.2: Plane Strain Finite Element Mesh B

The results of the study to investigate the four methods of interface analysis show that the normal stress profiles along the reinforcement length are all of a relatively comparable nature, Figure 5.3. Method 3, however, gave the most inconsistent result, in that the upper and lower interface normal stresses are not equal, whereas each of the other methods produced similar, reasonably smooth curves. The shear stress profiles, on the other hand, differed dramatically, Figure 5.4. Those obtained by using Methods 1 and 2 exhibited considerable oscillations and variations, especially for the lower shear stresses (which are thought to be spurious), whilst those from Methods 3 and 4 displayed a far smoother distribution. Method 1 gave the most disparate set of shear stresses of the four methods.

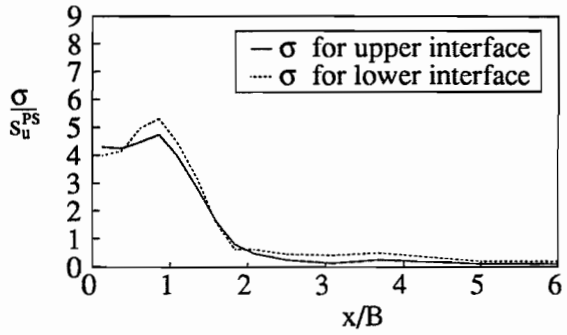

Method 1

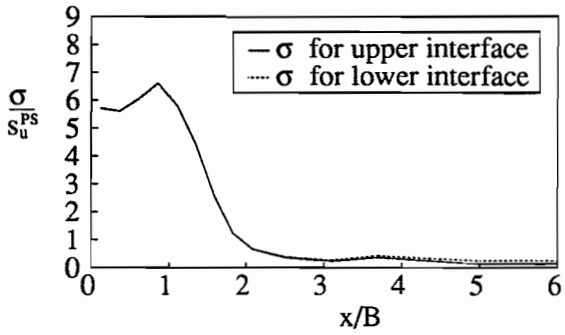

Method 2

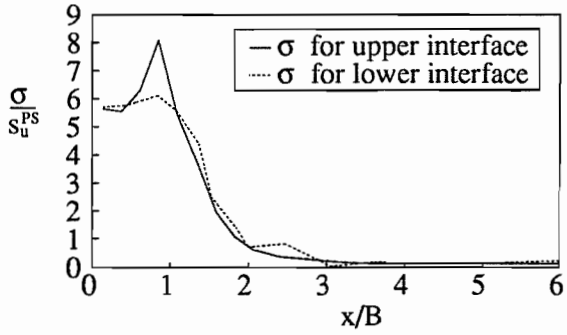

Method 3

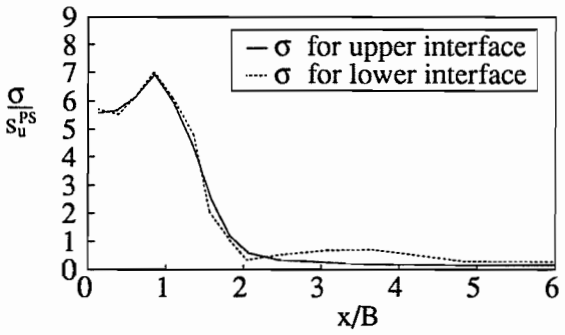

Method 4

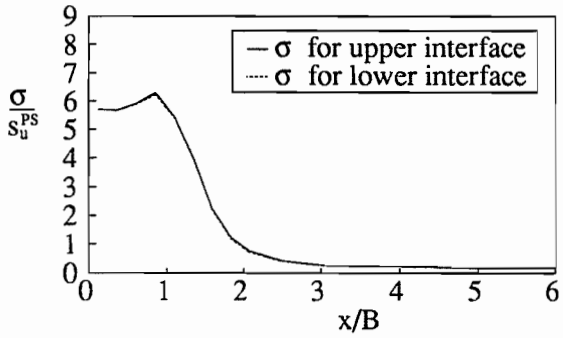

Interface Elements

Figure 5.3: Normal Stress Profiles along Interface for each Method of Analysis

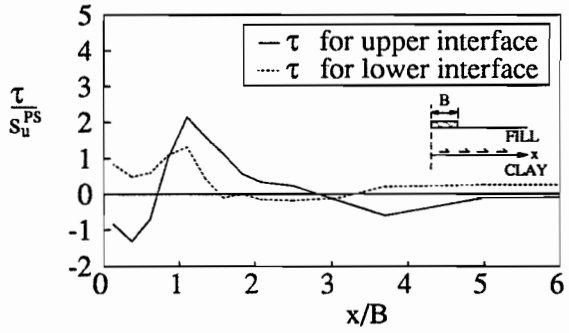

Method 1

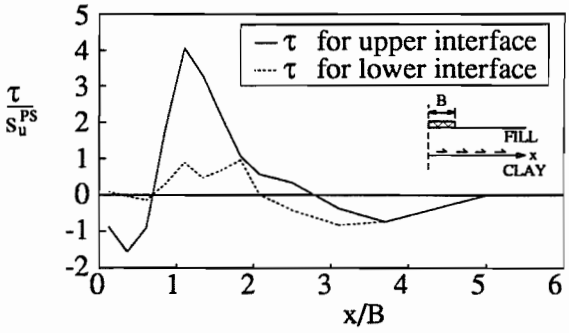

Method 2

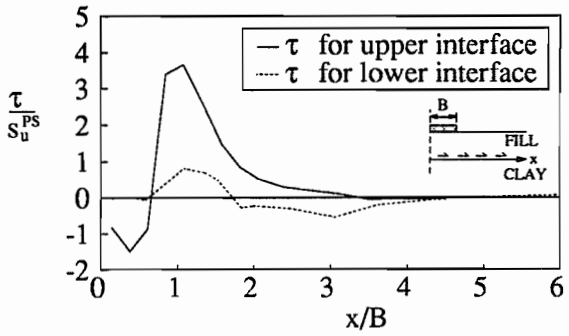

Method 3

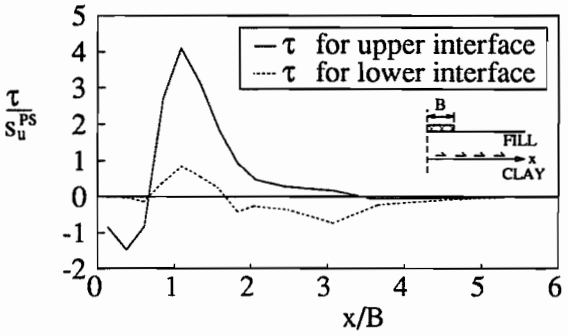

Method 4

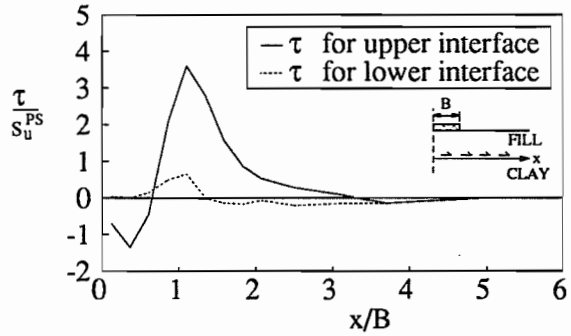

Interface Elements

Figure 5.4: Shear Stress Profiles along Interface for each Method of Analysis

It was concluded that the calculated normal stresses are approximately independent of the method, but that for the shear stresses the method based on the use of Gauss point stresses in adjacent elements gave results that were considered more satisfactory than those based on the use of nodal forces. Method 4 is thought to be the most appropriate of the four continuum element methods, since the calculated mean stresses in Method 3 will be slightly removed from the membrane, whereas in Method 4 the mean stresses are derived from the two Gauss points nearest the membrane. It is expected, however, that if a dense 'thin' band of continuum elements were placed above and below the reinforcement, across the entire width, then Method 3 may well be a more accurate analysis to use.

This study suggests that it is possible to extract interface stresses from the continuum elements. It was decided, however, to implement interface elements for each of the parametric study analyses (Chapters 6 - 10), since these provide a more straightforward approach to the extraction of interface stresses, this conclusion was also reached by Zeevaert (1980). A mean value of the Gauss point stresses can be obtained directly without concern for the large strain element rotations. Interestingly, the computed interface stresses at the end of a typical analysis using interface elements were found to be similar to those obtained by the best of the previous methods, i.e. Method 4, (see Figures 5.3 and 5.4). However, the use of interface elements is preferred on the basis that the stresses calculated are those precisely on the line of the interface, rather than those at a small distance from the reinforcement as generated by Method 4.

An investigative study into the modelling of interfaces using conventional eight-noded quadrilateral continuum elements was undertaken by Griffiths (1985). It was shown that satisfactory results for modelling both frictional and adhesive slippage at interfaces could be obtained, provided the thickness to length ratio of the elements remained smaller than 100. Slippage in the elements manifested itself by an increase in both the calculated shear displacements and the number of iterations necessary for numerical convergence. However, Griffiths (1985) further concluded that continuum elements at interfaces made good 'first approximations' in an analysis, but if large relative movement was a major factor, then specialised interface elements may prove necessary.

5.3 Types of Interface Elements

Conventional continuum elements have often proven inadequate in modelling soil-structure interaction exactly, especially where large relative lateral movement, or indeed separation occurs, e.g. Bell (1991) and Gens *et al.* (1989). However, the use of interface elements has been relatively successful in modelling such soil-structure interactions.

Interface elements have typically been applied to the problem of modelling jointed rock masses (Goodman *et al.* (1968)), or to the simulation of particular soil-structure interface behaviour, such as footings (Bell (1991)), soil reinforcement (Handel *et al.* (1990)) and piles (Zaman (1985)). The first proposal of a specific interface element formulation was made by Goodman *et al.* (1968) for the purely elastic case. Subsequently four main categories of finite elements have been proposed for the modelling of joints and interfaces, as detailed by Gens *et al.* (1989):-

1) Standard solid finite elements of small thickness, i.e. with an aspect ratio of < 100 (Griffiths (1985)).

2) Quasi-continuum elements possessing a weakness plane in the direction of the interface plane (Zienkiewicz *et al.* (1970)).

3) Linkage elements in which only the connections between opposite nodes are considered (Frank *et al.* (1982)).

4) Interface elements in which relative displacements between opposite nodes are the primary deformation variables and which use elastic, or elasto-plastic constitutive laws. This class combines the 'thin-layer element' of finite thickness (Zaman (1985)) and the 'zero-thickness element' (Goodman *et al.* (1968), Gens *et al.* (1989) and Burd and Brocklehurst (1991)).

An alternative procedure for modelling a soil-structure interface is presented by Moore and Booker (1989) and Kodikara and Moore (1991) for the particular problem of buried flexible pipes. They suggest using a nonlinear frictional-adhesive zero-tension interface model at the boundary between the two separate bodies, rather than employing a discrete interface element. The technique permits large rotations and substantial slip between the

interacting bodies, as well as the occurrence, or loss, of contact at the interface. However, large relative slip is not an important characteristic of the two-layer soil system and therefore this interface model would be superfluous

The zero-thickness interface element of category 4 has been used successfully within OXFEM for both the plane strain (Burd and Brocklehurst (1991)) and the three-dimensional (Bell (1991)) problem of modelling a distinct soil-structure interface. This type of element has therefore been incorporated into the finite element model described in Chapter 3. Details of the new axisymmetric interface element formulation, which is based on the same general procedures as those used for the plane strain interface element formulation described in Burd and Brocklehurst (1991), are presented in Section 5.4.

5.4 Axisymmetric Interface Element Formulation

The large strain finite element formulation of the new zero-thickness axisymmetric interface element is based on an isoparametric approach. The formulation takes account of the effects of large global displacements and rotations, but the relative displacements within the element are constrained to being infinitesimal. Although this is an apparent limitation to the general applicability of the element it is justified for the specific cases of the two-layer soil systems studied in this thesis, because in the important region immediately beneath the footing gross slip would not be expected to occur (as found experimentally by Fannin (1986) and numerically in Section 6.5).

The axisymmetric formulation described in this chapter is applicable to axisymmetric interface elements of arbitrary order and is therefore presented in a general form. All of the axisymmetric computations described in this thesis were conducted using a ten-noded axisymmetric interface element, since this is kinematically compatible with both the fifteen-noded axisymmetric continuum element and the five-noded axisymmetric membrane element previously described. The specific equations for the case of the ten-noded element are presented in Appendix 5A.

5.4.1 Kinematic Equations

A general axisymmetric interface element with N nodes is shown in Figure 5.5. The interface element geometry consists of pairs of nodes sharing the same co-ordinates, however, within each pair the nodes have independent degrees of freedom. The global cylindrical polar co-ordinates of a point in the element are r, z and these are mapped onto a single reference co-ordinate α, as shown in Figure 5.5.

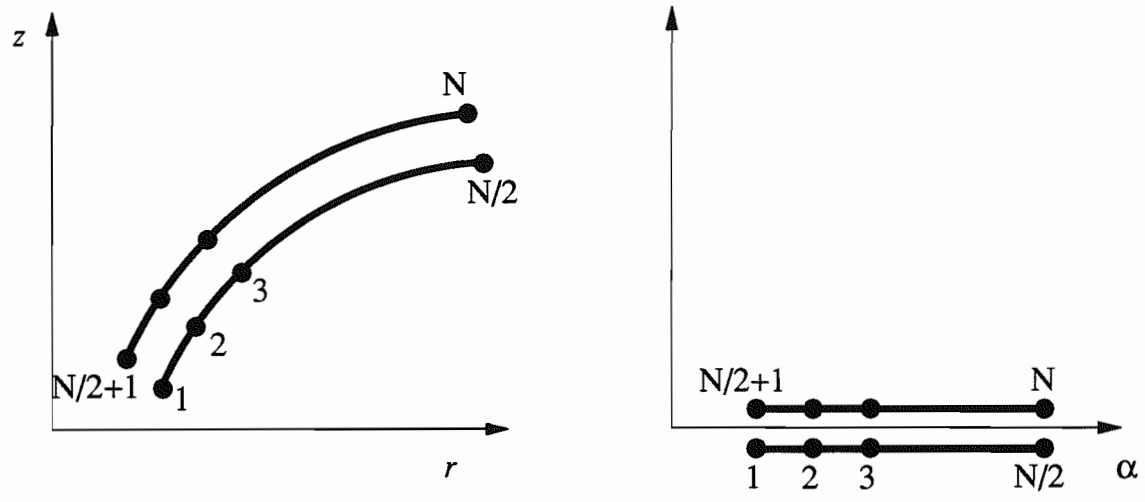

Parent Element **Mapped Element**

Figure 5.5: Isoparametric Mapping for an Axisymmetric Interface Element

Figure 5.6(a) shows an infinitesimal portion of the interface element where two coincident arbitrary points, a and b, lie on the element sides A and B. The vector of the global co-ordinates of the two points in the element is $\underset{\sim}{r}^T = [r_a \quad z_a \quad r_b \quad z_b]$ and is related to the vector of global nodal co-ordinates $\underset{\sim}{R}$ by:-

$$\underset{\sim}{r} = [N]\,\underset{\sim}{R} \tag{5.11}$$

where $[N]$, the shape function matrix, is a function of α. (Note that the co-ordinates (r_a, z_a) are identical to (r_b, z_b)).

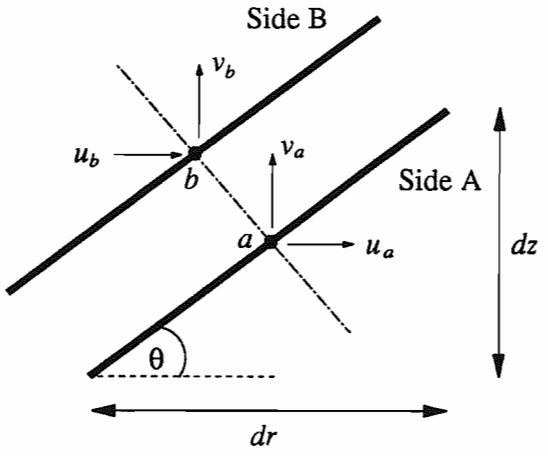

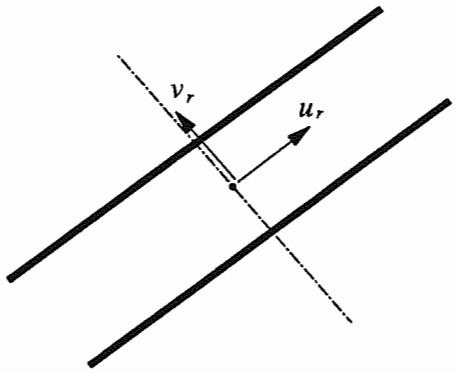

5.6(a) Global Velocities **5.6(b) Relative Velocities**

Figure 5.6: Interface Element Velocities

In a similar manner the velocity vector of the same two arbitrary points, $\underset{\sim}{u}^T = [u_a \quad v_a \quad u_b \quad v_b]$, is related to the nodal velocity vector $\underset{\sim}{U}$ by:-

$$\underset{\sim}{u} = [N]\,\underset{\sim}{U} \tag{5.12}$$

where $(u_a\ ,\ v_a)$ and $(u_b\ ,\ v_b)$ are the coincident velocities in the r and z directions at surfaces A and B respectively.

The velocities of the two congruent points on the interface may be resolved into directions parallel to, and perpendicular to, the local slope of the element, corresponding to the tangent and the normal of the element, Figure 5.6(b). The relative tangential (u_r) and normal (v_r) velocities within the interface are given by:-

$$u_r = (u_b - u_a)\cos\theta + (v_b - v_a)\sin\theta \tag{5.13}$$

$$v_r = (v_b - v_a)\cos\theta - (u_b - u_a)\sin\theta \tag{5.14}$$

where θ is the local angle of the interface relative to the r axis. The sign convention adopted here is that the relative tangential velocity is positive for the upper surface B moving to the right relative to the lower surface A and the normal velocity is positive when the interface surfaces move apart.

The vector of the relative velocities $\underset{\sim}{u_r}^T = [\, u_r \quad v_r \,]$ is given by the matrix equation:-

$$\underset{\sim}{u_r} = [S]\,[L]\,\underset{\sim}{u} \tag{5.15}$$

where:-

$$[L] = \begin{bmatrix} -1 & 0 & 1 & 0 \\ 0 & -1 & 0 & 1 \end{bmatrix} \tag{5.16}$$

and:-

$$[S] = \begin{bmatrix} \cos\theta & \sin\theta \\ -\sin\theta & \cos\theta \end{bmatrix} \tag{5.17}$$

The components of the matrix $[S]$ can be rewritten in terms of the infinitesimal lengths of the element and differentiated with respect to α, giving:-

$$\cos\theta = \frac{dr/d\alpha}{[\,(dr/d\alpha)^2 + (dz/d\alpha)^2\,]^{1/2}} \tag{5.18}$$

and:-

$$\sin\theta = \frac{dz/d\alpha}{[\,(dr/d\alpha)^2 + (dz/d\alpha)^2\,]^{1/2}} \tag{5.19}$$

The denominator of both these expressions can be interpreted as J, which represents the Jacobian of the transformation from parent co-ordinates (r, z) to the reference co-ordinates (α). In this case equations (5.18) and (5.19) may be rewritten:-

$$\cos\theta = \frac{1}{J}\frac{dr}{d\alpha} \tag{5.20}$$

and:-

$$\sin\theta = \frac{1}{J}\frac{dz}{d\alpha} \tag{5.21}$$

Substituting these equations into matrix $[S]$ given in equation (5.17) gives:-

$$[S] = \frac{1}{J}\begin{bmatrix} \frac{dr}{d\alpha} & \frac{dz}{d\alpha} \\ -\frac{dz}{d\alpha} & \frac{dr}{d\alpha} \end{bmatrix} = \frac{1}{J}\begin{bmatrix} r' & z' \\ -z' & r' \end{bmatrix} \tag{5.22}$$

where the prime denotes differentiation with respect to α.

Equation (5.15) can be rewritten in a more standard form by combining it with equation (5.12), giving:-

$$\underset{\sim}{u_r} = [B]\ \underset{\sim}{U} \tag{5.23}$$

where the matrix $[B]$ relates the vector of nodal velocities, $\underset{\sim}{U}$, to the vector of relative velocities at a point in the interface, $\underset{\sim}{u_r}$, and is given by:-

$$[B] = [S]\ [L]\ [N] \tag{5.24}$$

5.4.2 Constitutive Equations

The constitutive equations for this zero-thickness axisymmetric interface element are based on a Mohr-Coulomb elastic-perfectly frictional model of behaviour. Figure 5.7 schematically illustrates the Mohr-Coulomb yield function, $f(\sigma)$, defined by:-

$$f = |\tau| + \sigma \tan\phi_i = 0 \tag{5.25}$$

where ϕ_i is the angle of friction of the interface.

There are only two co-ordinate directions considered in axisymmetry (i.e. r and z) and only two component stresses are acting, the shear stress, τ, and normal stress, σ as shown in Figure 5.7. There is no circumferential shear stress, because there is no relative velocity in that direction. Tensile normal stress is considered as positive.

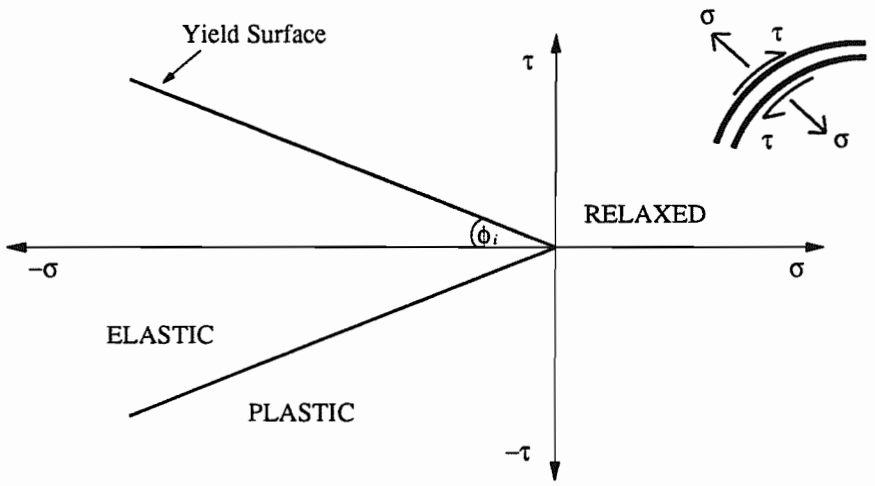

Figure 5.7: Mohr-Coulomb Yield Surface

The vector of stress, $\underset{\sim}{\sigma}$, of an arbitrary point in the interface can be differentiated with respect to time (denoted by a superior dot) to give the stress rate vector, $\dot{\underset{\sim}{\sigma}}^T = [\dot{\tau} \quad \dot{\sigma}]$, which is then related to the relative velocities, $\underset{\sim}{u_r}$, by the expression:-

$$\begin{aligned} \dot{\underset{\sim}{\sigma}} &= [D]^{EP} \underset{\sim}{u_r} \\ &= [D]^{EP} [B] \underset{\sim}{U} \end{aligned} \tag{5.26}$$

where $[D]^{EP}$ is the elasto-plastic material stiffness matrix and is expressed in terms of the elastic component of the material stiffness matrix $[D]^E$ and the plastic component $[D]^P$ thus:-

$$[D]^{EP} = [D]^E + [D]^P \tag{5.27}$$

Note that the interface element relative velocities are analogous to strain in continuum mechanics.

The elastic material stiffness matrix is essentially the same as that proposed in the

original work by Goodman *et al.* (1968), which is given by:-

$$[D]^E = \begin{bmatrix} k_s & 0 \\ 0 & k_n \end{bmatrix} \tag{5.28}$$

The parameters k_s and k_n represent the shear and normal stiffnesses of the interface, respectively.

The plastic material interface stiffness matrix is derived from the approach conventionally adopted for continuum elements (e.g. Burd (1986)) and is given by:-

$$[D]^P = \frac{-[D]^E \left[\frac{\delta g}{\delta \sigma}\right] \left[\frac{\delta f}{\delta \sigma}\right]^T [D]^E}{\left[\frac{\delta f}{\delta \sigma}\right]^T [D]^E \left[\frac{\delta g}{\delta \sigma}\right]} \tag{5.29}$$

This equation (5.29) involves the assumptions that the relative velocities can be decomposed into elastic and plastic parts and that the stress rate is related to the elastic relative velocities. The Mohr-Coulomb yield function, $f(\sigma)$, is given in equation (5.25) and $g(\sigma)$ is the plastic potential which is used to define the plastic relative velocities using equations of the form:-

$$u_r^P = \lambda \frac{\delta g}{\delta \tau} \tag{5.30}$$

$$v_r^P = \lambda \frac{\delta g}{\delta \sigma} \tag{5.31}$$

where λ is an undetermined multiplier. The plastic potential developed in this analysis is assumed to be non-associated, where:-

$$g = |\tau| + \sigma \tan \psi_i \tag{5.32}$$

and ψ_i is the angle of dilation of the interface. A non-associated flow rule allows the dilation characteristics of the material to be specified independently from the friction angle.

If the Gauss point stress lies inside the yield surface, then the plastic stiffness matrix is set to zero, but if the stress point lies on the yield surface then $[D]^{EP}$ is:-

$$[D]^{EP} = \frac{k_n \, k_s}{k_s + k_n \tan \phi_i \tan \psi_i} \begin{bmatrix} \tan \phi_i \tan \psi_i & -sgn(\tau) \tan \phi_i \\ -sgn(\tau) \tan \psi_i & 1 \end{bmatrix} \tag{5.33}$$

where $sgn(\tau) = 1$ for $\tau > 0$ and $sgn(\tau) = -1$ for $\tau < 0$.

5.4.3 Stress Update Calculations

The finite element calculations are typically conducted as a series of steps for a particular prescribed displacement, or prescribed force, or indeed a mixture of both. At the end of each load step, corresponding to a finite time increment Δt, the updated normal and shear stresses associated with the calculated relative velocities are determined by a 'stress update procedure'. This provides for a check on the general equilibrium of the system and also gives the out-of-balance nodal forces that are needed for the incremental solution procedure. The computed final stresses are characterised into different states according to their position in stress space relative to the Mohr-Coulomb failure envelope shown in Figure 5.8. The three possible states are denoted as Elastic, Plastic and Relaxed as indicated in Figure 5.8.

At the start of a load step $\Delta t = 0$ and at the end $\Delta t = 1$. In order to calculate the Gauss point stresses at the end of a load step the response of each Gauss point is assumed, initially, to be elastic, regardless of initial state. The relevant final stresses, τ and σ, are calculated using the elastic material stiffness matrix $[D]^E$ in equation (5.26), giving:-

$$\tau = \tau_0 + k_s u_r \Delta t \tag{5.34}$$

$$\sigma = \sigma_0 + k_n v_r \Delta t \tag{5.35}$$

where τ_0 and σ_0 are the initial Gauss point stresses and $\Delta t = 1$ at the end of the load step.

This assumption of a purely elastic stress update is then checked to ensure that the final stresses, τ and σ, have not violated the failure conditions:-

1) If $|\tau / \sigma| \geq \tan\phi_i$ then the updated stress point has yielded and must be re-analysed plastically beyond the point that the stress path intersects the Mohr-Coulomb yield surface.

2) If $\sigma \geq 0$ then separation of the interface has occurred during the load step and the stress point must be relaxed by setting the stresses to zero, i.e. $\sigma = \tau = 0$.

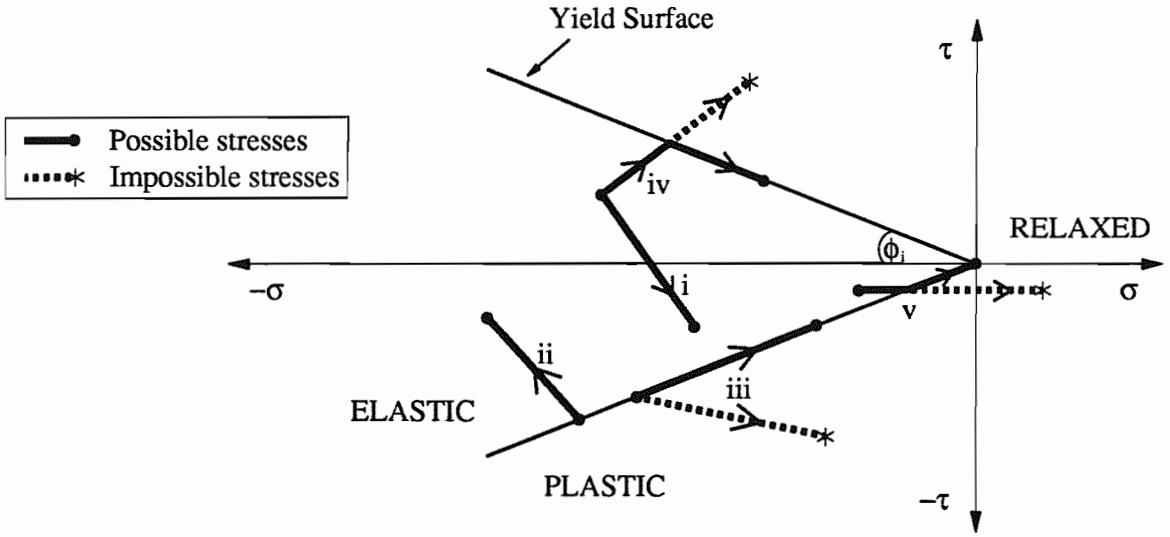

Figure 5.8: Mohr-Coulomb Yield Surface and Possible cases of Constitutive Behaviour

There are five possible cases of constitutive behaviour, realising that the initial stress state is either elastic and lies inside the failure envelope, or plastic and lies on the failure envelope, as illustrated in Figure 5.8.

Case (i)

The calculated stresses at the end of the assumed elastic step are correct.

Case (ii)

The Gauss point stress is initially on the failure envelope, but the final stresses are correct since the behaviour involves a purely elastic increment away from the yield surface.

Case (iii)

As in case (ii) the initial Gauss point stress lies on the failure envelope, but for this case the assumed elastic increment produces stresses outside of the yield surface. The entire step, therefore, has to be re-analysed plastically using the elasto-plastic material stiffness matrix $[D]^{EP}$ in equation (5.26), so that the final stresses are:-

$$\tau = \tau_0 + C\,(u_r \tan\phi_i \tan\psi_i - v_r\, sgn(\tau_0) \tan\phi_i)\,\Delta t \tag{5.36}$$

$$\sigma = \sigma_0 + C\,(-u_r\, sgn(\tau_0) \tan\psi_i + v_r)\,\Delta t \tag{5.37}$$

where the constant, C, is:-

$$C = \frac{k_n\, k_s}{k_s + k_n \tan\phi_i \tan\psi_i} \tag{5.38}$$

Case (iv)

The initial stress point is elastic, but the elastic updated stresses lie outside of the yield surface. The proportion of the time increment, β, at which the stresses crossed the yield surface must be determined from the equation given by combining equations (5.34), (5.35) and the yield function equation (5.25):-

$$\frac{(\tau_0 + k_s\, u_r\, \beta\Delta t)^2}{(\sigma_0 + k_n\, v_r\, \beta\Delta t)^2} = \tan^2\phi_i \tag{5.39}$$

for which there will be only one positive real root and $0 < \beta < 1$.

The elastic and plastic parts of the stress increment can then be calculated separately for the time increments $\beta\Delta t$ and $(1-\beta)\Delta t$, respectively. The yield point stresses, τ_y and σ_y, are calculated from the elastic equations (5.40) and (5.41):-

$$\tau_y = \tau_0 + k_s\, u_r\, \beta\Delta t \tag{5.40}$$

$$\sigma_y = \sigma_0 + k_n\, v_r\, \beta\Delta t \tag{5.41}$$

and the final plastic stresses, using $[D]^{EP}$, are:-

$$\tau = \tau_y + C\,(u_r \tan\phi_i \tan\psi_i - v_r\, sgn(\tau_y) \tan\phi_i)\,(1-\beta)\,\Delta t \tag{5.42}$$

$$\sigma = \sigma_y + C\,(-u_r\, sgn(\tau_y) \tan\psi_i + v_r)\,(1-\beta)\,\Delta t \tag{5.43}$$

where the constant, C, is given in equation (5.38).

Case (v)

An additional consideration when correcting a yielded, or relaxed stress point back onto the yield surface is whether the plastic stresses have passed through the origin, i.e. the plastic normal stress becomes positive. In this situation the final plastic stresses must remain at zero, since the shear stress cannot change sign. This particular case of constitutive behaviour is depicted in Figure 5.8.

The elastic and plastic stress updating is initially done by the method described for case (iv), but if $\sigma \geq 0$ by equation (5.43) then both final stresses are set to zero, i.e. $\sigma = \tau = 0$.

If γ is the proportion of the time increment between the point of yield surface intersection and the origin, then the precise time at which the shear stress passes through the origin is given by:-

$$(\beta + \gamma)\,\Delta t \;=\; \frac{\tau_y - \tau_0}{k_s\, u_r} - \frac{\tau_y}{C\,(\,u_r \tan\phi_i \tan\psi_i \;-\; v_r\, sgn(\tau_y) \tan\phi_i\,)} \tag{5.44}$$

where $0 < \gamma < 1$, equation (5.40) gives τ_y and C is given in equation (5.38).

These updated final stresses are used for the equilibrium check to find the new nodal forces in the interface element.

5.4.4 Finite Element Equations

If a set of virtual velocities $\underset{\sim}{U}^*$ are applied to the nodes of the element, then by the principle of virtual work:-

$$\underset{\sim}{U}^{*T}\,\underset{\sim}{P} \;=\; \int_E \underset{\sim}{u_r}^{*T}\,\underset{\sim}{\sigma}\; dA \tag{5.45}$$

where $\underset{\sim}{u_r}^*$ are the relative velocities compatible with the virtual nodal velocities, $\underset{\sim}{U}^*$, and $\underset{\sim}{P}$ is the vector of nodal forces which are in equilibrium with the stresses $\underset{\sim}{\sigma}^T = [\,\tau \quad \sigma\,]$. The integration is performed over the surface area of the element.

The elemental surface area, dA , is given by:-

$$dA = 2\pi r J \quad d\alpha \tag{5.46}$$

It follows, therefore, that the virtual work equation (5.45) can be rewritten, substituting for the relative velocities vector as given in equation (5.23), as:-

$$\underset{\sim}{U}^{*T} \underset{\sim}{P} = 2\pi \int_E \underset{\sim}{U}^{*T} [B]^T \underset{\sim}{\sigma} r J \quad d\alpha \tag{5.47}$$

Since this expression must hold for arbitrary nodal velocities $\underset{\sim}{U}^*$, it follows that:-

$$\underset{\sim}{P} = 2\pi \int_E [B]^T \underset{\sim}{\sigma} r J \quad d\alpha \tag{5.48}$$

where the scalar variable r , the radius, is conveniently expressed by the matrix equation:-

$$r = \underset{\sim}{k} [N] \underset{\sim}{R} \tag{5.49}$$

where $\underset{\sim}{k}$ is the constant vector $[1 \quad 0 \quad 1 \quad 0]$.

Equation (5.48) is differentiated with respect to time to give the nodal force rate vector:-

$$\dot{\underset{\sim}{P}} = 2\pi \int_E \left\{ [B]^T \dot{\underset{\sim}{\sigma}} r J + (\dot{[B]^T} J) \underset{\sim}{\sigma} r + [B]^T \underset{\sim}{\sigma} \dot{r} J \right\} \quad d\alpha \tag{5.50}$$

Note that in the second term of the integrand the superior dot relates to the product $([B]^T J)$. In order to use this expression to derive an element stiffness matrix it is necessary to express each component of the integrand in terms of the vector of nodal velocities, $\underset{\sim}{U}$, so that:-

$$\dot{\underset{\sim}{P}} = [K] \underset{\sim}{U} \tag{5.51}$$

where $[K]$ is the incremental stiffness matrix given by:-

$$[K] = 2\pi \int_E \{ [B]^T [D]^{EP} [B] r J + [C] \} \, d\alpha \tag{5.52}$$

The first term in the integrand of the incremental stiffness matrix is the conventional infinitesimal displacement stiffness matrix obtained by substituting equation (5.26) into equation (5.50), i.e. :-

$$[B]^T \dot{\underset{\sim}{\sigma}} r J = [B]^T [D]^{EP} [B] \underset{\sim}{U} r J \tag{5.53}$$

The second component in equation (5.52) is the distortion rate matrix, $[C]$, which contains additional terms to account for the rate of change of element geometry, as proposed by Burd (1986). These need to be included in the stiffness matrix to model the large strain and large displacement effects. Equation (5.52) compares to the form of the axisymmetric incremental stiffness matrix for the continuum elements, equation (3.8), and the axisymmetric membrane elements, equation (4.22). The distortion rate matrix is obtained by the combination of two terms (c.f. equation (3.10)):-

$$[C] U = (\dot{[B]}^T J) \underset{\sim}{\sigma} r + [B]^T \dot{\underset{\sim}{\sigma}} \dot{r} J \tag{5.54}$$

where the first term in the distortion rate matrix gives the rate of change of element geometry and is evaluated by algebraic manipulation, rather than by the term-by-term expansion procedure that was necessary for the axisymmetric membrane element distortion rate matrix (see Section 4.2.2). The second term of the $[C]$ matrix accounts for the rate of change of the nodal co-ordinates with time.

The first part of the distortion rate matrix may be rewritten by substituting for $[B]$ using equation (5.24), giving:-

$$(\dot{[B]}^T J) \underset{\sim}{\sigma} r = [N]^T [L]^T (\dot{[S]}^T J) \underset{\sim}{\sigma} r \tag{5.55}$$

From equation (5.22):-

$$[S]^T J = \begin{bmatrix} r' & -z' \\ z' & r' \end{bmatrix} \tag{5.56}$$

This equation may be differentiated with respect to time and multiplied by the stress vector $\underset{\sim}{\sigma}$ to give:-

$$(\,[S]^{\dot{T}}\,J\,)\,\underset{\sim}{\sigma} \;=\; \begin{bmatrix} \dot{r}' & -\dot{z}' \\ \dot{z}' & \dot{r}' \end{bmatrix} \begin{bmatrix} \tau \\ \sigma \end{bmatrix} \tag{5.57}$$

which is re-arranged to give:-

$$(\,[S]^{\dot{T}}\,J\,)\,\underset{\sim}{\sigma} \;=\; \begin{bmatrix} \tau & -\sigma \\ \sigma & \tau \end{bmatrix} \begin{bmatrix} \dot{r}' \\ \dot{z}' \end{bmatrix} \tag{5.58}$$

The two variables, r and z, are the co-ordinates of the stress point and may be conveniently written in the form:-

$$\begin{bmatrix} r \\ z \end{bmatrix} \;=\; [A]\,\underset{\sim}{r} \tag{5.59}$$

where $\underset{\sim}{r}$ is the global co-ordinates vector as given in equation (5.11) and the matrix constant, $[A]$, is:-

$$[A] \;=\; \begin{bmatrix} \frac{1}{2} & 0 & \frac{1}{2} & 0 \\ 0 & \frac{1}{2} & 0 & \frac{1}{2} \end{bmatrix} \tag{5.60}$$

Differentiating equation (5.59) with respect to both α and time, and then substituting $\underset{\sim}{u'}$ using equation (5.12) gives:-

$$\begin{aligned} \begin{bmatrix} \dot{r}' \\ \dot{z}' \end{bmatrix} \;&=\; [A]\,\underset{\sim}{u'} \\ &=\; [A]\,[N']\,\underset{\sim}{U} \end{aligned} \tag{5.61}$$

Combining this expression with equation (5.58) gives:-

$$(\,[S]^{\dot{T}}\,J\,)\,\underset{\sim}{\sigma} \;=\; [Q]\,[A]\,[N']\,\underset{\sim}{U} \tag{5.62}$$

where:-

$$[Q] = \begin{bmatrix} \tau & -\sigma \\ \sigma & \tau \end{bmatrix} \tag{5.63}$$

If equation (5.62) is combined with equation (5.55), then the first term in the distortion rate equation (5.54) may be shown to be:-

$$\begin{aligned} ([B]^T J)\,\underset{\sim}{\sigma}\, r &= [N]^T [L]^T [Q] [A] [N'] \underset{\sim}{U}\, r \\ &= [C_1] \underset{\sim}{U}\, r \end{aligned} \tag{5.64}$$

The second term of the $[C]$ matrix may be rewritten by substituting equation (5.49) and noting that $\underset{\sim}{\dot{R}} = \underset{\sim}{U}$. The distortion rate matrix can therefore be written fully as:-

$$[C]\,U = [C_1]\,\underset{\sim}{U}\, r + [B]^T \underset{\sim}{\sigma}\, \underset{\sim}{k}\, [N]\, \underset{\sim}{U}\, J \tag{5.65}$$

A seven-point Gaussian quadrature scheme is used to evaluate the incremental element stiffness matrix of equation (5.52). As previously discussed in Section 4.2.2, exact integration can only be achieved for an element that has the nodes equally spaced, is initially straight and does not experience any severe distortion. If the finite element analysis was carried out as a small displacement problem, then the exact integration pre-requisites would be satisfied and it can be shown from Appendix 5A that a seven-point Gauss quadrature would be sufficient. However, within a large displacement analysis the interface element will be subjected to finite distortion and exact integration in this case is not possible. Therefore, it is reasonable to choose an order of quadrature based on the ideal configuration, although the limitations of this chosen integration scheme must be realised.

At the end of each step of the finite element analysis it is necessary to update each of the nodal co-ordinates of the deformed mesh by the calculated incremental displacements. For the interface elements this is done by determining the individual updated nodal co-ordinates and then calculating the arithmetic mean for the corresponding pairs and updating the co-ordinates to this mean position, so that they continue to share a common position.

Note that all of the plane strain large displacement computations described in this thesis were carried out using the six-noded plane strain interface element (Burd and Brocklehurst (1991)), with a three-point Gaussian integration rule.

5.4.5 Limitations of the Interface Element

The formulations of the axisymmetric and plane strain interface elements are based on an elastic perfectly-frictional model of behaviour. In modelling a two-layer soil system this interface element is appropriate for the boundary between the frictional fill layer and the reinforcement, but it is somewhat limited when modelling the clay-reinforcement boundary because of the cohesive nature of the clay.

The potential problem in modelling a cohesive interface with frictional interface elements is that the predicted shear stresses may exceed the shear strength of the clay (as seen in Figures 7.5, 8.2, 9.4, 10.2 and 10.3). This is because the discretization in the clay may allow nodal forces to exceed the clay strength. Although the interface element formulations could be broadened to include a cohesive strength term as well as friction, which would ensure that the shear stresses did not exceed the clay shear strength, this would make only a difference to the absolute peak shear stress values and no difference to the overall trend of the stress distributions.

The further limitation of the axisymmetric and plane strain interface element formulations is that they do not allow correctly for the re-joining of the mating surfaces after they have been relaxed. For instance, if the normal stress across the element was to become tensile (i.e. positive), thus tending to separate the interface surfaces, the formulation immediately sets the stresses to zero, but does not calculate the would-be separating distance. When the normal stress becomes compressive again, the formulation assumes the surfaces are at once in contact, rather than allowing for the potentially large separating distance to be recovered. Despite this shortcoming the interface element formulation is applicable to the modelling of the boundaries in the two-layer soil systems considered herein, because separation of the mating surfaces does not occur (see the contours of vertical stress, plates 6.3 and 6.4 Appendix 6B).

5.5 Verification of the Axisymmetric Interface Formulation

The new large strain axisymmetric interface formulation is validated by a series of test analyses. A lack of appropriate benchmarks has meant that a less than comprehensive validation for this element has been undertaken, i.e. all the tests are for horizontal and vertical configurations only. Some of these analyses were found initially to be rather unstable, so in order to improve the computation the incremental stiffness matrix ($[K]$, equation (5.52)) is made purely elastic by negating the plasticity part of the elasto-plastic material stiffness matrix ($[D]^{EP}$). Although the element stiffness is then based upon the elastic stiffnesses only, the stress updating still considers plasticity and therefore the overall solution for stresses is correct. This approach has been used for all the interface element analyses discussed throughout this dissertation. A similar procedure was adopted also by Bell (1991).

5.5.1 Single Interface Element under Constant Normal Stress

A small strain analysis is conducted using a single axisymmetric interface element as shown in Figure 5.9, where the length of the element, l, and the inner radius from the centre-line to the element are both taken as unity. The lower nodes of the interface are fixed horizontally and vertically, while the upper nodes are each displaced horizontally by the same amount, u_r. A constant normal stress of $\sigma = 100\ kPa$ is applied throughout the analysis.

The shear and normal stiffnesses of the interface, k_s and k_n, are equal to $10^4\ kN/m$ and $10^8\ kN/m$ respectively, and the angles of friction and dilation of the interface are $\phi_i = 30°$ and $\psi_i = 0°$, respectively. The resulting shear stresses, τ, and shear displacements, u_r, are depicted in Figure 5.9 for the case of initial loading, partial unloading and then re-loading. The stresses and displacements of the seven Gauss points are identical to each other and the correct behaviour is obtained.

5.5.2 Single Interface Element Subjected to Yield

A single horizontal axisymmetric interface element, similar to that shown in Figure 5.9, is fixed horizontally and vertically along the lower surface and subjected to a variable compressive normal stress, σ, along the upper surface. By applying increments of horizontal

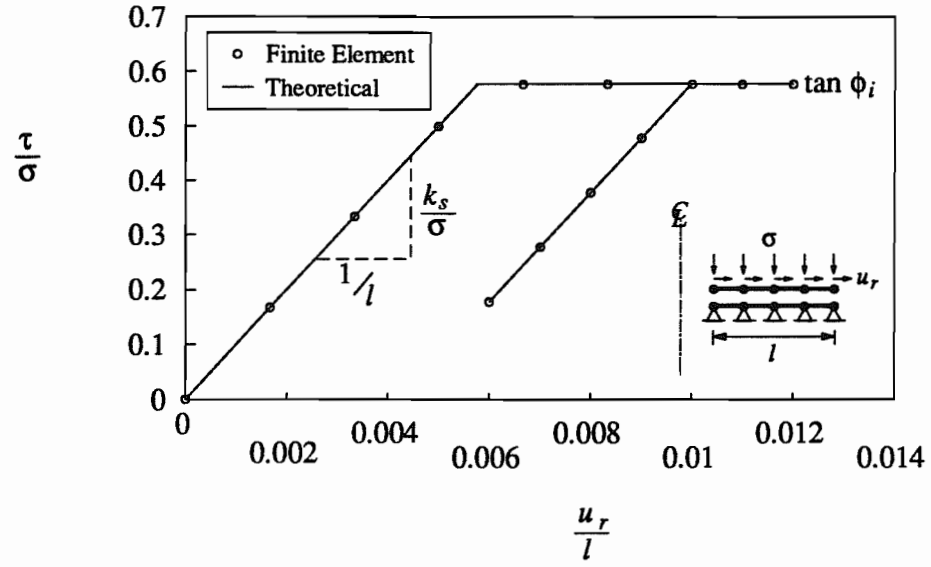

Figure 5.9: Shear Stress against Shear Displacement for a Single Interface Element

displacement to each of the upper nodes, the normal and shear stress paths of a single Gauss point can be traced, as shown in Figure 5.10 for different initial σ. The stresses and displacements of all of the integration points are identical. Once the displacements in each case become large enough to cause yield of the interface, further displacements generate both increasing σ, due to the assumed dilation of the interface, and τ as the stress paths correctly follow the yield surface. The interface properties are given in Figure 5.10.

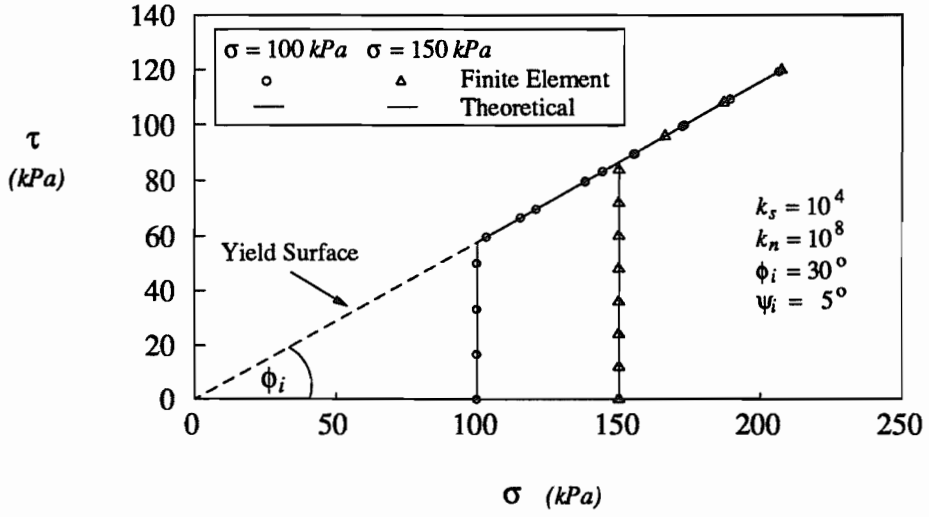

Figure 5.10: Shear Stress against Normal Stress for a Single Interface Element

5.5.3 Adjacent Concentric Thick Cylinders

Two concentric adjacent cylinders of wall thickness and inner radius $a = 1\ m$, separated vertically by interface elements, are subjected initially to a uniform internal outward acting pressure, $q = 100\ kN/m$, so that the interface is under compression. The outer cylinder is then vertically displaced relative to the inner cylinder by an amount δ, while holding q constant. The mesh of sixteen 15-noded axisymmetric continuum elements and two interface elements is shown schematically in Figure 5.11.

The cylinders are assigned a Young's modulus of $E = 5\text{x}10^4\ kPa$, a shear strength of $1.2\text{x}10^9\ kPa$ and a Poisson's ratio of zero. This small displacement analysis is conducted for two different interface friction angles, $\phi_1 = 20°$ and $\phi_2 = 30°$, while the other interface properties of dilation angle, $\psi_i = 0$, and the shear and normal stiffnesses, $k_s = 10^5\ kN/m$ and $k_n = 10^{10}\ kN/m$, are kept constant.

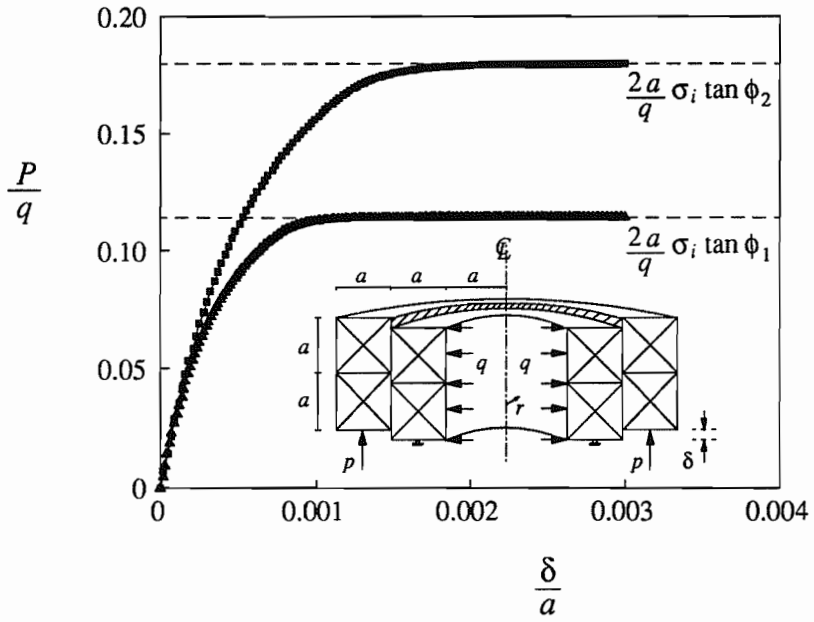

Figure 5.11: Pressure against Displacement for Outer Thick Cylinder

The pressure, P, at the base of the outer cylinder is plotted in Figure 5.11 against the small relative displacement, δ. The limit pressure, P_u, for each analysis is dependent upon the value of the friction angle and can be analytically determined by the equation:-

$$P_u = 2\,a\,\sigma_i \tan\phi_i \tag{5.66}$$

where σ_i is the radial stress across the interface (of length $2a$). Since the interface is of infinitesimal thickness and its stiffness does not significantly effect the radial stress distribution through the cylinders (as shown in Figure 5.13), σ_i can be calculated by using the equations (4.53), which are derived by equilibrium, compatibility of strain and the stress-strain relationships of elasticity. By applying the boundary conditions (at $r = a$, $\sigma_r = -q$ and at $r = 3a$, $\sigma_r = 0$), it may be shown that at $r = 2a$:-

$$\sigma_i = \frac{q}{8}\left(1 - 9\left(\frac{a}{r}\right)^2\right) = -15.625 \tag{5.67}$$

There is a good agreement between the finite element solutions and the simplified analytical calculations for P_u, Figure 5.11. Although the average shear stress, τ, along the interface gives the correct yield response for increasing δ, Figure 5.12, there is a slight variation between the distributions of τ along the lengths of the higher and lower interface elements ($\pm 5\%$), due to the bending moment created by the displaced outer cylinder.

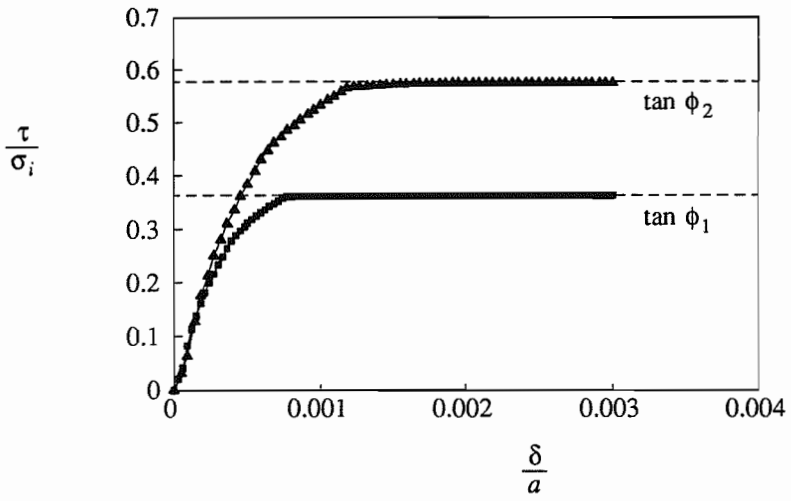

Figure 5.12: Shear Stress at Interface against Displacement

For the initial loading condition, where only a uniform internal pressure q is applied, the radial and circumferential stresses are continuous through the two cylinders, Figure 5.13, with the meridional stresses at zero. The finite element results are for each Gauss point throughout the continuum elements, with the analytical elasticity solutions shown for comparison. The results display an exact match for this small displacement elastic analysis.

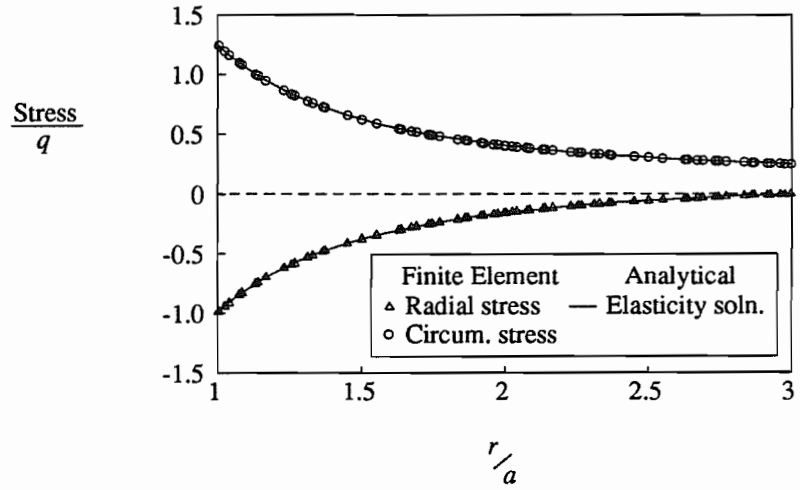

Figure 5.13: Stresses through the Thick Cylinders

5.5.4 Elastic Annular Plate under Inward Internal Pressure

An elastic annular plate of thickness and inner radius a = 1 m and outer radius b = 10a, modelled by fourteen axisymmetric continuum elements, is sandwiched between two layers of interface elements as shown in Figure 5.14. A uniform vertical stress of q = 10 kN/m is applied continuously across the system, while the inner cavity is progressively displaced inwards by an amount δ, generating an inward internal pressure P.

The properties assigned to the plate are a Young's modulus $E = 10^5\ kPa$, a shear strength of $1.2 \times 10^9\ kPa$ and a Poisson's ratio of zero. The two identical interfaces have the properties of a friction angle $\phi_i = 30°$, a dilation angle $\psi_i = 0$ and the shear and normal stiffnesses $k_s = k_n = 10^5\ kN/m$.

The value of P is dependent upon the magnitudes of both the inner displacement, δ, and the outward acting body forces imposed by the frictional interface elements on the top and bottom of the plate, F (per unit area). However, the magnitude of F ($= \tau$) is dependent upon δ also, as shown in Figure 5.15. As the displacements increase at the inner radius ($r = a$) the shear stresses along the interfaces vary from the initial fully elastic case ($\tau^e = k_s\ u_r$), to the partially plastic-elastic case (illustrated in Figure 5.15) and ultimately to the fully plastic case ($\tau^p = q\ \tan\phi_i$). The complete analytical solution relating P and δ for

the elastic-plastic interfaces proved unobtainable, but by assuming that only the fully plastic case prevails (i.e. $F = q \tan\phi_i$) and that the plate remains elastic, the following solution is derived.

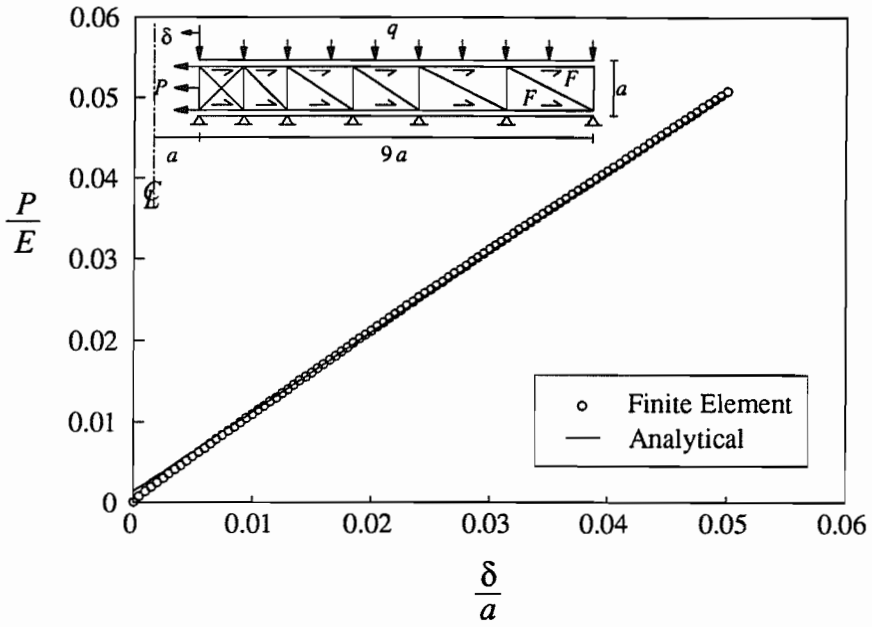

Figure 5.14: Pressure against Displacement

By using the equations of equilibrium, compatibility of strain and the stress-strain relationships of elasticity it may be shown that:-

$$\frac{d^2\delta}{dr^2} + \frac{1}{r}\frac{d\delta}{dr} - \frac{\delta}{r^2} = -\frac{2F}{E}(1-\nu^2) \tag{5.68}$$

The sum of the complementary function and the particular integral of this second order linear differential equation gives:-

$$\delta = Ar + \frac{B}{r} - \frac{2Fr^2}{3E}(1-\nu^2) \tag{5.69}$$

where A and B are constants determined from the boundary conditions, i.e. at $r = a$, $\sigma_r = P$ and at $r = b$, $\sigma_r = 0$.

Solving for A and B gives:-

$$P = C\left\{\delta+\frac{2F}{3E}\left[(1-\nu^2)r^2-\frac{(2+\nu)}{(a+b)r}[(b^2+ab+a^2)(1-\nu)r^2+a^2b^2(1+\nu)]\right]\right\} \tag{5.70}$$

where the constant C is:-

$$C = \frac{E\,(a^2-b^2)\,r}{a^2\,[r^2\,(1-\nu)+b^2\,(1+\nu)]} \tag{5.71}$$

The correlation between the finite element solution and the simplified analytical calculation for P, presented in Figure 5.14, is very close. There is however an observable discrepancy between the results at small values of δ, because, contrary to the analytical assumption, full plasticity has not developed across the entire interface lengths, Figure 5.15.

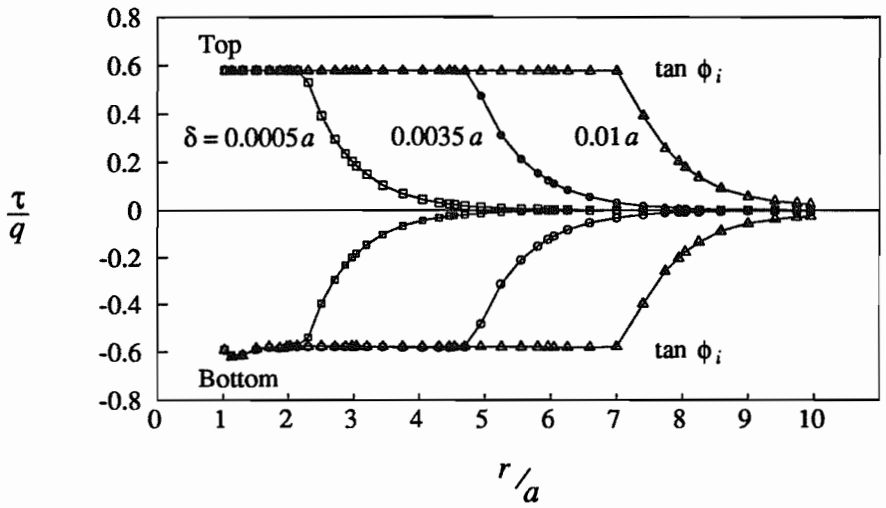

Figure 5.15: Shear Stress Distribution along Interfaces

APPENDIX 5A

Finite Element Equations for the Ten-Noded Interface Element

Figure 5.16 shows the isoparametric mapping between the parent and reference elements for the ten-noded interface element.

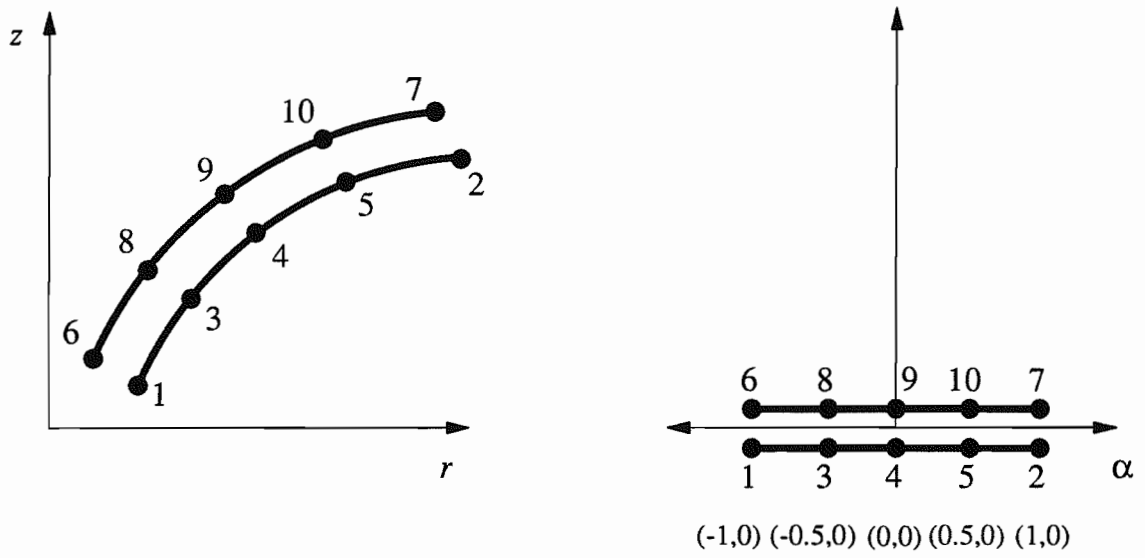

Parent Element **Mapped Element**

Figure 5.16: Mapping for the Ten-Noded Axisymmetric Interface Element

The vectors $\underset{\sim}{r}$ and $\underset{\sim}{R}$, that are related by equation (5.11), are defined as:-

$$\underset{\sim}{r}^T = [\, r_a \quad z_a \quad r_b \quad z_b \,] \tag{5.72}$$

$$\underset{\sim}{R}^T = [\, R_1 \quad Z_1 \quad R_2 \quad Z_2 \quad \ldots \quad R_{10} \quad Z_{10} \,] \tag{5.73}$$

Where R_i, Z_i are the global co-ordinates of the i^{th} node. The shape function matrix, which is required to keep the co-ordinates (r_a, z_a) and (r_b, z_b) congruent, is of the form:-

$$[N] = \begin{bmatrix} f_1 & 0 & f_2 & 0 & \cdots & f_5 & 0 & 0 & 0 & 0 & 0 & \cdots & 0 & 0 \\ 0 & f_1 & 0 & f_2 & \cdots & 0 & f_5 & 0 & 0 & 0 & 0 & \cdots & 0 & 0 \\ 0 & 0 & 0 & 0 & \cdots & 0 & 0 & f_1 & 0 & f_2 & 0 & \cdots & f_5 & 0 \\ 0 & 0 & 0 & 0 & \cdots & 0 & 0 & 0 & f_1 & 0 & f_2 & \cdots & 0 & f_5 \end{bmatrix} \tag{5.74}$$

in which:-

$$f_1 = \frac{2}{3}(\alpha+1/2)(\alpha)(\alpha-1/2)(\alpha-1) \tag{5.75}$$

$$f_2 = \frac{2}{3}(\alpha+1/2)(\alpha)(\alpha-1/2)(\alpha+1) \tag{5.76}$$

$$f_3 = -\frac{8}{3}(\alpha+1)(\alpha)(\alpha-1/2)(\alpha-1) \tag{5.77}$$

$$f_4 = 4(\alpha+1)(\alpha-1)(\alpha+1/2)(\alpha-1/2) \tag{5.78}$$

$$f_5 = -\frac{8}{3}(\alpha+1)(\alpha)(\alpha+1/2)(\alpha-1) \tag{5.79}$$

Note, these shape functions are the same as those used for the five-noded axisymmetric membrane element.

The matrix $[B]$ of equation (5.24) is given by:-

$$[B] = \frac{1}{J}\begin{bmatrix} -f_1 r' & -f_1 z' & \cdots & -f_5 r' & -f_5 z' & f_1 r' & f_1 z' & \cdots & f_5 r' & f_5 z' \\ f_1 z' & -f_1 r' & \cdots & f_5 z' & -f_5 r' & -f_1 z' & f_1 r' & \cdots & -f_5 z' & f_5 r' \end{bmatrix} \tag{5.80}$$